University of Bath

PHD

Linear and Nonlinear Optics in Coupled Waveguide Arrays

De Nobriga, Charles

Award date:
2013

Awarding institution:
University of Bath

Link to publication

Alternative formats
If you require this document in an alternative format, please contact:
openaccess@bath.ac.uk

Copyright of this thesis rests with the author. Access is subject to the above licence, if given. If no licence is specified above, original content in this thesis is licensed under the terms of the Creative Commons Attribution-NonCommercial 4.0 International (CC BY-NC-ND 4.0) Licence (https://creativecommons.org/licenses/by-nc-nd/4.0/). Any third-party copyright material present remains the property of its respective owner(s) and is licensed under its existing terms.

Take down policy
If you consider content within Bath's Research Portal to be in breach of UK law, please contact: openaccess@bath.ac.uk with the details. Your claim will be investigated and, where appropriate, the item will be removed from public view as soon as possible.

Download date: 05. May. 2023

Linear and Nonlinear Optics in Coupled Waveguide Arrays

Charles de Nobriga

A thesis submitted for the degree of Doctor of Philosophy

University of Bath

Department of Physics

September 2012

COPYRIGHT

Attention is drawn to the fact that copyright of this thesis rests with the author. A copy of this thesis has been supplied on condition that anyone who consults it is understood to recognise that its copyright rests with the author and that they must not copy it or use material from it except as permitted by law or with the consent of the author.

This thesis may be made available for consultation within the University Library and may be photocopied or lent to other libraries for the purposes of consultation.

. . . . . .

for Nette and Tilly

Acknowledgements

I would like to thank everybody who has made my journey possible and encouraged all my endeavours towards the completion of this thesis. There are some special people in my life that deserve a special mention.

Firstly, and most importantly, I want to thank my family. Nette and Tilly have given my fantastic support. Every day has been made enjoyable throughout my journey.

All the people that have worked closely with me throughout my time at the Univeristy of Bath: Gareth, Wei, Chris, Andrey, Dmitry, William, Brian, Antonio, Michael, Marc and Richard. All of your advice and insight has been immeasurably important to me.

Finally I would like to thank Jonathan. From the moment I walked into his office as an undergraduate in 2003 he has been with me every step of the way.

Without your help, this would not have been possible. Thank you all.

Overview

The following thesis is comprised of four main areas of work. These are centred around the experimental observation of phenomena associated with both linear and non-linear optics in silicon photonic-wires. As a comparison, I also discuss a similar coupled-waveguide system; dual-core hollow-core photonic crystal fibre.

To introduce the reader to this work, the first chapter will recap some undergraduate level theory; a general introduction to optical waveguides. It is not intended to be a complete theoretical picture, as many beautiful texts on optics already exist [1–3]. This chapter concerns itself only with the aspects of optics with which the author was intimately aware of throughout the completion of this thesis.

Thereafter, the chapters become specific to the particular experiments undertaken. Each one follows a simple framework: examination of the relevant theory, extending upon that already discussed in the first chapter, a literature review and finally a discussion of the work I completed within this thesis.

Chapter 2 is the only chapter not related to silicon based photonics. Here I discuss dual-core hollow-core photonic crystal fibres; including guidance mechanisms, fabrication methods and the numerical modelling techniques employed in my work. I will compare these numerical results to experimental results taken by colleagues at the university of Bath.

Chapter 3 analyses linear propagation in arrays of silicon photonic wires. I extend the simple picture of light propagating in waveguides to discuss the different types of dispersion inherent in this system and how dispersion tailoring can be achieved; with reference to the other literature on this topic. Experimental results are examined and discussed.

Chapters 4 and 5 discuss non-linear propagation in silicon photonic wire arrays; modulation instability and spatio-temporal solitons respectively. In each

case I extend the ideas on non-linearity presented in Chapter 1 to explain both modulation instability and optical solitons. Detailed descriptions of the experiments undertaken, and associated numerical modelling completed are then discussed. Whilst the work I present is incomplete, I will discuss subsequent work performed by my colleagues at the University of Bath based on my initial work.

Finally, Chapter 6 draws together my conclusions.

Contents

1 Optical Waveguides **10**

1.1 Introduction 10

1.2 Waveguides and Waveguide modes 10

1.3 Maxwell's Equations, the Wave Equation and the Propagation Constant 11

1.4 Chromatic Dispersion 13

1.5 Attenuation 15

1.5.1 Photonic Wires 16

1.5.2 Hollow-Core Photonic Bandgap Fibres 17

1.6 Nonlinearity 19

1.6.1 Kerr Nonlinearity 20

1.6.2 Self-Phase Modulation 21

1.6.3 Dispersion and SPM 23

1.6.4 Solitons 24

1.7 Waveguide Arrays and Coupled Mode Theory 25

2 Coupled waveguides in Hollow Core Photonic Bandgap Fibre **28**

2.1 Introduction 28

2.1.1 Synopsis 28

2.1.2 Introduction to PCF and PBGF 29

2.2 Photonic Bandgap Guidance 29

2.3 Fabrication 32

2.4 Core-to-core coupling in multi-core HC-PCF 33

2.5 Literature Review 35

2.6 Modelling HC-PGBF 37

2.6.1 Maxwell's Equations 37

2.6.2 Fixed-Frequency Plane-Wave Expansion Method 38
2.6.3 Full-vectorial Finite Element Method 41
2.6.4 FEM Model of a dual-core HC-PCF 43
2.7 Analysis 51
2.8 Discussion 54
2.8.1 Future Work 54
2.8.2 Comparison to Silicon-on-Insulator Waveguide coupling . . 54
2.9 Summary 55

3 Silicon Photonic Wires in the Linear Regime 56
3.1 Introduction 56
3.2 Chromatic Dispersion 57
3.2.1 Material Dispersion 57
3.2.2 Waveguide Dispersion 63
3.2.3 Coupling induced dispersion 64
3.2.4 Slot Modes 67
3.3 Fabrication of Real Devices 68
3.4 Modelling Coupled Silicon Photonic Wires 70
3.4.1 White-Light Interferometry 71
3.5 Experimental Determination of Dispersion 75
3.6 Analysis 77
3.6.1 Waveguide Arrays with Large Separation 77
3.6.2 Waveguide Arrays with Small Separation 82
3.7 Summary 86

4 Silicon Photonic Wires in the Nonlinear Regime: Modulation Instability 87
4.1 Introduction 87
4.2 Optical Nonlinearity 87
4.2.1 Third-Order Susceptibility 88
4.2.2 Nonlinear Schrödinger Equation 90
4.2.3 Modulation Instability 90
4.3 Literature Review 92
4.3.1 Waveguide arrays 98
4.4 Experimental Observation of MI in Silicon Photonic Wire Arrays 99

4.4.1 Waveguide Selection 99
4.4.2 Pulse Generation 101
4.4.3 Bandwidth Selection 102
4.4.4 EDFA 102
4.4.5 Experimental Configuration 103
4.4.6 Autocorrelation 106
4.4.7 Results and Analysis 110
4.5 Subsequent Work 111
4.6 Summary 114

5 Silicon Photonic Wires in the Nonlinear Regime: Spatiotemporal Solitons 115
5.1 Introduction 115
5.2 Background Theory 115
5.2.1 Temporal Solitons 115
5.2.2 Čerenkov Radiation 116
5.2.3 Solitons in Waveguide arrays 121
5.3 Spatiotemporal Soliton Experiments 125
5.4 Subsequent Work 127
5.4.1 Modelling Spatiotemporal Solitons 127
5.5 Summary 131

6 Conclusions and Future Work 132

A Previously Published Work 134
A.1 Journal Publications 134
A.2 Conference Publications 135

References 137

Chapter 1

Optical Waveguides

1.1 Introduction

The work presented throughout this thesis is concerned solely with the guidance of electromagnetic waves along a waveguide in bound modes. Already, I have mentioned many important terms here. It is pertinent at this point, therefore, to discuss some relevant terminology.

1.2 Waveguides and Waveguide modes

A waveguide is quite simply "any structure which confines the propagation of electromagnetic waves along a path defined by the physical construction of the

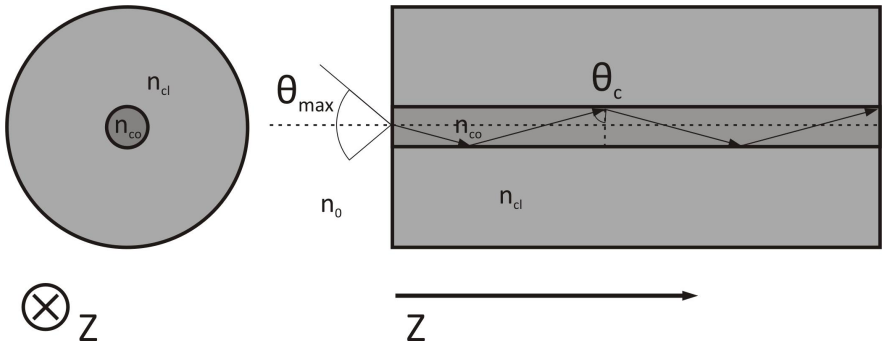

Figure 1-1: A cartoon of a step-index fibre showing a ray trace through the core region. Reprinted from [4].

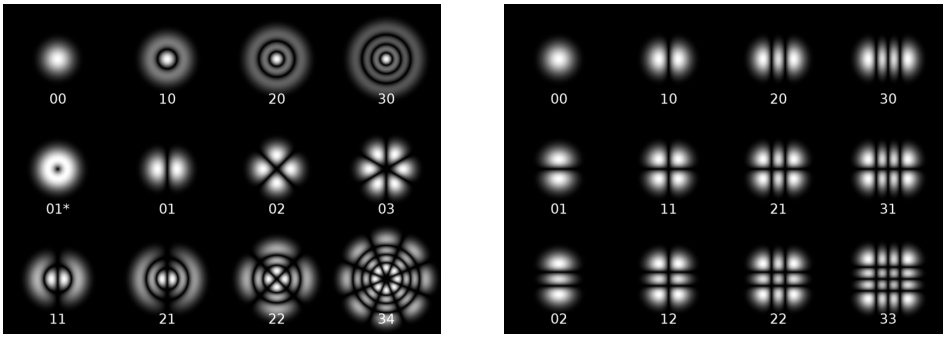

Figure 1-2: Diagrams of the field profiles of low-order modes of both a cylindrical waveguide (left) and rectangular waveguide (right). Both images are reprinted from [6].

waveguide" [5]. The simplest example in optics is the step index waveguide; in which a core region with a higher refractive index is surrounded by a material of a lower refractive index (figure 1-1). The simplest geometry to consider is the cylindrical step-index fibre. In this geometry, the rotational symmetry enables analysis to be undertaken in only two dimensions. The light can subsequently be represented by rays that undergo total internal reflection at the core-cladding boundary as they propagate [1].

Whilst the ray method of determining how light travels in a waveguide is useful, a more complete picture is obtained by thinking about waveguide modes (figure 1-2). In the linear limit, a bound mode is an electromagnetic wave which does not change its profile during propagation, apart from in phase. This phase change is determined by the propagation constant. There are a discrete set of bound modes, propagating without loss, for each given waveguide.

1.3 Maxwell's Equations, the Wave Equation and the Propagation Constant

The transverse electromagnetic field profile, that comes to mind when describing a mode, is an outcome of analysing waveguides using Maxwell's equations [1, 2]. For completeness, let us consider this further by following the analysis presented in the literature. Maxwell's equations, in their macroscopic form are given by:

$$\nabla \cdot \mathbf{B} = 0 \tag{1.1}$$

$$\nabla \cdot \mathbf{D} = \rho \tag{1.2}$$

$$\nabla \times \mathbf{E} = -\frac{\partial \mathbf{B}}{\partial t} \tag{1.3}$$

$$\nabla \times \mathbf{H} = -\mathbf{J} + \frac{\partial \mathbf{B}}{\partial t}, \tag{1.4}$$

where $\mathbf{H}$ and $\mathbf{B}$ are the magnetic field and magnetic flux density, $\mathbf{E}$ and $\mathbf{D}$ are the electric field and electric displacement field respectively, $\mathbf{J}$ is the free electric current density and ρ is the free electric charge density. For the waveguides of this thesis, I shall consider only *source-free* Maxwell equations in non-magnetic media; setting ρ and $\mathbf{J}$ to zero.

Flux densities arise in response to these magnetic and electric fields. Where the relationship between the field and the flux density is linear, the constitutive relations are given by:

$$\mathbf{D} = n^2(x, y)\epsilon_0 \mathbf{E} + \mathbf{P} \tag{1.5}$$

$$\mathbf{B} = \mu_0 \mathbf{H} \tag{1.6}$$

where we have introduced the refractive index, $n(x, y)$ and the polarisability $\mathbf{P}$. By combining these relations with the aforementioned Maxwell's equations we can define a second order wave equation that fully describes the propagation of light in a waveguide:

$$\nabla^2 \mathbf{E} = -\frac{1}{c^2}\frac{\partial^2 \mathbf{E}}{\partial t^2} - \frac{1}{\mu_0}\frac{\partial^2 \mathbf{P}}{\partial t^2} + \nabla\left(\nabla \cdot \mathbf{E}\right) \tag{1.7}$$

Further simplification of this equation can occur by considering propagation in a single direction only, which in the usual formalism is $\hat{z}$. Thus

$$\frac{\partial^2 \mathbf{E}}{\partial z^2} + \nabla_\perp^2 \mathbf{E} = -\frac{1}{c^2}\frac{\partial^2 \mathbf{E}}{\partial t^2} - \frac{1}{\mu_0}\frac{\partial^2 \mathbf{P}}{\partial t^2} \tag{1.8}$$

where we have split the gradient term into constituent components both in, and perpendicular to, the direction of propagation.

In isotropic media, like the waveguides considered in the later chapters of this thesis, the solutions to the wave equation take the form of modes that propagate with a frequency, ω, and propagation constant, β. For a lossless waveguide mode, we can define the electric field as

$$\mathbf{E} = \mathbf{F}(\mathbf{x}, \mathbf{y}) \cos(\beta z - \omega t) \tag{1.9}$$

where $\mathbf{F}$ is the spatial profile, or modal profile, of the waveguide mode. The frequency dependent propagation constant, β, is defined by the refractive index of the medium and the contribution of the physical geometry of the waveguide such that

$$\beta(\omega) = n(\omega) \frac{\omega}{c} \tag{1.10}$$

where $n(\omega)$ is the frequency dependent refractive index of the material, ω the frequency of the propagating wave and c the speed of light in a vacuum.

1.4 Chromatic Dispersion

The frequency dependent refractive index, as described in equation 1.10, leads to a difference in both phase and group velocities for different frequencies of light [2, 4]. This is known as chromatic dispersion, although sometime the term is incorrectly used synonymously with group-velocity-dispersion (GVD) or just dispersion. Consider a medium whereby the refractive index of a red wavelengths is smaller than that of blue wavelengths; the red wavelengths will travel at a faster phase velocity.

This can be expanded further by thinking about the dispersive effects on an optical pulse. Consider a pulse containing some set of frequency components. Due to the chromatic dispersion described above, the higher frequency components have a lower phase velocity than the lower frequency components. The pulse

maximum forms where the wavefronts coincide and it propagates with the group velocity [7], given by

$$\frac{1}{v_g} = \frac{1}{c}\left(n(\lambda) - \lambda\frac{dn(\lambda)}{d\lambda}\right) \tag{1.11}$$

where we know that n is the frequency (or wavelength) dependent refractive index and c is the speed of light in a vacuum. In general this group velocity will also be dependent on wavelength and will yield a group velocity dispersion, a frequency dependency in the rate of change of the amplitude of the pulse envelope. The pulse envelope, in the case of optics, is the slowly varying outline of the minimal and maximal extremes of the electric or magnetic fields.

Mathematically, we can see the effects of chromatic dispersion by considering a Taylor expansion of β around some central frequency ω_0 such that:

$$\beta(\omega) = \beta_0 + \beta_1(\omega - \omega_0) + \frac{\beta_2}{2!}(\omega - \omega_0)^2 + \frac{\beta_3}{3!}(\omega - \omega_0)^3 + ... \tag{1.12}$$

where the dispersion coefficients, β_m are given by the m^{th} derivative of β,

$$\beta_m = \left(\frac{d^m\beta}{d\omega^m}\right)_{\omega=\omega_0}. \tag{1.13}$$

The first two non-constant terms are related to the refractive index through the relationships:

$$\beta_1 = \frac{1}{v_g} = \frac{1}{c}\left(n + n\frac{dn}{d\omega}\right) \tag{1.14}$$

$$\beta_2 = \frac{1}{c}\left(2\frac{dn}{d\omega} + \omega\frac{d^2n}{d\omega^2}\right). \tag{1.15}$$

It can be seen that β_1 is the reciprocal of the group velocity and thus determines the propagation speed of an optical pulse, whereas β_2 yields the rate

at which the different frequency components temporally disperse as the pulse propagates.

Rather than discuss negative and positive values of this group velocity dispersion we use the terms *normal* and *anomalous*. Normal dispersion is where lower frequencies travel faster than the higher frequencies, and β_2 is positive. Anomalous Dispersion is where the higher frequencies travel faster than the lower frequencies, and β_2 is negative. In either case, dispersion usually acts to lengthen a pulse temporarily creating a frequency *chirp* across the pulse, a time dependence of its instantaneous frequency [7].

It is also common, in telecommunications engineering, to talk about the dispersion parameter D, which is related to β_2 by

$$D = -\frac{2\pi c}{\lambda}\beta_2 \tag{1.16}$$

where the sign change denotes that conversely to β_2, negative values of D correspond to normal dispersion.

Finally, the remaining coefficients in the Taylor expansion, β_3 and above, comprise what is known as higher order dispersion (HOD). These provide corrections to the simple parabolic dispersion model. In many cases, their magnitude is negligible, except at wavelengths close to the zero-dispersion wavelength, where the values of β_2 are small. As we shall see in later chapters, the effects of higher-order dispersion in this scenario can be seen far from the zero-dispersion wavelength.

1.5 Attenuation

Unlike the assumptions made in our earlier analysis, no waveguides guide light without a loss of optical power as the mode propagates. Attenuation is generally expressed on a logarithmic scale; in units of dB/km or dB/cm, depending on the application. The attenuation α is given by

$$\alpha = \frac{10}{L} log\left(\frac{P_{in}}{P_{out}}\right) \tag{1.17}$$

where L is the distance along the waveguide and P_{in} and P_{out} are the input power and power at point L respectively. From a mathematical perspective, attenuation, also known as transmission loss, is the manifestation of an imaginary component in the propagation constant, such that $\beta \rightarrow \beta + i\alpha$, which decays the amplitude during propagation.

The contributing factors that make up this imaginary propagation constant are numerous and application dependent. This thesis is concerned with two different waveguide technologies and some distinct loss mechanisms for each technology shall be discussed below.

1.5.1 Photonic Wires

For photonic wires, of any material, the main contributions to optical loss come from either surface roughness remnant from the fabrication process [8–10], optical coupling to an optical substrate [11], and material absorptions [12]. Typical values of absorption are of the order of a few $dB.cm^{-1}$.

For silicon, the material pertinent to the majority of the work in this thesis, we need to consider two further mechanisms that induce loss. Silicon is an indirect bandgap semiconductor with a bandgap of approximately 1.1 eV. Two or more photons with energies below this can combine, in the presence of a phonon, to excite electrons from the valence to conduction bands and generate free carriers [12, 13] (see figure 1-3). This nonlinear absorption can be linked mathematically to optical nonlinearity (See section 1.6) such that

$$n_2 \rightarrow n_2 + i\frac{c\alpha_{TPA}}{2\omega_0} \tag{1.18}$$

where α_{TPA} is the two-photon-absorption (TPA) coefficient and has a typical value of either $0.3 \times 10^{-11}\ mW^{-1}$ [14] or $1.1 \times 10^{-11}\ mW^{-1}$ [15]. More than two photons can combine to overcome the silicon bandgap, resulting in losses such as three-photon-absorption [16], but is not discussed here.

The free carriers generated during propagation, in part by TPA, can themselves both absorb photons, by a mechanism known as free-carrier absorption (FCA), and change material refractive index.

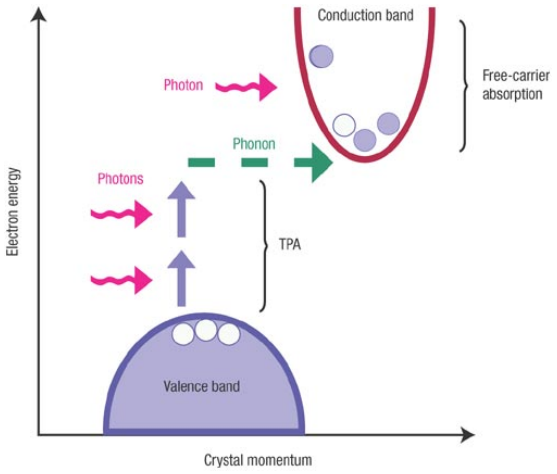

Figure 1-3: Cartoon showing the mechanisms of TPA and FCA in silicon. Reprinted from [13].

1.5.2 Hollow-Core Photonic Bandgap Fibres

Generally, optical loss in silica fibres (fig.1-4) has mainly material contributions. The edges of the silica transparency window (0.25 μm to 2.5 μm) are defined by electronic absorption and absorption by the atomic bonds in silica. Rayleigh scattering, which arises due to density fluctuations frozen into the fibre, fundamentally determines the minimum loss within this transparency window. The equation to describe Rayleigh scattering is dependent on many of the material properties of the guiding medium. It is usually given that

$$\alpha_{Rayleigh} = \frac{8\pi^3}{3\lambda^4} n^8 p^2 k_B T_f \beta_T \tag{1.19}$$

where λ is the wavelength of the incident light, n is the refractive index of the guiding medium, p is the photoelastic constant, k_B is Boltzmann's constant, β_T is the isothermal compressibility and T_f the temperature at which the density fluctuations were frozen into the material [18]. This can be simplified to

$$\alpha_{Rayleigh} = \frac{C_R}{\lambda^4} \tag{1.20}$$

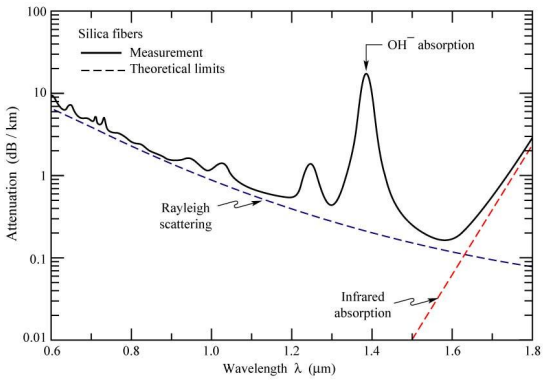

Figure 1-4: Attenuation in SiO_2 fibres (solid line) overlaid by the fundamental limits imposed by infrared absorption and Rayleigh scattering (red and blue dashed lines respectively). The absorption from the second harmonic of the OH-vibration, at 1380 nm, is clearly seen. Reprinted from [17].

where C_R can take a typical value of $0.7 - 0.9$ $(dB.\mu m^4)/km$ for silica fibres [2,18]. From this equation is is clear that Rayleigh scattering increases drastically as propagating wavelengths approach sizes comparable to those of the density fluctuations.

Across this transmission region, resonances from impurity ions add further losses. In particular, OH- ions have a fundamental absorption close to 2.7 μm, with several higher harmonics also contributing to loss at other wavelength inside the transparency window.

One of the driving forces to develop air-guiding fibres is the possibility to avoid the losses associated with silica. In a standard hollow-core photonic crystal fibre 99% of the light resides in the air core. Initial predictions suggested losses lower than the current minimum loss fibres used for long-haul telecommunications networks ($0.2dB/km$) could be achieved. However, the introduction of the hollow core means the fibre inherits new loss mechanisms.

Firstly, the finite extent of a microstructured cladding allows tunnelling or confinement loss, where the exponential tail of the guided mode extends beyond the microstructured cladding. Analysis of the current generation of fibres suggests that above a certain number of periods of cladding holes, this effect is negligible. Secondly,during fabrication, surface capillary waves at the air-silica interface become frozen into the silica as it cools through the melting point. The presence

of this surface roughness couples light out of the guided core mode into lossy cladding modes [11, 19]. Finally, depending on the geometry of the core-cladding boundary, modes localised to the glass core surround, called surface modes, can exist. They are high loss due to an increased overlap with the cladding modes and from having the majority of their energy inside the silica. The overlap between the scattering from core modes to cladding modes via surface modes is much larger than when surface modes are not present. Although the wavelengths comprising these modes exist within the bandgap of the fibre and limit the useful bandwidth, they can be shifted spectrally by employing innovative fabrication techniques [20].

1.6 Nonlinearity

In the earlier consideration of a propagating optical mode, only a linear relationship between the applied field and dielectric polarisation was considered, such that

$$P = \epsilon_0 \chi E. \tag{1.21}$$

where ϵ_0 is the permittivity of free space, χ is the linear electric susceptibility and E is the applied field. This is an excellent approximation for weak fields, as the higher order terms are negligible. In general, however, the dielectric polarisation is not proportional to the applied field and for strong fields we cannot continue to use this assumption.

Physically, this relates directly to the breakdown of Hooke's Law. Electrons within the valence band of a material are displaced only a short distance from the atomic nucleus when excited by low intensity electric fields. Let us consider a simple Lorentz model under these conditions, where the restraining elastic force is proportional to the displacement and the equilibrium displacement is proportional to the applied field [21]. In this case the medium is linear, and P is related to E as per equation 1.21. When electric fields are of high intensities, the restoring force on the valence band electrons becomes aharmonic, and is not explained by the previous analysis. If we expand P in a Maclaurin series such that:

$$P = \epsilon_0 \left(\chi^{(1)} E + \chi^{(2)} E^2 + \chi^{(3)} E^3 + \cdots \right) \tag{1.22}$$

where $\chi^{(m)}$ represent both the linear and non-linear susceptibilities of the medium. It is observed that the polarisation is now not linear with the applied field but it expands as a power series of the applied field.

1.6.1 Kerr Nonlinearity

The nonlinear relationship between polarisation and electric field gives rise to some interesting effects. The first term in equation 1.22 describes linear dispersion, as discussed in the preceding chapters. The second term, describes the Pockel's effect and the third describes Kerr Nonlinearity.

For Silicon, it is important to simplify the above equation. In general, $\chi^{(j)}$ is a tensor of rank $j+1$. It can be treated as scalar if it is assumed that only one field is applied [16]. Both silicon and silica have inversion symmetry meaning they do not have a preferred direction for their polarisability. All the even exponent terms in equation 1.22 are therefore zero. Finally, terms with an odd exponent higher than $\chi^{(3)}$ can be assumed negligible.

The induced polarisation can therefore be written in the following form

$$P = \epsilon_0 \left(\chi^{(1)} E + \chi^{(3)} E^2 E \right). \tag{1.23}$$

Substituting into the electric displacement equation yields

$$\vec{D} = \epsilon_0 \vec{E} + \vec{P} = \epsilon_0 n^2 \vec{E}. \tag{1.24}$$

Here we have defined the total refractive index, n, as [2]

$$n \left(\omega, \left| \vec{E} \right| \right) = n_0 + \tilde{n}_2 \left| \vec{E} \right|^2 \tag{1.25}$$

where n_0 is the linear refractive index contribution and $\tilde{n}_2$ is the nonlinear refractive index, the term conventionally used to describe nonlinearity. The nonlinear refractive index is a coefficient describing a proportionality between optical intensity and refractive index, known as the *Kerr Effect*. When high intensity waves travel through a nonlinear medium the refractive index changes depending on this intensity; the rate of change being determined by the nonlinear refractive index. Given this description involving intensity, we can also use the more common mathematical description of nonlinearity [22]

$$n = n_0 + n_2 I \tag{1.26}$$

where n_2 is also a nonlinear refractive index and I is the time-averaged intensity given by $I = 2n_0\epsilon_0 c\,|E|^2$. For silicon the nonlinear refractive index, n_2, has a value of between $10^{-18}\ m^2W^{-1}$ and $10^{-17}\ m^2W^{-1}$ [14, 15], whilst for silica it is much smaller around $3 \times 10^{-20}\ m^2W^{-1}$ [23].

1.6.2 Self-Phase Modulation

By considering a high intensity pulse travelling in a Kerr medium, we can observe one of the main manifestations of the Kerr effect; self-phase modulation (SPM). As a summary, Kerr nonlinearity leads to the generation of a intensity dependent phase shift across a pulse which in turn leads to the generation of new spectral components. The front end of the pulse is red-shifted whilst the trailing edge is blue-shifted. After propagating in such a medium, the spectrum is broadened whilst the temporal pulse shape remains unaffected.

Let us consider this in slightly more detail. To simplify our analysis we shall ignore the dispersive effects discussed in section 1.4; and set β_2 and all higher order dispersive terms to zero. Given this scenario, the governing equation of pulse dynamics is the nonlinear phase shift equation [2, 24]:

$$\frac{\partial U}{\partial z} = ie^{i\alpha z}\gamma P_0 |U|^2 U \tag{1.27}$$

where U is a normalised envelope function, P_0 is the peak power, γ is a nonlinear parameter related to n_2 through $\gamma = n_2\omega/cA_{eff}$, and α accounts for losses during propagation. This equation has standard solutions of the form

$$U(L,T) = U(0,T)e^{\phi_{NL}(L,T)} \tag{1.28}$$

where $U0,T$ is the amplitude of the pulse envelope at $z = 0$ and ϕ_{NL} is the nonlinear phase shift given by

$$\phi_{NL}(L,T) = |U(0,T)|^2\gamma P_0 L_{eff}. \tag{1.29}$$

We have introduced the effective length, L_{eff}, which plays the role of the length, adjusted to take into account of propagation losses [2].

The solutions to equation 1.27, given by equation 1.28, shows that the temporal profile of the pulse is independent of the effects of SPM. They only add an intensity dependent phase shift, ϕ_{NL}, across the pulse, which grows with increasing propagation distance. This change in nonlinear phase across the pulse generates new frequencies of light, detuned from the central frequency of the pulse, given by

$$\delta\omega(T) = -\frac{\partial\phi_{NL}}{\partial T} = -L_{eff}\gamma P_0\frac{\partial}{\partial T}|U(0,T)|^2. \tag{1.30}$$

These new frequencies are continuously generated during propagation.

A simple example can be shown with a Gaussian pulse (fig. 1-5). The value of $\delta\omega$ at the leading edge of the pulse (with negative values of T) is negative, shifting the frequencies to lower values (red-shifting). At the trailing edge of the pulse, $\delta\omega$ is positive, shifting the frequencies to higher values (blue-shifting). Given an initially unchirped pulse, the new frequencies broaden the spectrum from its initial width, at $z = 0$ and induce a frequency chirp across the pulse (central plot in fig. 1-5).

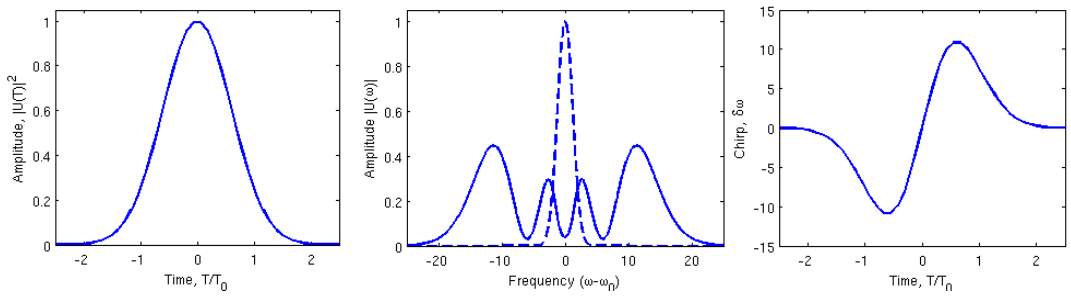

Figure 1-5: Figure showing the temporal (left) and spectral (centre) profiles of a Gaussian pulse given a phase shift of $\phi_{NL} = 3.5\pi$. The chirp associated with this phase shift is shown in the figure on the right. For comparison, the spectral profile of the Gaussian pulse with zero phase shift is also shown (blue dashed line in centre figure). Calculation performed using SSPROP [25].

1.6.3 Dispersion and SPM

On a more practical note, it is usually unreasonable to ignore dispersive effects when we consider pulse propagation. Qualitatively the results of combining both effects is different depending on whether we are in the normal or anomalous dispersion regime and on the chirp of the input pulse.

First we shall consider an unchirped pulse propagating in a normally dispersive medium where the relative importance of SPM and GVD are similar. What we would observe is that in the presence of SPM a pulse travelling in a normally dispersive medium would lengthen much more rapidly than if there was no SPM present. This can be understood by noting that at the front of the pulse, the frequency components are red-shifted. These red-shifted components travel faster in the normal dispersion regime leading to an enhancement of the pulse lengthening when SPM is present. This rapid pulse lengthening leads to a smaller than expected spectral broadening due to the decrease in peak intensity.

Let us consider the same unchirped pulse considered in the previous case but propagating in the anomalous dispersion regime. In this case it might be expected that the pulse lengthening will be at a much lower rate than in the absence of SPM. At the same time, the spectrum broadening will be either much reduced or possibly even negative, denoting a spectral narrowing. This can be understood by noting that the two mechanisms yield chirp of opposing signs. The specific behaviour will depend on the relative strength of the GVD and SPM effects, and

the initial pulse shape. It is this scenario that will be discussed in more detail in section 1.6.4 on solitons.

Finally we shall discuss chirped pulses. If we consider a pulse which has some initial chirp on it, this chirp can be removed by flattening the spectral phase. As we have seen already in this chapter, applying the correct sign of chromatic dispersion can reduce this phase. In doing so they will reduce the duration, to the minimum value (whereby we have bandwidth-limited pulses). this regime is used for nonlinear-pulse compression techniques where the initial chirp is the result of a nonlinear interaction such as SPM [7, 26, 27].

1.6.4 Solitons

We have already discussed the interplay between SPM and GVD and alluded to their interplay when the dispersion is anomalous. Under certain circumstances the frequency chirp generated by SPM can be completely compensated for by anomalous dispersion. The resulting pulses propagate without changing either temporally or spectrally during propagation along a waveguide and are known as *fundamental optical solitons*. Anomalous dispersion lengthens initially transform-limited pulses. However, in the case where there is an initial positive chirp, like that imposed by SPM, the pulse will look to be compressed. Another way of thinking about it is that SPM red-shifts the frequency components at the front of the pulse and blue-shifts the frequency components at the tail, the anomalous dispersion redistributes these frequencies, pushing the blue-shifted components to the front of the pulse where they are red-shifted. This latter description is not quite true in that it seems to show oscillatory behaviour. In practice both of these effects occur at the same time and the pulse shape is maintained.

The requirements for such a compensation is that the pulses have a *sech-shaped* envelope function, such that:

$$A(T) = \sqrt{\frac{|\beta_2|}{T_0^2 \gamma}} \mathrm{sech}\left(\frac{T}{T_0}\right). \tag{1.31}$$

where this solution comes from the nonlinear Schrödinger equation, which is discussed in more details in Chapters 4 and 5.

The above solutions are temporal optical solitons. We refer only to temporal solitons here, as in a single waveguide the balancing effects confine the soliton in the time domain only. The transverse confinement is not a function of the propagation but of the waveguide itself. In the final chapter, on spatio-temporal solitons, we shall discuss a situation when this is not the case.

1.7 Waveguide Arrays and Coupled Mode Theory

The experimental work presented in this thesis deals with arrays of strongly coupled silicon waveguides and the linear and non-linear propagation phenomena observed. The presence of a secondary waveguide at a close enough spacing to perturb the guided mode leads to coupling of the power from one waveguide into the other.

There are two different descriptions of this effect. The first is to consider the modes of each individual waveguide and consider that the power transfers between the modes of one waveguide and its neighbour. The other is to think of the whole coupled array as a single structure. An array of N waveguides will have N modes of a given polarisation. These modes, known as supermodes, have different propagation constants and the superposition of them yields the observed spatial field and power transfer effect as discussed in the first description of this system.

The interesting point here is how to calculate the fields of the supermodes. Coupled mode theory (CMT) was first developed heuristically in the early 1950's. Rigorous equations were then established for microwave oscillations using mode expansion [28] and a variational principle [29]. CMT was then introduced into guided-wave optics in the 1970's [30–32]. Conventional CMT, as it is known, is entirely based on the modes of individual waveguides. Once these modes are determined, the amplitudes of the modes in the coupled-waveguide systems are governed by coupled-mode equations.

To introduce the coupled mode formalism, we consider the modes of a 2-channel waveguide array, with amplitudes a_1 and a_2, and implicit time dependence of $\exp(i\omega t)$ as described in [33]. When the waveguides are far apart the

mode amplitudes obey the equations

$$\frac{da_1}{dz} = -i\beta_1 a_1 \tag{1.32}$$

$$\frac{da_2}{dz} = -i\beta_2 a_2 \tag{1.33}$$

and the modes will propagate independently, with propagation constants β_1 and β_2 respectively. When the waveguides are brought close together the spatial dependence of each mode will be modified by the existence of the other. In the case of weak coupling, the coupling takes the form

$$\frac{da_1}{dz} = -i\left(\beta_1 + \kappa_{11}\right) a_1 - i\kappa_{12} a_2 \tag{1.34}$$

$$\frac{da_2}{dz} = -i\left(\beta_2 + \kappa_{22}\right) a_2 - i\kappa_{21} a_1 \tag{1.35}$$

where κ_{xx} and κ_{xy} are the self- and mutual- coupling coefficients between the modes [33]. Making the assumption that the modes are lossless, yields the total power in the system as $P(z) = |a_1|^2 + |a_2|^2$. By applying the law of power conservation we obtain the relation that

$$\kappa_{12} = \kappa_{21}^* = \kappa \tag{1.36}$$

and that all κ_{xx} have to be real. For the simple case of uniform couplers, both the coupling coefficients and propagation constants are invariant with propagation and equations 1.34 and 1.35 can be solved analytically by transforming them such that

$$\frac{da_1}{dz} = -i\delta\hat{a}_1 - i\kappa\hat{a}_2 \tag{1.37}$$

$$\frac{da_2}{dz} = -i\delta\hat{a}_2 - i\kappa\hat{a}_1 \tag{1.38}$$

where

$$\delta = \frac{\beta_1 + \kappa_{11} - \beta_2 - \kappa_{22}}{2} \tag{1.39}$$

is the phase-mismatch factor and

$$a_i(z) = \hat{a}_i \exp\left(-i\frac{\beta_1 + \kappa_{11} + \beta_2 + \kappa_{22}}{2}z\right) \tag{1.40}$$

simplifies the equations by removing the common phase factor [33].

This conventional CMT was formulated to be valid for weak-coupling and power-orthogonal modes only. It has received more rigorous analysis to yield both scalar non-orthogonal coupled-mode equation [33] and vectorial coupled mode theory [34]. Orthogonality is not discussed further as the analysis discussed in later chapters is based on numerical simulations, not the formalism presented within this section.

Chapter 2

Coupled waveguides in Hollow Core Photonic Bandgap Fibre

2.1 Introduction

2.1.1 Synopsis

Unlike the remainder of this thesis, this chapter does not describe silicon based photonics. Other technologies, such as optical fibres, are also able to support coupled waveguides with non trivial coupling coefficients. This chapter considers coupling between two hollow-cores in a multi-core hollow-core photonic crystal fibre (HC-PCF). Comparisons will be made, to the silicon waveguides studied elsewhere.

The chapter will commence with an introduction to photonic crystal fibres (PCF), sometimes called microstructured fibres or holey fibres. The chapter will then discuss the guidance mechanism for confining light in an air core; where conventional total internal reflection (TIR) is not possible. Fabrication techniques will be explained with particular reference to the stack and draw method used herein to produce multi-core HC-PCF.

The chapter will then progress to a literature review of the current work on multi-core photonic crystal fibres. The sub-chapters following this represent the authors work modelling a multi-core HC-PCF. The model was based on a fibre fabricated at the University of Bath by Brian J. Mangan.

2.1.2 Introduction to PCF and PBGF

An optical fibre is a cylindrically symmetric flexible glass waveguide that guides light inside a core medium, surrounded by a cladding medium. The central core region has a refractive index that is usually higher than the cladding region that surrounds it, creating a step in refractive index. Fibres with this geometry guide light through total internal reflection (TIR). Guiding light by TIR can be described by considering a light ray that is incident on an interface to a low index material from a higher index material. If the angle of incidence, the angle between the ray and the normal to the interface, is above a critical angle then the wave is completely reflected by the interface.

In 1996, a new generation of optical fibres were reported [35], Photonic Crystal Fibres (PCFs). These fibres have a cladding region comprising of a periodic array of air holes that run down the length of the fibre, generating a two-dimensional photonic crystal. Other types of fibre comprising of a cladding made of air holes have also been produced; these microstructured fibres, or holey fibres, may not necessarily have a periodic cladding structure. These fibres will not be discussed further.

PCFs can also display guidance mechanisms far different from the TIR guidance exhibited by conventional fibres. The requirement of the core region having a higher refractive index than the cladding can be lifted; allowing fibres to be fabricated with a core material of a lower refractive index than the cladding region. In this case, the light guided solely by a property of the cladding; the presence of a photonic bandgap.

2.2 Photonic Bandgap Guidance

Photonic-bandgap fibres (PBGF), a subset of photonic crystal fibres (PCF), are fibres in which the guidance mechanism relies on the optical properties of the periodic two-dimensional array of air holes that makes up the cladding region of the fibre. The periodicity gives rise to a photonic bandgap; a set of photonic states that are forbidden to exist in the cladding. A bandgap can exist both in the plane of the periodicity, as has been exploited in silicon photonics [36, 37], or perpendicular to it as employed in PBGF. For the remainder of this chapter we

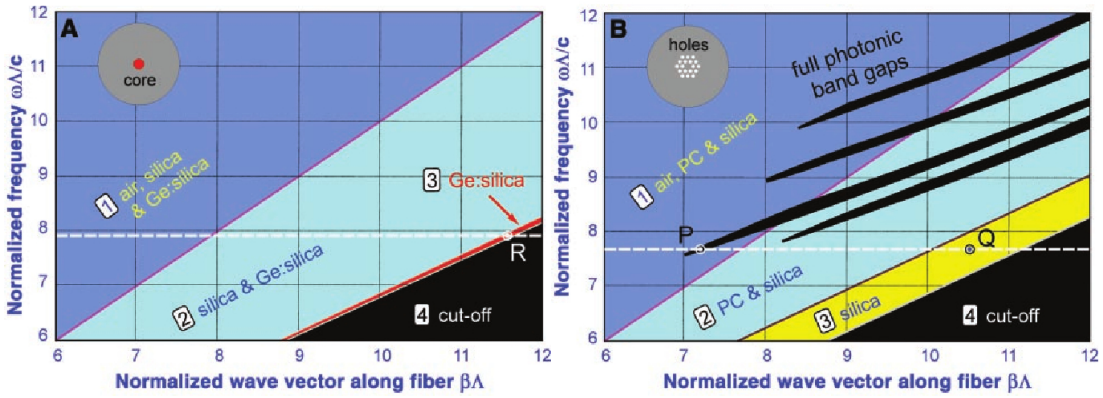

Figure 2-1: *(a)* Propagation diagram for a single mode fibre guiding via total internal reflection. Guided modes from at R where light is free to travel in the core but are totally reflected at the core cladding interface. The regions 1 through 4 are discussed in the text. *(b)* Propagation diagram for a fibre consisting of a triangular lattice of air holes (inset). The same features can be seen for the index guiding fibre but with the inclusion of black fingers. These represent the regions where the full two-dimensional photonic bandgap exists (see fig2-2). Reprinted from [39]

are, quite naturally, only going to consider out-of-plane propagation.

To understand bandgap guidance let us take a step back and consider guidance in a step-index fibre, consisting of a doped silica core and silica cladding, suspended in air [38, 39], with the doped core having a higher refractive index than the cladding. The structure is invariant along its length, meaning that any interfaces between materials are parallel to this direction of propagation. When light encounters these interfaces, the wavevector parallel to the interface is conserved [1]. This wavevector, k_z, is also known as the propagation constant, β. In a homogeneous medium the value of this propagation constant can take a continuum of values up to a maximum; when the wave travels completely in the direction of propagation, and has a value of nk_o, where k_0 is the free space wavevector and n is the refractive index of the medium.

Given our step-index fibre structure there are four different propagation regimes (see fig. 2-1(a)):

1. $\beta < nk_0$ in all media and the light may propagate in any of the materials.

2. $\beta < nk_0$ only within the fibre cladding and fibre core. The light is forbidden

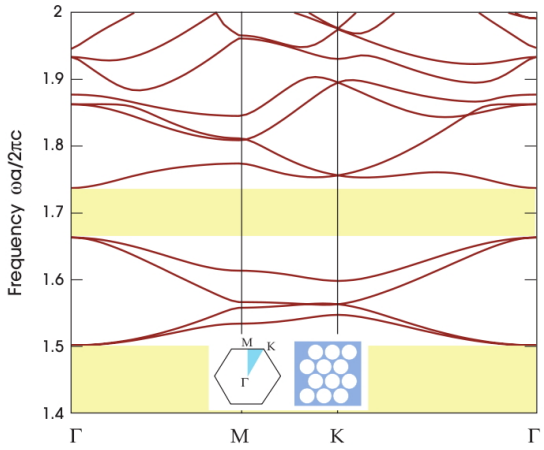

Figure 2-2: Band diagram versus in-plane wave vector in the Brillouin zone of a triangular lattice of air holes. The lower of the two gaps corresponds to the index guiding region of the core defect whilst the upper gap corresponds to a bandgap inside the light cone. Here guidance in an air core would be allowed as it crosses the light line $k = w_0/c$. Reprinted from [40].

to travel in the air because $\beta < n/k_0$ and total internal reflection at the material interface prevents light from entering that medium.

3. $\beta < nk_0$ only inside the core. β is now too large to exist even inside the cladding. It is this region that is used for conventional telecommunications. Any mode guided by the core has a propagation constant defined by $n_{cladding}k_0 < \beta < n_{core}k_0$. In general, light becomes confined to regions of higher refractive index due to total internal reflection.

4. $\beta > nk_0$ for all media and light is forbidden to propagate within the system described.

Consider the same type of fibre but with a set of cladding holes in a photonic crystal arrangement within the cladding (as depicted in the inset in figure 2-1(b)). The regions described above also exist within this case, but there appear some fingers within the plot. They are bandgaps that appear due to the periodicity of the cladding holes and show a range of β values for which the microstructured cladding does not support guidance. The origin of such bandgaps is that for a given β value the solution to Maxwell's equations within the photonic crystal are Bloch modes [40]. Superposing the Bloch modes over the entire reciprocal space

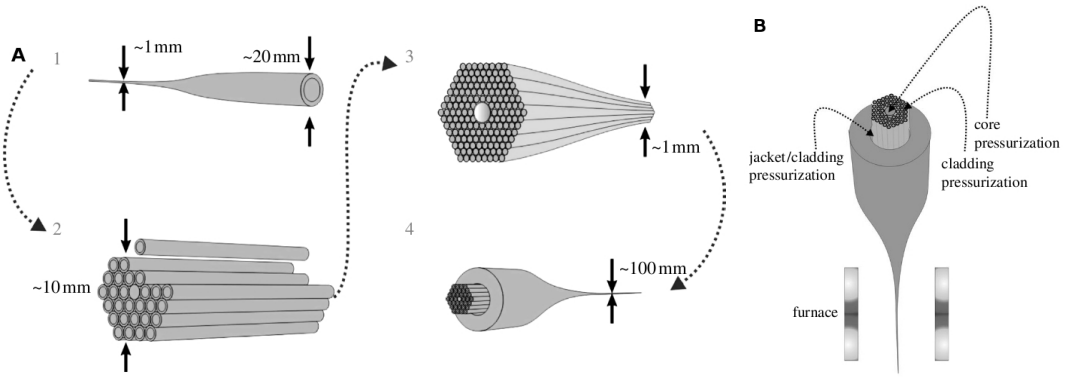

Figure 2-3: (**A**) Schematic of the stack and draw fabrication process. (1) Glass tubes are drawn down into thin capillaries. (2) These are stacked in a triangular lattice arrangement to create a "stack" with a core defect. (3) The stack is drawn down into "canes". (4) The canes are jacketed and drawn to fibre using differential pressure (**B**). Reprinted from [42].

yields a two dimensional band structure (fig. 2-2). The gaps present within this bandstructure only stay open for a given range of β.

If the holes that comprise the photonic crystal cladding have the correct properties the bandgap can open when β is not too large and can therefore extend above the light line of air [40]. In this case, if a hollow defect were to be placed in such a cladding the air within the core could support modes of a given range of β that is confined to the core by the bandgap present in the cladding.

2.3 Fabrication

Fabrication of many PCF, and other "holey fibres", follows a common stack-and-draw procedure [41]. Extrusion, and other methods, are also used for different types of microstructured fibre, but are not common for photonic bandgap fibre. The stack-and-draw procedure consists of first drawing a tube of fused silica glass down to hundreds of capillaries with a diameter of approximately 1 mm. These are then stacked in in a triangular lattice in the cross sectional plane in what is known as a "stack" (fig:2-3a).

To create a hollow core fibre, a hexagonal section from the centre of the stack is removed. Usually this is replaced with a larger capillary, known as a core-tube, that just fits the remaining hole in the lattice [41]. This increases

integrity during the drawing process, but the extra glass increases the number of lossy modes supported by the core-wall structure. There is no necessity for this fabrication step, and by removing the core-tube from the process, and holding the cladding capillaries in place by another means, the interaction between core and core-surface modes can be removed from the bandgap [20, 43, 44]. Although the increased spectral width of the bandgap for an idealised core is evident, due to less core modes in the bandgap region, the structural integrity of the core during fabrication is lessened and needs to be monitored closely.

The stack is then jacketed in a larger tube to add mechanical strength. A packing of glass rods is used to fill the air gaps between the stack and the inner wall of the jacket. This reduces deformation of the cladding structure during the drawing process. The stacks are drawn down to "canes" a few millimetres in diameter before being jacketed for a second time with a thicker glass tube, to increase the total glass volume, whence they are drawn down to fibre with a typical diameter of a few hundred microns.

One requirement, for bandgap guidance, on most HC-PBGF is that the air filling fraction of the cladding is high, of the order of 80%. Careful choice of the glass capillaries used in the stack is not enough to control the air filling fraction of the final fibre. As the fibre is being drawn the air holes within the cladding have a propensity to collapse due to the increased effect of surface tension at the glass air interface. This needs to be counteracted by a force directed outwards [45]; usually accomplished experimentally by the process of differential inflation (fig:2-3b). This method applies gasses at different pressures to the different regions of the fibre: vacuum between the outside of the cane and the jacket to remove all the air between the capillaries; a pressure P_{cladd} is applied to the cladding structure region; and a pressure P_{core} to the fibre core region. For multi-core fibres it is important to note that the cladding will not be uniform enough for a single pressure to generate nominally identical cores. Therefore separate pressures must be applied to each core and controlled independently.

2.4 Core-to-core coupling in multi-core HC-PCF

Many textbooks on waveguide optics [1, 46, 47] will introduce the coupling of waveguides via the overlap of the wavefunctions of each core. In the most part,

this is true of any coupled waveguides as long as their separation is finite and the evanescent tails of the guided modes are non-zero. The only thing that changes for larger separation is the strength of this coupling, and thus the distance over which the light needs to extend to couple completely to the adjacent waveguide.

Applying scalar wave theory to this problem shows that adjacent waveguides can never be decoupled. The formalism outlined by Someda [48] involving integration over the positive half-plane and applying Green's Theorem yields the resultant equation:

$$\left(\beta_1^2 - \beta_2^2\right) \int_0^\infty dx \int_{-\infty}^\infty dy \psi_1 \psi_2 = \int_{-\infty}^{infty} \psi_1 \left(\frac{\partial \psi_2}{\partial x}\right) \Bigg|_{x=0} dy \tag{2.1}$$

where the even (odd) supermode has a propagation constant β_1 (β_2) and a wavefunction ψ_1 (ψ_2). The wavefunctions are both even with respect to y and have even partial derivatives with respect to x. Here, x is the direction coupling the waveguides, with light propagating in the z-direction. The right hand side of equation 2.1 can never go to zero and as such $\beta_1 \neq \beta_2$ must always be true and the waveguides must always be coupled.

Scalar equations, however, are an approximation to the full picture. Vector theory shows that adjacent waveguides can be made to decouple by shaping the index of any intermediate anti-guiding region between the waveguides [48–50]. For electromagnetic waves, and other vector fields, there is a distinction between odd and even modes. Let us consider TE modes only, by which we mean that the main component of the electric field is in the direction adjoining the two adjacent waveguides. In this case, the Maxwell equations for the even supermode are:

$$\nabla \times E_1 = -j\omega\mu H_1 \tag{2.2}$$

$$\nabla \times H_1 = j\omega\epsilon E_1 \tag{2.3}$$

Using the analysis outlined by Someda [48] the result is:

$$j\left(\beta_1 - \beta_2\right)\int_0^{\infty} dx \int_{-\infty}^{\infty} dy \left(E_1 \times H_2^* + E_2^* \times H_1\right) \cdot e_z$$
$$= \int_{-\infty}^{infty} E_1 \times H_2^* \cdot e_x \Big|_{x=0} dy \quad (2.4)$$

where e_x and e_z are unit vectors in the $x-$ and $z-$ directions. Now, the equality $\beta_1 = \beta_2$ can be satisfied when

$$\int_{-\infty}^{infty} \left(E_{1y} H_{2z}^* - E_{1z} H_{2y}^*\right) dy = 0 \quad (2.5)$$

In order to satisfy this condition, it is necessary to introduce independence between field components. This can be done, according to the literature, by making the medium between the guides inhomogeneous [48].

2.5 Literature Review

A cladding comprised of a periodic medium, like that present when using a microstructured fibre, can create the inhomogeneity required for complete decoupling of adjacent waveguides. Theoretical analysis of the coupling between core modes for non-uniform, and non-physical, cookie-cutter cores in a photonic crystal fibre has been performed [51]. The resulting eigenmodes of the PBGF were treated as combinations of Gaussian-like air-core modes and surface modes, residing at the core-cladding interface. The dispersion of the eigenmode is steeper for even TE polarised modes, causing the dispersion curves to cross those of the odd modes; decoupling the two. It was found that the point at which this decoupling occurs can be shifted across the bandgap by changing the radius of their core region, r_c.

For conventional fibres, those that are index guiding, the coupling length, L_c has two general properties. Firstly it increases monotonically with frequency and core separation. Secondly, the effective index of the even supermode is always greater than that of the odd supermode. This is because the fundamental modes of the individual cores have positive phase everywhere, yielding a positive overlap.

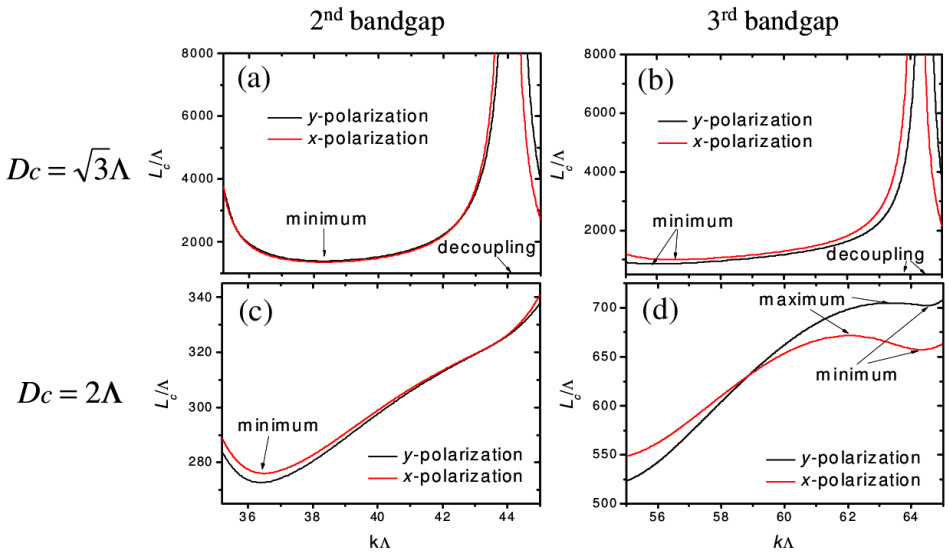

Figure 2-4: Graphs of coupling Length, L_c, as a function of normalised frequency. Results for two different core-core geometries and in the first two bandgaps of a multi-bandgap all-solid silica band-gap fibre. Reprinted from [52].

This makes it impossible to engineer the dispersion as required to decouple the cores. However, the complicated structure of a HC-PCF, whereby the core index is lower than the material index of the cladding lifts this prohibition. The fundamental guided modes of the core are no longer the fundamental guided modes of the fibre.

All-solid PBGF, comprising of high-index germanium-doped rods in a pure silica matrix [52] has been used to validate these early theoretical predictions. Complete decoupling, and supermode ordering reversal were observed (fig. 2-4). This work concentrated on the field distributions of the first ring of high-index rods that surround the core, and the decoupling is described in terms of an avoided-crossing effect between a supermode of the dual core and the modes of the inter-core rods. The coupling lengths were measured experimentally using a standard cut-back method.

To my knowledge, no experiments of this type have been made using hollow-core photonic crystal fibres with an air-silica matrix cladding.

2.6 Modelling HC-PGBF

The following sections describe work done by me in modelling the linear properties of dual-core hollow core photonic crystal fibres. It is split into two sections. Firstly the properties of the cladding are calculated using a fixed-frequency plane-wave expansion (FFPW) method, developed at the University of Bath by Greg Pearce. A full-fibre model is then generated and analysed inside a full vector finite element method package (Comsol Multiphysics and RF module) to calculate the properties of the core modes. These will be discussed in detail in the following sections.

2.6.1 Maxwell's Equations

We have already looked at Maxwell's equations in Chapter 1. If we consider a waveguide that is uniform along its length we can separate the electric and magnetic fields into their Cartesian coordinates, with the z-direction defining the direction of propagation such that

$$\mathbf{E}(x,y,z) = \mathbf{e}(x,y)\exp(i\beta z) \tag{2.6}$$

$$\mathbf{H}(x,y,z) = \mathbf{h}(x,y)\exp(i\beta z) \tag{2.7}$$

Further analysis, by decomposing the fields into longitudinal and transverse components, leads to the following relation that equates the transverse components of the wave equations such that [1]:

$$\left(\nabla_t^2 + n^2k_0^2 - \beta^2\right)e_t = -\nabla_t\left(e_t \cdot \nabla_t \ln n^2\right) \tag{2.8}$$

$$\left(\nabla_t^2 + n^2k_0^2 - \beta^2\right)h_t = (\nabla_t \times h_t) \times \nabla_t \ln n^2. \tag{2.9}$$

By solving either one of the above equations it is possible to obtain all field components by substitution into Maxwell's equations. It is customary to use the **H** field for calculation due to the fact it is a continuous quantity across all boundaries in a material. If h_t is known, then the remaining fields are calculated from [1]:

$$h_z = \frac{i}{\beta}\nabla_t \cdot h_t \tag{2.10}$$

$$e_z = i\left(\frac{\mu_0}{\epsilon_0}\right)^{1/2} \frac{1}{k_0 n^2}\hat{z}\cdot\nabla_t \times h_t \tag{2.11}$$

$$e_t = -\left(\frac{\mu_0}{\epsilon_0}\right)^{1/2} \frac{1}{k_0 n^2}\hat{z}\times(\beta h_t + i\nabla_t h_z) \tag{2.12}$$

Thus, solutions to either eq. (2.8) or eq. (2.9) provide a complete description of the electromagnetic fields.

2.6.2 Fixed-Frequency Plane-Wave Expansion Method

The fixed-frequency plane-wave expansion modelling used within this thesis was devised within the Department of Physics and written by Greg Pearce. In the code, the solutions are found using algorithms based on iterative eigensolvers and fast Fourier Transform techniques. Below we will outline the function of the code: a full explanation, which is not presented here, can be found from the manual [53] or its author's thesis [38]. We will continue our discussion with a précis of his analysis.

In the fixed-frequency method frequency is fixed through k_0 and the eigenvalue solutions are the set of allowed β^2 values found from

$$\left(\nabla_t + n^2 k_0^2 + \nabla_t \ln n^2 \times \nabla_t \times\right) h_t = \beta^2 h_t \tag{2.13}$$

for which a generalised eigensolver is required to generate a set of solutions [53].

Plane-wave methods use expansions of fields and dielectric functions in the form of plane waves. The only requirement is that the structure , and hence the dielectric function, is periodic. The manipulation of Maxwell's equations determines that this periodicity is necessary in the transverse plane only [38].

Using the reciprocal lattice vectors [54], the dielectric function may be expanded in a plane-wave basis as

$$n^2(x) = \sum_G n_G^2 e^{iG\cdot x}, \tag{2.14}$$

where $\mathbf{G}$ are reciprocal lattice vectors and $\exp(i\mathbf{G}\cdot x)$ are the basis plane wave functions [53]. Bloch's Theorem states that a field resulting from a periodic 'potential' can also be written as a sum over plane waves with the inclusion of a Bloch vector $\mathbf{k}$

$$h_m(x) = \sum_G k_{m,k,G} e^{i(k+G)\cdot x} \tag{2.15}$$

The sets of coefficients n_G^2 and $k_{m,k,G}(mx, y)$ represent n^2 and h_t in reciprocal space and these coefficients completely describe the dielectric function and transverse magnetic field. Substitution of these two summations into eq. (2.13) yields the reciprocal space form of the vector wave equation. It is this matrix equation that is solved to yield the properties of the cladding.

Modelling a PCF cladding using the FFPW method

In this thesis, we model a dual-core HC-PCF. The main analysis is done using finite-element analysis, as discussed in later chapters. However, the simplicity of the FFPW code available at the University of Bath made it a good choice for quickly determining the physical parameters of the cladding.

The model itself uses a single unit cell (fig. 2-5a) to represent an idealised cladding (fig. 2-5b). Rectangles of length, l, and thickness, t, are centred on a single point, along the directions of a hexagonal lattice. Circles are then placed at the point of intersection between adjacent rectangles. The perimeter of the composite shape defines the edge of the air region of the cladding, and the resulting struts and interstitial glass regions (grey region of figure 2-5a). During fibre fabrication, pressure and surface tension fluctuate across the plane of the cladding. These fluctuations yield small dimensional changes in each of the cells within the resultant cladding with respect to the idealised unit cell making a fabricated cladding non ideal but effectively ideal.

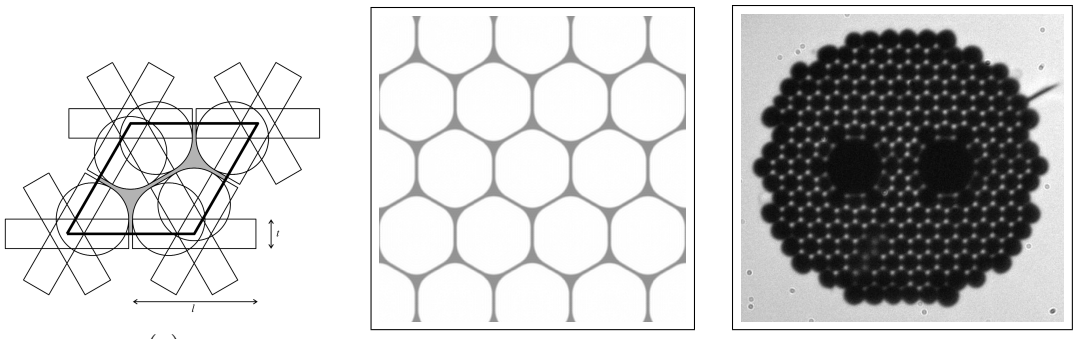

(a) (b) (c)

Figure 2-5: (a) Cartoon of the process for defining the parameters of a PCF cladding unit cell [53]. (b) The output from defining the cladding as per figure (a) based on fabricated device sizes and transmission spectra (Fig. 2-6). (c) Optical micrograph of a dual core fibre fabricated during this work. The image shows the excellent similarities between the two adjacent cores.

To obtain the properties of the fibre fabricated by Brian Mangan, (fig. 2-5c), optical micrographs like the one showed were used to calculate the physical dimensions of the cladding structure; pitch (Λ), strut thickness and corner roundness. The resultant dimensions gave an idealised cladding hole for that fabricated fibre.

The physical measurements, as calculated above were used to generate parameters for the unit cell file input into the FFPW code. These parameters, defined in (fig. 2-5a), were $l = 0.8575\Lambda$ and $t = 0.21\Lambda$ in dimensionless units, where Λ is the hole to hole spacing of the cladding, or *pitch*. For the fabricated fibre the pitch was 2.1 μm.

The output from running the code is the density of states (DOS) plot (fig. 2-6b). On the plot, the red regions denote that the code could not find a mode of the cladding at that frequency. Where the DOS plot is black, there are one or multiple states existing in for that wavelength and wavevector. The blue line across the centre of the plot shows the air-line ($\beta = nk_0$), the effective index of a free space mode. Core modes of a fibre have most of their properties defined by the large air core which they inhabit and as such will sit close to this line.

In order to ensure that the modelled fibre was a suitable approximation to the fabricated fibre white light transmission measurements were taken. These measurements were taken with both a black-body radiator and a fibre-generated

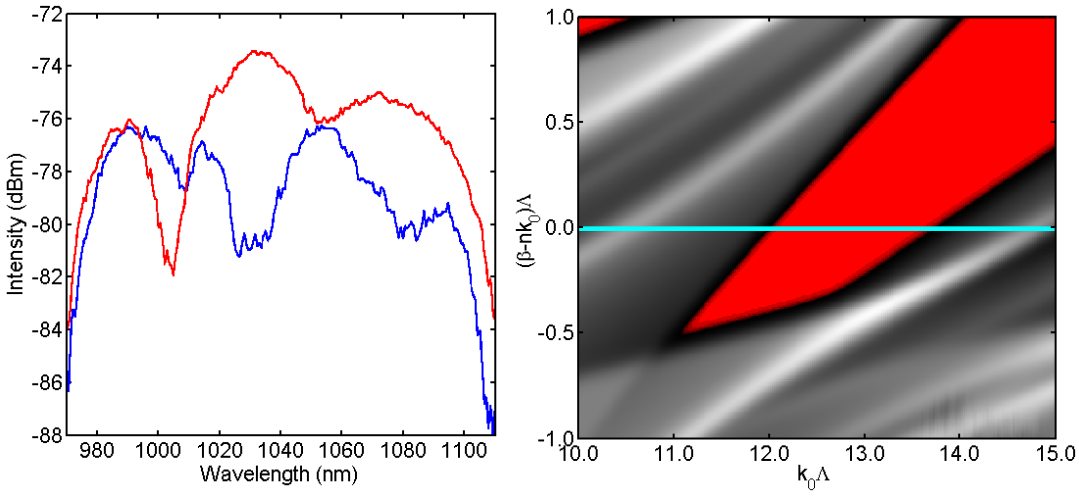

(a) (b)

Figure 2-6: (a) Optical output from each of the cores when the fibre illumination was into a single core only. (b) Plot of the photonic density of states (DOS) for normalised wavevector and normalised frequency. The red regions show where no modes exist within the cladding structure defined (fig. 2-5b). The blue line denotes the refractive index of air.

supercontinuum. The output of each core was measured with light input into a single core (fig. 2-6a). The experimental transmission window was used to validate the cladding parameter selection by matching it against the spectral width of the bandgap in the DOS plot produced by the FFPW code. The width of the bandgap is 130 nm, centred at 1035 nm as measured along the light line of the DOS plot (calculated using a pitch of 2.1μm); compared to 130 nm width, centred at 1032.5 nm in the experimental measurement. Therefore the numerical model has good correlation to the real fibre.

2.6.3 Full-vectorial Finite Element Method

FEM Introduction

Many of the equations of physics, including those describing the propagation of light in a waveguide, are partial differential equations (PDEs). Some PDEs have higher order terms, or are applied to complex geometries. In these cases, they do not have analytical solutions. When a numerical solution is required, two

methods are generally used: Finite difference methods (FDM) or finite-element methods (FEM). Finite element methods have a more global approach, based on the calculus of variations [55]. One advantage of their use here is their inherent capability to incorporate mixed boundary conditions and random element sizes, unlike FDM which requires discretisation on a regular grid.

The basic steps that make up FEM are as follows:

- Rephrase your equations into their weak formulation, This step changes our problem from solving a PDE to minimising a *functional*. For most FEM, the functional is in the form of an integral.
- Discretise your infinite linear problem into a finite discrete one. To complete this, it is necessary to put a mesh over your model space; which is most commonly triangular. The vertices of the applied mesh become your solution points, and you interpolate between them either linearly or using low order polynomials.
- Apply appropriate boundary conditions.
- Solve.

Whilst this seems to over simplify FEM, a fuller, and more verbose, explanation can be found in some standard texts [56–58]. One main point to discuss is the last one. FEM analysis is usually done by a commercial package designed to solve your particular PDE. For the case of the wave equation, in any of its forms, the package used for this analysis was Comsol Multiphysics®.

Comsol Multiphysics RF Module

Within this thesis I utilise Comsol Multiphysics with the attached RF module as a standard FEM package. I implement the geometry with the perpendicular waves application mode. In this mode, the waves propagate out of the plane of the 2-dimensional geometry analysed. In general, this deals with waves of the form $\mathbf{E}(x, y, z, t) = \mathbf{E}(x, y) \exp(i(\omega t - \beta z))$ as discussed previously. These fields are applied to various formulations of the relations [59]:

$$\nabla \times \mathbf{H} = i\omega\epsilon\mathbf{E} \tag{2.16}$$

$$\nabla \times \mathbf{E} = i\omega\mu\mathbf{H}. \tag{2.17}$$

These can be solved in either of two methods; calculating $\lambda = -\delta_z - i\beta$ as the eigenvalue, or using the eigenvalue $\lambda = -\delta - i\omega$ to calculate the angular frequency ω. If we consider TE waves only we can remove the z-component of the electric field and derive a PDE for the H_z component of the magnetic field.

By combining the relative Maxwell-Ampere and Faraday laws, given the above stipulations, we obtain:

$$-\nabla \cdot \left(n^{-2}\nabla H_z\right) - \mu_r k_0^2 H_z = -\beta^2 n^{-2} H_z \tag{2.18}$$

where I have substituted the refractive index, n, for the dielectric constant, ϵ using the relationship $n = \sqrt{\epsilon\mu}$ [59, 60]. However, if we also require to consider hybrid waves, where either the modes are not completely TE or TM, but are only quasi-transverse modes, or where we have inhomogeneous materials, then the formulation is more complex. In this case, either two equations for the transverse field components are solved, or three equations for each field component is solved.

2.6.4 FEM Model of a dual-core HC-PCF

Generating the geometry of the dual-core HC-PCF consists of three parts:

- create a bulk cladding structure consistent with the unit cell from the FFPW calculations and insert an idealised bulk cladding into your model space;
- take boundary conditions and symmetry into account to simplify the problem and generate an associated model space.
- insert dodecagonal cores regions, modifying the surface cladding rings, the nearest ring of bulk cladding holes to the core boundary,to match the experimental fibre;

These are each discussed in turn below.

Bulk Cladding

In order to do create a bulk cladding, a triangular lattice of cladding hole sites was generated by converting the lattice coordinates $\hat{a}$ and $\hat{b}$ into Cartesian lattice vectors:

$$\hat{a} = 0.5\Lambda\hat{x} + 0.5 * 3^2\Lambda\hat{y} \tag{2.19}$$

$$\hat{b} = 0.5\Lambda\hat{x} - 0.5 * \sqrt{3}\Lambda\hat{y} \tag{2.20}$$

such that the lattice pitch, Λ, was equivalent to the fabricated fibre (2.1 μm). These lattice vectors can describe an infinite set of possible coordinates for the cladding holes. To define the sub-set that make our fibre cladding we generated a set of 7 cladding rings about the centre point 0,0. Once complete, a further third of a complete ring was added (Fig. 2-7a), to elongate the cladding in the horizontal direction and make it equivalent to the cladding of the real fibre.

These coordinates were then moved horizontally by a half-pitch. This is to retain the symmetry of a dual-core as defined by the fabricated fibre. The axes of symmetry for the real fibre goes through a vertical cladding "strut" in its centre (Fig. 2-5c). These struts are generated at the cladding hole boundary and as such are equidistant between two horizontally adjacent cladding holes.

At each lattice site, a regular hexagon was formed by coercing a set of six lines, whose end points were formed using the simple formula:

$$xy = \frac{1}{\sqrt{3}} \exp 2i\pi(n + 1/2) \tag{2.21}$$

where n is a set of 7 linearly spaced numbers from 0 to 6. The real and imaginary part of this equation yields the set of Cartesian coordinates to generate the vertices of a hexagon, oriented so that it pointed vertically, about its centre. The hexagon was scaled using both the pitch, Λ, and the relative hole width with respect to the pitch, the l parameter from the FFPW code. Finally, to match the

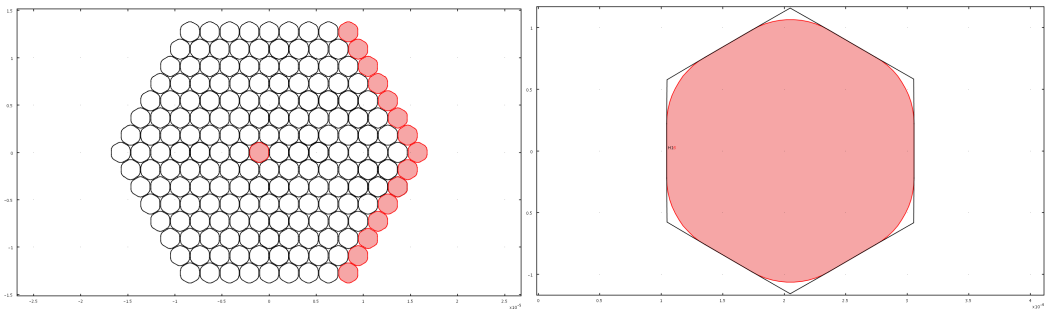

Figure 2-7: (a) Image of the bulk cladding during generation of the model space. The ringed structure is clear to see, with the extra cladding holes highlighted. (b) A blown up cartoon of a modelled cladding hole showing the vertically aligned hexagonal shape with the filleted corners.

hole shape from the FFPW code, the corners of the hexagons were rounded using the *fillet* command. This rounded them using a user-defined radius of curvature, derived from the previously calculated t and l parameters (Fig. 2-7b). These bulk cladding hexagons were placed at each lattice point defined previously.

Symmetry and the Model Space

Coupled Mode Theory (CMT) tell us that identical cores are required for complete power transfer to occur during mode propagation. Whilst the greatest effort was made to obtain this experimentally, the final fibre has what can be described as nominally identical cores; in that both their physical dimensions and the physical dimension of the surface cladding holes are similar, if not identical. In the real fibre, although the cores appear similar during image analysis, there appears to be a difference in the transmission measured out of each core. It is observed that when measuring the output from each core for a fixed input there is a wavelength shift between the regions of higher loss (Fig. 2-6a). A sensible origin of this difference would be the differing interaction between the core mode and the surface and cladding modes surrounding each of the cores.

In the modelled space, we can match the cores completely, in terms of their physical dimensions. In reality, however, during the meshing phase of the simulation, the mesh elements are not exactly the same. As is explained later, the quality of the mesh can affect the solution parameters, making identical cores,

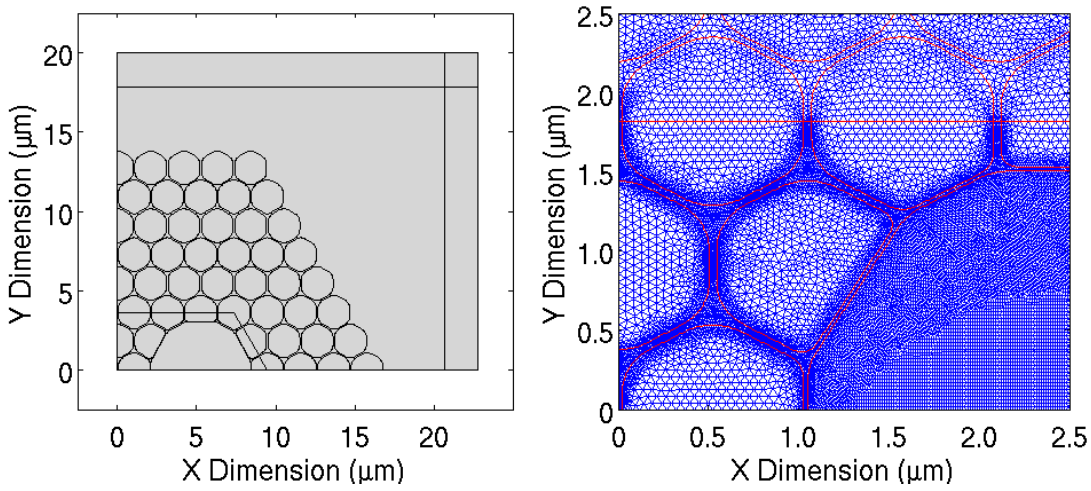

Figure 2-8: Plots showing (a) the quarter structure used for the Comsol model. The PML layers and trapezium used to bound the high density mesh region. (b) A plot showing the extra mesh refinement in the core and coupling regions.

into nominally similar cores; and no decoupling will be observable.

The solution to this problem is to only use a single core in the model space; utilising the symmetry of the model space to determine the complete solution. This method provides the capability to generate identical cores but also minimises the required number of elements that make up the model space.

The total model space was now able to be defined, by using the origin $(0, 0)$ and the Cartesian x- and y- axes as two of the boundaries. The other two boundaries were chosen such that a rectangular model space was defined that was approximately 1.5 times larger than the maximum dimension of the cladding structure. Along the "outer" boundaries, we used perfectly matched layers (PML) to minimise any effect of the presence of the boundary on the model structure. The dimension of these perfectly matched layers was chosen arbitrarily as the pitch of the fibre. This is completely unoptimised, and some simulations were done whereby this thickness was changed. No observable change in the results was detected, so the thickness was left in its unoptimised state.

A PML is a domain that acts as an artificial absorbing layer for wave equations with no reflections back to the domain which the wave is incident to the PML from. The original formulation for PMLs involved splitting electromagnetic fields into two non-physical fields in the PML region [61]. The usual approach taken

now is that of a *stretched-coordinate PML* [62,63], which is a generalisation of the problem and encompasses the earlier approach. In this case, the PML corresponds to a coordinate transformation mapping coordinates to complex numbers, effectively changing a propagating wave into an exponentially decaying wave. Comsol Multiphysics implements this by using the transformation

$$t' = t\frac{\lambda}{\delta t}(1-i) \tag{2.22}$$

where t is the coordinate being transformed [60].

Boundary Conditions

Initially, to understand the boundary conditions, let us think about the fundamental modes supported by each core and what the supermodes of the dual-core structure may look like. We shall consider only the transverse electric (TE) polarisation here, whereby the main field components are the E_x and H_y field components. The analysis steps also hold for the TM mode, but this will not be shown here.

Considering the fundamental TE mode of each core only (TE_{01} modes) we can immediately understand that the horizontal boundary, defined by the x-axis of our model space cuts the cores directly in half. For a fundamental TE mode, we need a continuous value of the E_x field across this boundary. The electric field component perpendicular to the boundary, E_y, is zero at the boundary in this case. We can use the *perfect electric conductor* boundary condition to enforce this symmetry; such that $\hat{n} \times \vec{E} = 0$, where n is the vector normal to the boundary. This boundary condition now yields a symmetry condition that means we can reduce our model to the upper half-plane and consider only TE modes.

To further exploit the symmetry of the problem we now consider the vertical boundary, as imposed by the Cartesian y-axis. We know that coupled waveguides support the same number of supermodes as cores. In this case we have two supermodes, a symmetric and anti-symmetric mode. In the antisymmetric TE mode, the E_x field component will be zero at the boundary that bisects the two cores This can be enforced by using a *prefect electric conductor* condition. For the symmetric mode, the E_x component is continuous and it is the H_x component,

Table 2.1: Table giving the supported modes in the core region for the different combinations of boundary conditions that bisect the centre of the fibre cladding. Each combination only supports a single mode of the dual core structure.

Horizontal Boundary	**Vertical Boundary**	**Supported Mode**
$\hat{n} \times \vec{E} = 0$	$\hat{n} \times \vec{E} = 0$	Anti-symmetric TE modes
$\hat{n} \times \vec{E} = 0$	$\hat{n} \times \vec{H} = 0$	Symmetric TE modes
$\hat{n} \times \vec{H} = 0$	$\hat{n} \times \vec{E} = 0$	Symmetric TM modes
$\hat{n} \times \vec{H} = 0$	$\hat{n} \times \vec{H} = 0$	Anti-symmetric TM modes

and similarly the E_y component, that is held at zero for this mode. In this case we can use the *perfect magnetic conductor* boundary condition; such that $\hat{n} \times \vec{H} = 0$; to achieve this.

By limiting the field components at the boundary we can generate the symmetry observed in our large structure by only using the small quarter structure defined in figure 2-8. However, the model space now only supports a single mode for each boundary condition setting. The full structure modes, and their associated boundary conditions when modelling the quarter-structure are given in Table 2.1. By using the symmetry to make the two cores effectively identical, there is a separate problem. Rather than have separate mesh formulations for each core, we have one for each different boundary condition setting as these need to be set prior to determining the mesh. However, if the mesh is not generated automatically but the parameters of the mesh are set as constant the user has more control over the density and position of the mesh elements.

Air Cores and Surface Cladding Rings

To generate core regions when fabricating fibre; either 1,7 or 19 bulk cladding capillaries (in a one, two or three ringed hexagonal arrangement) are removed. For the model, the same approach was taken, in which five cladding holes are removed in a semi-hexagonal arrangement (a trapezium). The centre of the core wad located at the fourth cladding hole from the centre of the cladding structure to match the geometry of the fabricated fibre.

The resultant shape is not similar to the core as seen in the fabricated fibre (figure 2-5c). The differential pressure applied to the core deforms the first ring

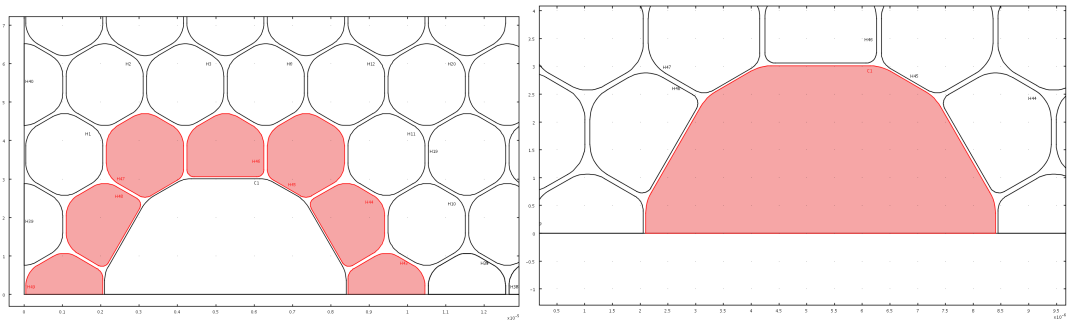

Figure 2-9: (a) Diagram of the bulk cladding near the core region. The surface ring of holes that surround the core are highlighted. Every other cladding hole has been turned into a irregular pentagon, and the curvature of the corners that edge the core has been changed. (b) Diagram of the core region with the core hole inserted. The irregular semi-dodecagon structure is easily observed.

of cladding holes by using surface tension to form an almost circular core region. The core is not actually circular, but due to the geometry constraints is a rounded dodecagon.

The surface ring of cladding holes was modified by making every second regular hexagon into an irregular pentagon (figure 2-9a). The core was then added by inserting a dodecagon into the space provided. The relative width of the dodecagon was calculated by ensuring the core wall was half as thick as the cladding struts in the bulk cladding (figure 2-9b) in order to minimise the interaction between core and surface modes.

The corners of both the dodecagonal core and the corners of the surface ring pentagons and hexagons that were adjacent to the core were modified so that their radius of curvature was scaled relative to the bulk cladding radius of curvature. The rate of scaling was controlled by the difference in curvature between the core and bulk radius of curvature in the real fibre.

Meshing

The mesh is one of the fundamental components of FEM modelling. As discussed in the earlier section on FEM, it provides small elements for approximating a PDE solution. The most common shape for elements in an FEM analysis are triangles as this allows closer approximation to the real shape within your modelling space,

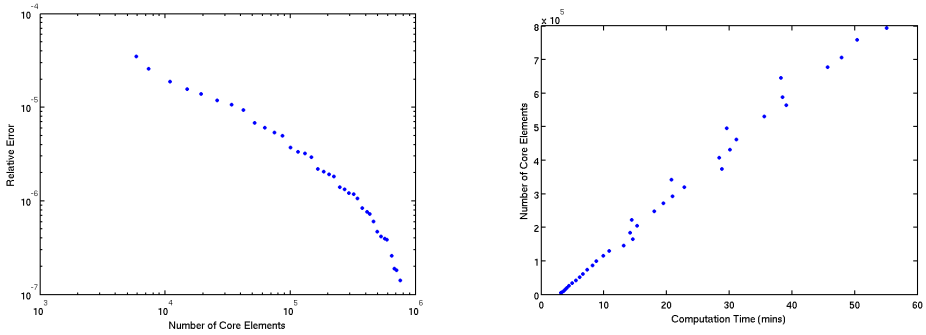

Figure 2-10: (a) Convergence plot of relative error against the number of core elements. Also shown is the relationship to computation time for obtaining the modes for a single wavelength (b).

Table 2.2: Table of mesh parameters for dual-core PCF modelling in Comsol Multiphysics

Parameter	**Value**
Maximum Element Size	$\Lambda/10$
Core Maximum Element Size	$\Lambda/40$
Element Growth Rate	1.4
Mesh Curvature Factor	0.15
Narrow Region Resolution	2

in this case the curvature of the air holes of a PCF, although this is not exclusively used.

Choice of suitable mesh parameters is important in any modelling situation and in all the work done here, convergence testing was performed to optimise the mesh parameters, given a reasonable computation time and the computing constraints available. One such convergence plot can be seen in figure 2-10. Here, I have used the result from the most dense mesh as the "true" value and computed the difference between one iteration and the next by changing one of the mesh parameters.

Comsol Multiphysics® keeps mesh generation simple. It allows control of five main parameters: the maximum element size, or maximum element size scaling factor; element growth rate; mesh curvature factor and cut-off, and resolution parameter for narrow regions. The latter parameter is particularly important in

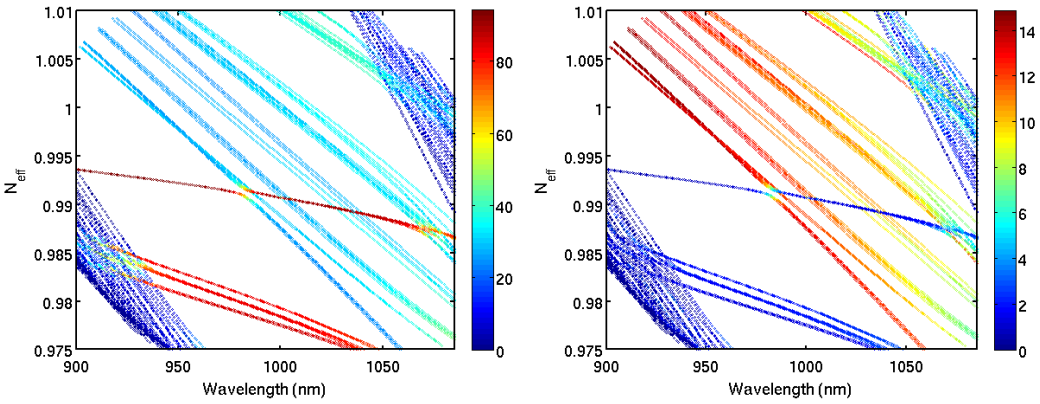

Figure 2-11: Plot of effective index against wavelength. The colours of the plots show the power present in the air core (a) and the power present in the glassy region surrounding the core and bounded by the trapezium of 2-8 (b).

this work as it determines the number of layers of elements created in narrow regions, for example the struts of a PCF. The mesh parameters for this work are given in table 2.2. For further information, see the Comsol User Guide [59].

Obviously, a simple way to make the computational time less but keep the level of accuracy required is to adapt your mesh more closely to the geometry in question. For this work, a simple trapezium was added to the geometry to act as a boundary between the bulk cladding and the core region. Whilst the full structure is important to the model, the area where the light is confined requires more attention. and as such the maximum element size in this region was a quarter of the value in the bulk device. Again this value was chosen to maximise the accuracy without having inordinately long computation time.

2.7 Analysis

The FEM analysis shows that within the simulation space of the modelled fibre, there exist both TE and TM modes, with both symmetric and antisymmetric modes. It can also be seen that despite the authors best efforts to control the surface modes [44], there still exist surface modes within this fibre that affect these modes. The power present in the surface modes is significantly lower than that present in the air region of a bound mode, but it is non-trivial (Fig. 2-11).

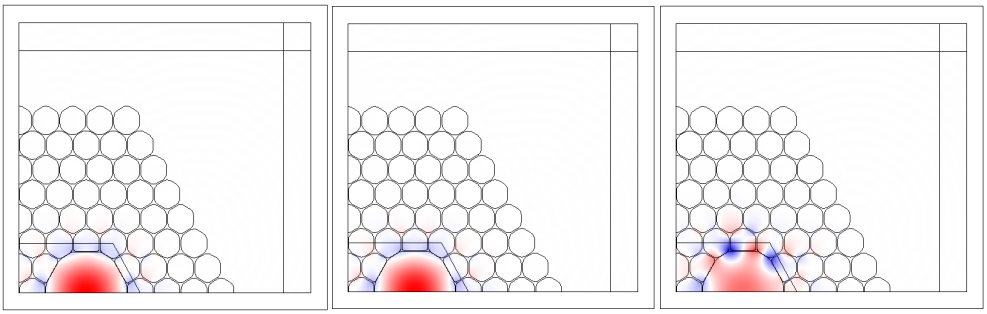

Figure 2-12: Field plots for the antisymmetric TE mode away from the decoupling point, at 931 nm (a), at the decoupling point, at 968 nm (b) and during an anti-crossing at 986 nm.

As can be seen when looking at the field profile of the antisymmetric TE mode, the mode shape is severely distorted when the core and surface modes interact (2-12 (c)). The presence of these surface modes does however, not deter from the qualitative nature of the results as they are sufficiently away from the peak of the decoupling point. Following the analysis of academic publications on this subject [51, 52], it may seem that the surface mode coupling is essential in the explanation of the presence of the decoupling point and so potentially they are a necessary component of decoupling adjacent cores.

A point of note for the surface mode is that it is not circularly symmetric. There appears to be a negative lobe missing from the core-cladding interface. Whilst it could denote a higher order of rotational symmetry, it might also be an artefact of the model space or more importantly a pointer to the modal decoupling. Potentially this interaction could signal that the decoupling mechanism is similar to that already observed for the all-solid fibre.

Continuing along this thought process, it would appear that the field profiles themselves (fig. 2-12) might show some difference between the decoupled cores and the cores far away from this point. This is clearly not the case, as both fields appear similar on initial inspection, and this has been confirmed through numerical comparison. This is however the first time that this work has been completed on a fibre with such a large difference in the refractive index of the low and high index materials. Previous work on all solid fibre yields a much less confined field profile for the core mode, with more interaction in the first ring of

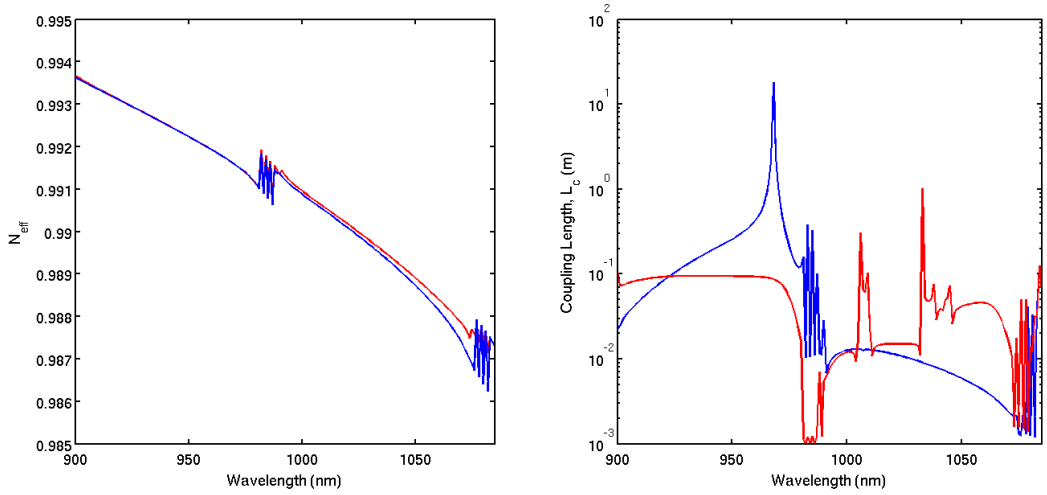

Figure 2-13: (a) A plot of the two TE core modes of the dual-core HC-PCF (b) Plot of the coupling length as a function of wavelength for the transverse electric (blue) and transverse magnetic (red) modes. Clearly a single peak, marking the decoupling point, can be seen with a maximum value of approximately 10^2. This is two orders of magnitude greater than any of the other features of the curves, which can all be directly attributable to anti-crossings with surface modes.

cladding holes than has been observed here. This might explain the difficulty in observing the role of the periodic lattice in the decoupling process.

If we extract the data for the fundamental core modes and calculate the resulting coupling length (fig. 2-13), we see that the hollow-core PCF creates a significant decoupling point with two orders of magnitude difference between the coupling length at the decoupling point and along the rest of the fibre. This high peak stands alone as the only feature that cannot be directly related to an anti-crossing interaction between the core modes and cladding modes. The lack of intensity inside the cladding at this wavelength shows that the overlap with these surface modes has not yet become significant, as can be seen by comparing the field plots. We can compare the decoupling peak from this work directly with those present in the published literature (fig. 2-4). In our case, we have a much narrower peak (if we make assumptions about the FWHM of the previous work). Again this is hardly surprising from a qualitative point of view as the strength of the interaction between the surface and cladding modes has been shown to be

much weaker due to the higher confinement of the core modes and lower density of surface modes across the transmission window.

2.8 Discussion

2.8.1 Future Work

In this section we have seen that a qualitative assessment of the decoupling of dual-core HC-PCF has been analysed. This shows very little difference to the understanding gained from published literature, except in the fact that we do not yet understand the full ramifications of introducing a higher differential between the refractive index of the cladding holes and the cladding struts. Some simple hypotheses have been given above, based on the presented findings but more work needs to be completed to fully understand this.

It would also be the authors wish that further experimental evidence was gained to corroborate the above results with HC-PCF. Whilst some initial experimentation was completed during the authors time at Bath, mainly by Dr. Brian Mangan, there was not enough mature evidence to present here.

2.8.2 Comparison to Silicon-on-Insulator Waveguide coupling

This work has been included within this thesis to show the importance of understanding dispersion and coupling across a diverse collection of areas of study, namely optical communications and photonics. Size scales in these two disciplines are an order of magnitude apart and as such we move away from the strongly guided and weakly coupled modes of HC-PCF to the strongly coupled waveguide arrays that are the object of study in the silicon photonics. The physics behind each one involves a different set of assumptions, for example: is the tight binding approximation valid in both cases? Recent literature has shown that in the case of silicon, the tight binding approximation has indeed been validated [16], suggesting more similarity between the different waveguide regimes where coupling is concerned.

Importantly, apart from the differences in analysis is the difference in applica-

tion. Optical fibres are a mature technology and one that has a well defined use within industry in the transmission of signals and power. The new possibilities yielded by PCF have meant that optical fibre faces new uses as a non-passive component in many systems. From a transmission sense, understanding core-to-core interaction would be of importance if you could operate at a point where you could permanently decouple the cores. However, if we consider active components, being able to couple and decouple the cores with different wavelengths may lead to some interesting active components involving wavelength selection transmission and generation. This is in contrast to the role of coupling in the silicon photonics sections of this thesis. Here we are only focused on facilitating further exploration of non-linear phenomena as we shall see in the following chapters.

2.9 Summary

In this chapter we have shown that dual-core hollow core fibre can support a decoupling of the core modes of adjacent cores. This extends the published literature, where only all-solid fibre has been considered. A decoupling point, with a numerical increase of two orders of magnitude of the coupling length has been found numerically, in a fibre generated from the parameters of a real dual core fibre (fabricated at Bath by Dr. Brian Mangan). Future work has been suggested that would help further explore this phenomenon and any interesting attributes that come from the host material. A comparison between the results obtained here and the results of the rest of this thesis has also been discussed, in terms of their physics and of their technological significance.

Chapter 3

Silicon Photonic Wires in the Linear Regime

3.1 Introduction

The remainder of this thesis is a description of an experimental and numerical investigation into the behaviour of coupled silicon photonic wires on the nanometre scale. This behaviour includes both linear characteristics, the subject of this chapter, and non-linear characteristics, the subject of subsequent chapters. Although the linear characteristics are important in their own right for propagation under low intensity fields, the characterisation of this behaviour is paramount to understand the non-linear effects observed under propagation of high intensity fields. The linear measurements also serve to verify the expected physical and optical properties of the samples used throughout the work.

This chapter consists of a discussion of the theory of the different types of dispersion observed in arrays of silicon photonic wires: material dispersion, waveguide dispersion and coupling induced dispersion. To understand this last point coupled oscillators will be discussed and equations governing linear propagation in coupled waveguides mentioned.

I then briefly describe the fabrication of real devices. Although this is not the author's own work, it is included here for completeness. I will review the academic literature on linear propagation in photonic wires, and show where this work fits within the research landscape.

Finally I will describe my own work and the numerical and experimental results obtained, which are also published in the academic literature [64–66].

3.2 Chromatic Dispersion

We have covered the basics of chromatic dispersion, or more accurately the basics of GVD, in the opening chapters of this thesis. In that explanation we concerned ourselves with the changes to the description of the light itself with no consideration of the origin of these effects. Below, we consider these origins, both material and geometric, in more detail; with particular reference to a geometry consisting of arrays of rectangular silicon waveguides.

3.2.1 Material Dispersion

Material dispersion is the component of chromatic dispersion resulting from the spectral variation in the optical properties of the guiding material. This has been studied extensively and in general, there are three main approaches when modelling refractive index as discussed below.

The Sellmeier Equation

In Chapter 1, we saw the relationship of the displacement field $\vec{D}$ to the electric field $\vec{E}$ via the polarisation $\vec{P}$ such that:

$$\vec{D} = \epsilon_0 \vec{E} + \vec{P} \tag{3.1}$$

The polarisation can be thought of as a sum of harmonic oscillators, which will cause absorption at resonance [3]. The equation of motion of the n^{th} oscillator is given by

$$\omega_n^2 \vec{P_n} + \frac{\partial^2 \vec{P_n}}{\partial t^2} = \epsilon_0 \Delta\epsilon_n \omega_n^2 \vec{E} \tag{3.2}$$

where ω_n is the resonant frequency of the oscillator, and $\Delta\epsilon_n$ is the coupling between the electric field and the oscillator. Summing over these polarisations gives a displacement field of the form:

$$\vec{D} = \epsilon_0\epsilon_\infty\vec{E} + \sum_n \vec{P_n} + \epsilon_0\chi_0^{(3)} \tag{3.3}$$

where the quasi-instantaneous term, ϵ_∞, has been added. It has a value, in silicon, of 11.6858 and results from the summation of high-energy direct-gap transitions [67, 68]. In response to an electric field, the oscillators reach a steady state. If we assume an equation of Lorentzian form to describe the frequency dependence, the frequency dependence of the dielectric permittivity is found to be

$$\epsilon(\omega) = \epsilon_\infty + \sum_n \frac{\Delta\epsilon_n\omega_n^2}{\omega_n^2 - \omega^2} \tag{3.4}$$

which can be rearranged in terms of free space wavelength and refractive index to give the usual form of a group of equations known as Sellmeier equations:

$$n(\omega) = \sqrt{\epsilon_\infty + \sum_n \frac{\Delta\epsilon_n\lambda^2}{\lambda^2 - \lambda_n^2}} \tag{3.5}$$

These fitting of these equations to the experimental refractive index for silicon and silica has been extensively studied, and is well documented [67, 69](with fitting parameters defined in Table 3.1). The oscillators described do not relate to physical oscillators but are merely curve-fitting parameters. For silicon and silica the only difference is the number of oscillator terms generally used. However, in the case of silicon, the Sellmeier equation is more usually modified to improve the fitting with experimental data [67]:

Table 3.1: Sellmeier equation coefficients for silicon and silica used throughout this work. For silica, the conventional Sellmeier equation has been used (3.5) and for silicon, the modified equation (3.6).

	Silicon	**Silica**
ϵ_∞	11.6858	1
$\Delta\epsilon_1$	0.00810461	0.6961663
$\Delta\epsilon_2$	0.939816	0.4079426
$\Delta\epsilon_3$	-	0.8974794
λ_1 (μm)	1.1071	0.0684043
λ_2 (μm)	1	0.1162414
λ_3 (μm)	-	9.896161

$$n_{Si}(\omega) = \sqrt{\epsilon_\infty + \frac{\Delta\epsilon_1\lambda^2}{\lambda_1^2 - \lambda^2} + \frac{\Delta\epsilon_2\lambda^2}{\lambda_2^2}} \tag{3.6}$$

The Herzberger Equation

Like the Sellmeier equation above, the Herzberger equation [70, 71] was initially developed to study the optical properties of glasses. However, again like the Sellmeier equation it has been shown to adequately model the dielectric constant of many crystalline materials and is used to approximate the dielectric constant of silicon in many applications.

$$n = A + B\lambda + \frac{C}{(\lambda^2 - \lambda_0^2)} + \frac{D}{(\lambda^2 - \lambda_0^2)^2} \tag{3.7}$$

The origin of this equation comes from two likely sources: the Helmoltz-Kettler-Drude formula [3, 72], a derivation of the Sellmeier equation discussed previously, and the Schott dispersion formula [73]. The theory assumes that glasses have two absorption bands, one in the near ultra-violet and the other in the far infra-red. This red absorption is far enough away from the spectrum of interest to be approximated by its linear form. This is similar to the justification

for using the Laurent series expansion of the Sellmeier equation [72].

The Model Dielectric Function (MDF)

The most complete way to study the optical properties of a material is to use the atomic band-structure to determine the important transitions that contribute to the dielectric function, $\epsilon(\omega) = \epsilon_1(\omega) + i\epsilon_2(\omega)$. For silicon, the most widely accepted model of this type is the MDF set out by Adachi [68]. In his formalism, the conduction to valence band transitions are linked via their momentum matrix to $\epsilon_2(\omega)$ such that

$$\epsilon_2(\omega) = \frac{4\hbar^2 e^2}{\pi m^2 \omega^2} |< c|p|v >|^2 J_{ev}(\omega) \tag{3.8}$$

where $J_{ev}(\omega)$ is the joint-density-of-states function and $< |p| >$ is the momentum matrix element of the valence to conduction band transitions. This contains all of the relevant transitions across the silicon band-structure (E_0, E_1, $E_{1'}$, E_2 and E_g^{1D}), as outlined in figure 3-1a.

The contribution to the refractive index comes in four forms. Firstly, the one-, two- and three-dimensional critical points are included using the following equations:

$$\epsilon_{1D} = -B_1 \left(\frac{E + i\Gamma}{E_1}\right)^{-2} \ln\left(1 - \left(\frac{E + i\Gamma}{E_1}\right)^2\right) \tag{3.9}$$

$$\epsilon_{2D} = -F \left(\frac{E + i\Gamma}{E_2}\right)^{-2} \ln\left(\frac{\left(1 - \frac{E+i\Gamma}{E_1}\right)^2}{\left(\frac{E+i\Gamma}{E_2}\right)^2}\right) \tag{3.10}$$

$$\epsilon_{3D} = \sum_n^{\infty} \frac{B_{1x}}{(2n-1)^3} \frac{1}{E_1^2 - E^2 - i2E\Gamma} \tag{3.11}$$

where B_1, B_{1x} and F are all fitting parameters, and Γ is the oscillator strength. It appears that different iterations of the MDF use either the same strength or different strengths for each transition.

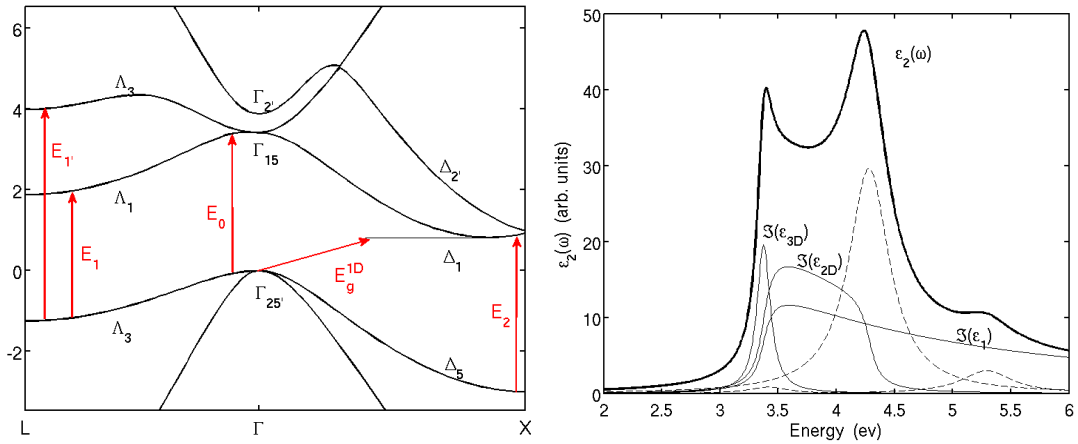

(a) (b)

Figure 3-1: (a) Numerically modelled silicon band-structure along two symmetry directions. The location of the transitions responsible for the refractive index are included in red. This diagram was calculated using the pseudo-potential method [76, 77]. (b) Imaginary part of the dielectric constant and the relevant contribution from each of the terms used. This model and its parameters have been fitted to the experimental data from [78]. The solid lines correspond to the ϵ_1, ϵ_{2D} and ϵ_{3D} components, and the dashed lines three damped harmonic oscillators, about E_0, $E_{1'}$ and E_2.

Finally, the E_2. $E_{1'}$ and E_0 transitions are of the form of a damped harmonic oscillator (DHO). In the case of the E_2 transition, the physics is more complicated. The DHO employed in this model [74] is representative of a broadened two-dimensional M_1 critical point that has been used to characterise this transition [75]:

$$\epsilon_{DHO} = \frac{CE_2^2}{E_2^2 - E^2 - iE_2E\gamma_{E_2}} \tag{3.12}$$

where γ_{E_2} is the damping term, and C the oscillator strength. The $E_{1'}$ and $E_{0'}$ transitions are usually omitted from analysis of dielectric constant due to their relative weakness but are included in this model in a DHO form for simplicity.

.

The above terms are all complex and so contribute to the real and imaginary parts of the dielectric constant. The contribution can be seen directly, in the case of silicon, in figure 3-1b. For our analysis, it is then trivial to convert this to refractive index via the relationship $n + ik = \sqrt{\epsilon_1 + i\epsilon_2}$.

Experimental Data and model fitting

The refractive index of silicon is an important quantity for many areas of physics, due to the versatility of the material itself and its wide application to areas as diverse as optics, microelectronics, solid-state and quantum physics. To this end, the experimental determination of this constant has received much attention historically [78–84] and has been measured over a wide range of wavelengths (see Fig. 3-2 (left)). The measurement technique mainly used for this type of experiment is spectral ellipsometry. This technique uses reflected light in both s- and p- polarisation, across the full spectrum of wavelengths. The light is incident on a layered sample consisting of homogeneous layers with perfectly abrupt interfaces. Model parameters are fitted to the data across the entire range of measurements using standard curve-fitting algorithms.

To test the accuracy of each of the model considered in the previous section, the most complete measurement set across the spectral region of interest [78, 85] was used as the experimental test data. The models were then fitted using a least-square fitting algorithm (see Fig. 3-2 (right)) over a large spectral range. The fitting of the MDF was slightly more complicated as the real and imaginary parts needed to be fitted simultaneously so as to produce physically meaningful parameters. Immediately, from the fitting, a large resonance peak can be observed in the Sellmeier equation. This is present due to the fitting region extending into the infrared and visible spectra. In the later chapters we shall see the importance of this as we consider the non-linear behaviour of light in silicon waveguides. For example, in studying modulation instability (MI) the values of dispersion, especially second-order dispersion, far away from the pump is paramount to understanding experimentally observed behaviour.

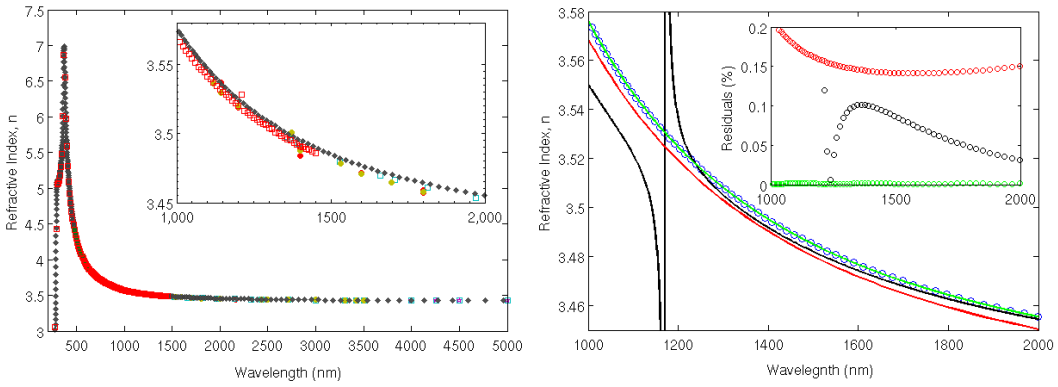

Figure 3-2: (left) Experimental measurements of refractive index of silicon from literature [67,78–84]. It can clearly be seen that this quantity has been determined over a large range of values. For the optical measurements discussed within this thesis, only a small range of values are relevant. This region has been magnified in the inset graph. (right) Fitting of Sellmeier (black), Herzberger (green) and Adachi's MDF (red) to experimental data from [78]. Inset is a plot of the residual difference between the relevant fit and the experimental data.

3.2.2 Waveguide Dispersion

Waveguide dispersion describes the chromatic dispersion effects that field confinement have on a wave as it propagates through a waveguide compared to those experienced in propagation through a homogeneous medium [7]. Inherent in the parameters that describe a propagating mode, such as the propagation constant β, is wavelength dependence even in the absence of material dispersion. This can be seen by considering the spread in the mean transit time, δt, when material dispersion has been ignored [1]:

$$\delta t_j = z \frac{d^2\beta}{d\omega^2} \delta\omega. \tag{3.13}$$

Another way to think about this is to consider a step-index fibre where two modes are travelling [86]. The first has a large wavelength relative to the core and the second has a small wavelength relative to the core. In the first case, the mode is very loosely confined and the majority of power is carried within the cladding material. The propagation constant and group delay approach that

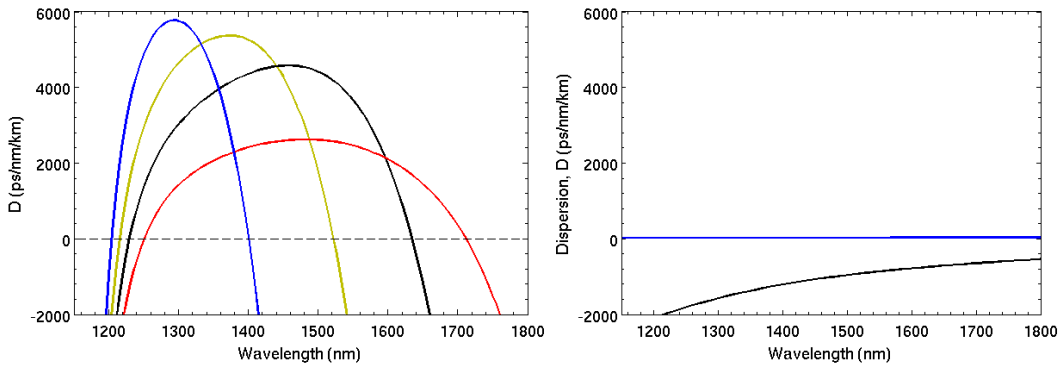

Figure 3-3: (left) Plot of the dispersion curves of four different waveguide cross-sections: 340 nm x 220 nm(blue), 360 nm x 220 nm (gold), 380 nm x 220 nm (black) and 420 nm x 220 nm (red). Positive values correspond to the anomalous GVD region. For comparison, a graph of the dispersion in bulk silicon (black) and bulk silica (blue), i.e. without waveguide dispersion, is also shown (right).

of a plane wave propagating in the cladding. In the second case, the mode is very tightly confined and the power is predominantly carried by the core. The propagation constant approaches that of a plane wave propagating in the core material. Inbetween these cases, the confines of the waveguide control the modal profile and the relative propagation constants of each wavelength within a mode.

As can be seen from figure 3-3, the presence of waveguide dispersion can make the total dispersion anomalous, where material dispersion alone is normal. By studying the two figures, and comparing to the earlier discussion on material dispersion, it can be seen that making the total dispersion anomalous over a given spectral window generates two zero-dispersion wavelengths. The long wavelength zero-dispersion point appears to be heavily dependent on the geometry of the waveguide. The variation of the short wavelength zero-dispersion point, however, shows less variation with geometry over the range of physical dimension studied.

3.2.3 Coupling induced dispersion

We have already seen the previous sections, there have been efforts in the literature to understand and control the linear propagation properties of light in silicon photonic wires [87, 88]. In the main, this has been achieved through controlling the properties of the individual waveguide or by surrounding it with materials of

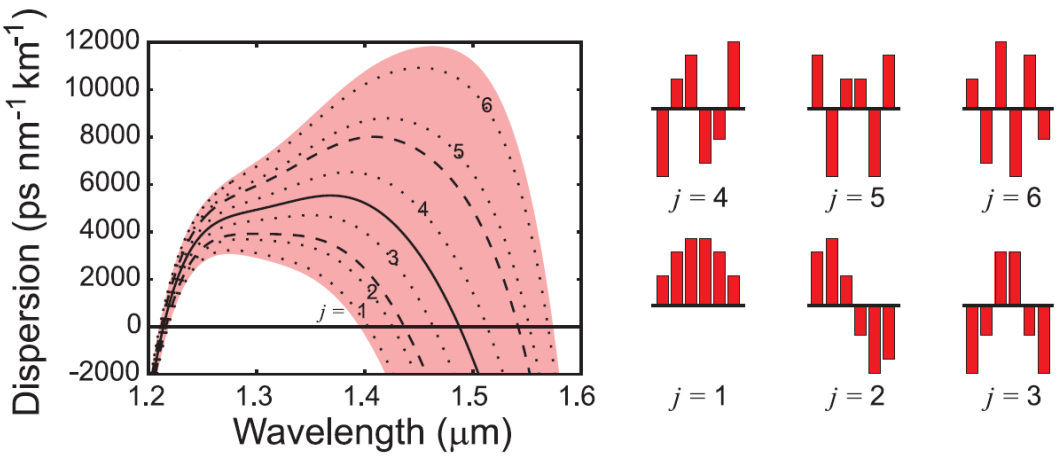

Figure 3-4: (left) Figure showing the dispersion of the quasi-TE supermodes of a single waveguide (solid), a two channel array of waveguides (dashed) and a six-channel array (dotted). (right) A schematic showing the six supermodes of a six-channel array. The supermode number relates to the dispersion curve shown on the left. Reprinted from [89].

different dielectric constant. More recently, a theoretical paper has suggested that this control can be achieved by using coupling-induced dispersion (Fig. 3-4) [89].

In the following work we consider the regime whereby the waveguide dimensions are small, and there is strong coupling due to the small separation between adjacent wires. In this regime, the coupling between the wires is strongly dispersive but remains evanescent. To understand this theoretically we assume the tight binding approximation; that the modes of the coupled system, also known as supermodes, are a linear superposition of the modes of the each individual waveguide that makes up that system [90, 91].

Consider the envelopes of the symmetric and antisymmetric supermodes, A_s and A_a respectively

$$A_s = \frac{1}{2}(A_1 + A_2) \tag{3.14}$$

$$A_a = \frac{1}{2}(A_1 - A_2) \tag{3.15}$$

where A_1 and A_2 are the envelope functions of the individual wires. By

applying the tight binding approximation, the propagation constants of each supermode can be written as $\beta_{s,a} = \beta(\omega) \pm \delta(\omega)$ where $\delta(\omega)$ is a small perturbation that is dependent on the coupling strength. In almost all cases the symmetric supermode has a higher effective index, meaning that $\delta(\omega)$ is positive. By altering the waveguide separation, the coupling can be altered through the extent to which the evanescent field of the individual waveguide modes overlap. In this case, the frequency dependence of the coupling can be approximated as

$$\delta \approx \delta_0 e^{-x(\omega-\omega_0)} \tag{3.16}$$

where x is a positive constant. If we make a Taylor expansion on both the propagation constant and the coupling coefficient, then the linear propagation will continue as

$$\frac{\partial A_{s,a}}{\partial z} + \sum_{m=0}^{M} i^{m-1} (\beta_m \pm \delta_m) \frac{\partial^m A_{s,a}}{\partial t^m} = 0 \tag{3.17}$$

By substituting the definition of A_s and A_a from above, and rearranging these equations for A_1 and A_2 such that

$$\frac{\partial A_{1,2}}{\partial z} + \sum_{m=0}^{M} \frac{i^{m-1}}{m!} \left(\beta_m \frac{\partial^m A_{1,2}}{\partial t^m} + \delta_m \frac{\partial^m A_{2,1}}{\partial t^m} \right) = 0. \tag{3.18}$$

This equation is just a different formalism of our standard wave equation for a single wire. The only difference is the added term. This extra term,

$$\sum_{m=0}^{M} i^{m-1} \frac{\delta_m}{m!} \frac{\partial^m A'}{\partial t^m}, \tag{3.19}$$

defines the contribution from the envelope of the neighbouring waveguide, A', and the relative strength of such an interaction, through δ_m.

Coupling Length

We can now define a coupling length between the waveguides as the distance over which the light couples from a single waveguide into the an adjacent waveguide. It can also be defined as the propagation distance when the light has coupled from one waveguide to its neighbour and back to the original waveguide, in which case it is a factor of two larger. The derivation for this can be found elsewhere [2, 16] but only the result is included here

$$L_c = \frac{\pi}{2|\delta_0|} = \frac{\pi}{|\beta_s - \beta_a|} \tag{3.20}$$

3.2.4 Slot Modes

For all the silicon waveguide modes so far, we have considered only the modes of a high index silicon waveguide surrounded by a low index material. This mode is not completely confined to the silicon and has evanescent tails that extend into the surrounding medium. The magnitude of these tails is defined by the continuity of the electric flux density, D, normal to the interface between the core (the waveguide) and the cladding material. The corresponding electric field must undergo a large discontinuity at this interface, with a much higher amplitude on the side of the interface with the lower refractive index. By putting two waveguides very close to one another, the evanescent tails can combine to greatly enhance the confinement of light within a low-index slot region. This mode is thus defined as a slot mode and an example field plot is shown in figure 3-5.

It has been shown in the literature that high intensities can be achieved in the low index slot between high-index silicon photonic wires [92] and in metal-void nanostructures [93], the analytical analysis of which is shown in both works. This phenomena yields applications across many areas of nonlinear optics, including nonlinear switching [94]. Nonlinear effects in silicon photonic wire arrays can be enhanced by working in the slot mode regime where the magnitude of the electric field vector can be greatly increased, enhancing the nonlinear interaction within the material. In this case, the power does not reside in the silicon. To take advantage of the higher electric fields, a suitable nonlinear polymer should

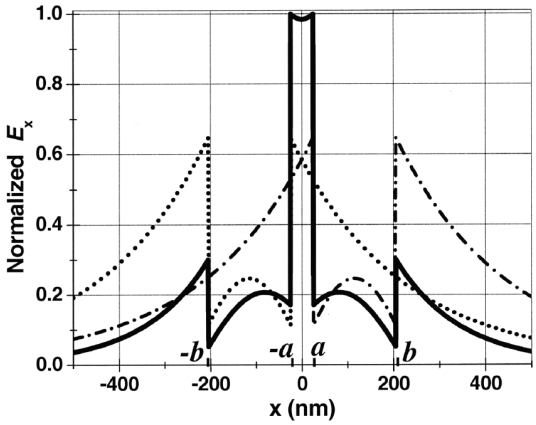

Figure 3-5: Normalised transverse electric field distribution of the fundamental TM eigenmode (solid curve) for a 2-dimensional slot waveguide consisting of two 180 nm wide silicon waveguides ($n = 3.48$), separated by a 50 nm wide slab of silica ($n = 1.44$). The waveguides are also surrounded by silica. Also shown are the individual slab modes for the TE eigenmode of each silicon waveguide given that the adjacent waveguide was missing (dotted and dashed-dotted lines). Reprinted from [92].

be used to fill the slot [94]. This will not only increase the nonlinearity, supposing the polymer is more nonlinear than silicon, but will also reducing the effects of two photon and free carrier absorption observed when the power is in the silicon wires.

3.3 Fabrication of Real Devices

The waveguides used for the following experimentation were fabricated by my collaborators at the University of Glasgow [95–99]. The information included in this section was not performed by the author of this thesis, but is included as a brief summary to waveguide fabrication. Further information can be found in the references it contains.

The fabrication starts with a silicon wafer. This is treated with a process called SIMOX [100] (separation by implantation of oxygen) whereby a 5 μm thick layer of oxygen ions are implanted into the wafer using an ion beam, leaving a small surface of silicon, approximately 200 nm thick, at the surface of the wafer. The oxygen-rich layer is then converted into a native oxide in a high temperature

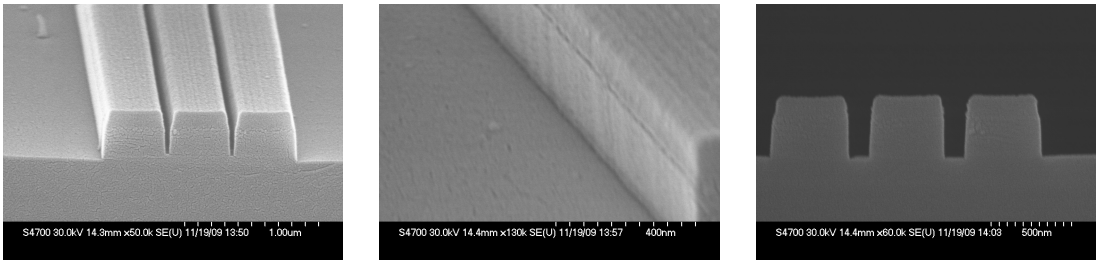

(a) (b) (c)

Figure 3-6: SEM micrographs of a three-channel array of silicon waveguides. These comprised of a 220 nm x 380 nm silicon channel on top of a 20 nm silica pedestal with a 160 nm HSQ mask layer on top. Different wall to wall separations were fabricated on the same sample. The good side wall verticality ((a) and (c)) and minimal line-edge roughness (b) are clearly observed.

annealing process. Other processes for obtaining a buried oxide layer are used, such as a smart-cutting process [101].

To pattern the waveguides a hydrogen silsesquioxane (HSQ) mask was used and patterned using a VISTEC VB6 e-beam lithography machine. HSQ is a positive resist and as such irradiation with electrons causes it to become resistant to etching with certain chemicals. The remaining resist, and silicon underneath is etched completely using fluorine based chemistry (SF_6 and C_4F_8) in an STS-ICP machine. The inductively-coupled-plasma (ICP) reactive-ion-etching (RIE) process employs radio frequencies to create a plasma from the reactive gas mixture. A second radio frequency source is coupled to the sample, creating a voltage bias, which extracts the reactive species from the plasma and accelerates it towards the sample, allowing highly anisotropic etching to be performed. Once at the sample either chemical or mechanical etching takes place, removing the etchable species [102]. The choice of mask and chemistry has been shown [95, 98] to have high resolution at moderate sensitivity and provide minimal line edge roughness due to its high level of etch resistance (Fig. 3-6). The criticality of the line edge roughness has already been discussed with respect to loss and coupling. Using the above technique the side wall verticality of the underlying silicon structures has been reported above 88° [98].

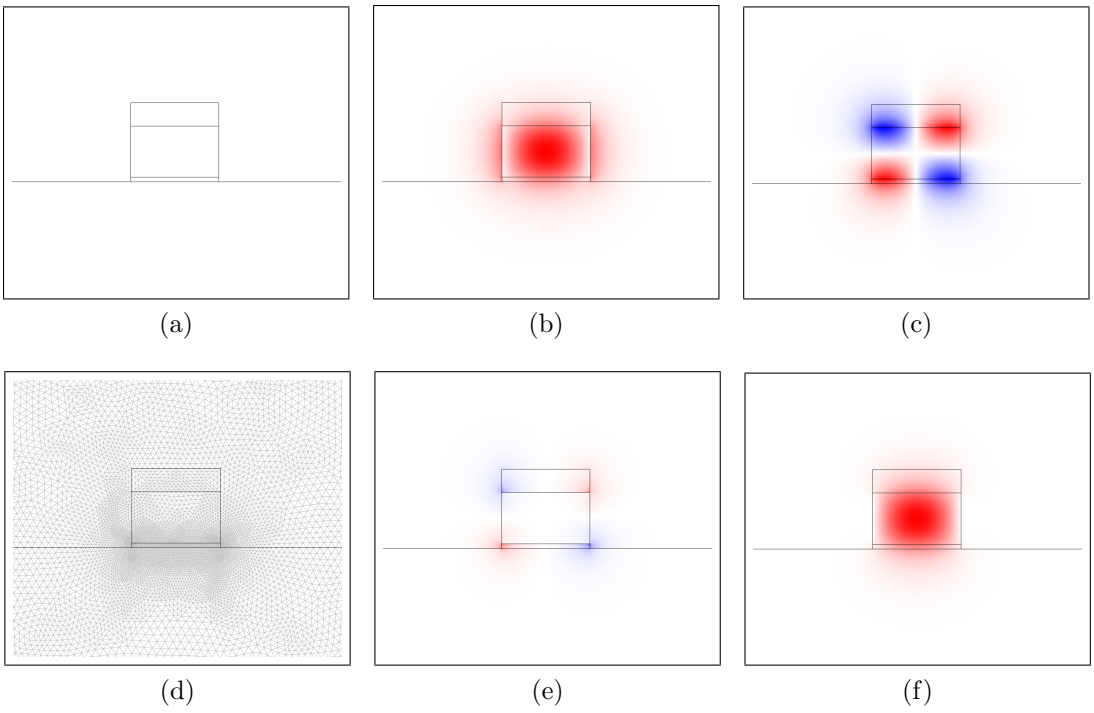

Figure 3-7: Images of the modelling space. (a) Geometry of the structure under test. This is surrounded by a 4 μm square boundary. (d) A zoom of the mesh used for the analysis. This shows that the element size is a minimum near the internal boundaries of the modelling space. The remaining plots are the field components oft the quasi-TE mode: (b) E_x, (c) H_x, (e) E_y and (f) H_y. In this figure, the x and y directions are horizontal and vertical on this page respectively.

3.4 Modelling Coupled Silicon Photonic Wires

There are many readily available software packages that can solve Maxwell's equations to find the propagation constant, β, and modal profile, F, of a defined geometry at a given wavelength. In this work, the RF module of Comsol Multiphysics has been used to calculate all of these values. A brief discussion of the methods used to calculate this are discussed in the preceding chapter on photonic crystal fibres.

The silicon-silica waveguide geometry is defined by a series of enclosed shapes, each with its own set of parameters (figure 3-7). The main parameter of use here is the refractive index, and to model the devices the refractive index of silicon was assumed to follow the modified Sellmeier equation, as defined above, and

that of silicon to follow the standard Sellmeier equation. After discussion with collaborators, it was defined that the post irradiated refractive index of HSQ was also very close to that of silica, so an identical equation was used.

The output of the software is not only the modal profile, as shown in figure 3-7, but also the corresponding values of the propagation constant. For our simple single channel structure as seen in the figure, we obtain two modes. These modes, can be defined as quasi-TE_0 and quasi-TM_0 modes. The term TE (TM) here is determined from the early work done on slab-waveguide geometries and is here taken to mean that the main component of the electric field (magnetic field) is parallel to the silica-silicon interface. The modes are defined as quasi-TE due to the fact that the electric field component along the direction of propagation is non-zero, but very small. Finally, the subscript denotes that these modes are fundamental modes of the waveguide and contain no nodes. Throughout this thesis the terms, quasi-TE_0, quasi-TE and TE will be used interchangeably to describe this mode.

For the remainder of this thesis we shall predominantly consider the TE modes above all. As can be seen from the cross sections of the two modes (figure 3-8) we see that the TE modes are more confined within the silicon. The result will be that more nonlinear response of this mode should be higher. Even given this, the more tightly confined mode means that any coupling between adjacent wires will be weaker due to the reduced interaction between modes of adjacent wires. One important point to note here is that the TE modes are the only modes to exhibit the slot-mode behaviour discussed in the preceding sections.

3.4.1 White-Light Interferometry

Historically, white-light received much attention as a source for measuring the dispersion characteristics of materials [103–107], with particular emphasis on measuring the group-delay dispersion using an interferometer. Two methodologies have been presented in the academic literature. The first employs multiple measurements of the centroid of the interference patterns from spectrally filtered pulses of a white light source [104, 105]. The second involves using the entire bandwidth of the source and obtaining the information from the Fourier transform of a single measurement [103, 106, 107].

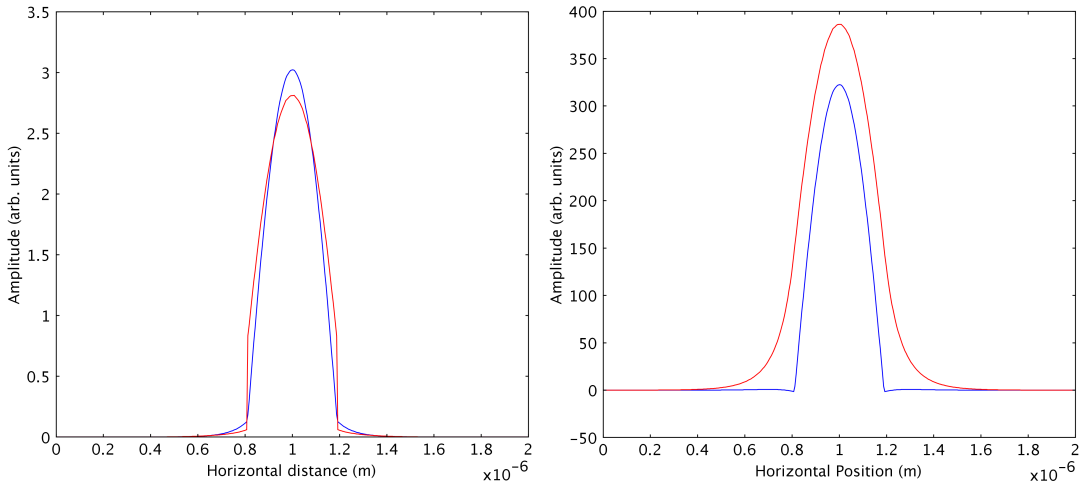

(a) (b)

Figure 3-8: Figure showing the comparison of the horizontal confinement of the electric and magnetic fields for the TE and TM mode as defined through the centre of the waveguide. (a) Horizontal extent of the E_x (blue line) and E_y (red line) fields for the TE and TM mode respectively. (b) Horizontal extent of the H_y (blue line) and H_x (red line) fields for the TE and TM mode respectively. Clearly, although the electric field shows similar levels of confinement the magnetic field is much less confined in the TM mode.

In the work by Scott Diddams and Jean-Claude Diels they show the fundamentals behind both regimes [103]. Here, we shall overview their analysis to explain the measurement system employed in this thesis. Whilst the literature discusses a Michelson interferometer directly there are no differences when considering the Mach-Zehnder interferometer discussed later in the subsequent sections of this Chapter.

To understand the measurement technique, consider an input field, $E_1(t)$ that is split in two by the input beamsplitter of an interferometer (fig. 3-9). In the absence of a sample, we can consider the field from the stationary arm and that from the delayed arm as $E_2(t)$ and $E_1(t-\tau)$ where τ is the temporal delay induced by increasing the path length of the delayed arm by a distance x.

With continuous increase of this delay, a square-law detector at the output of the interferometer will measure the interferogram that results from the two fields

moving in and out of phase with each other [103]. As a function of this delay the interferogram has the form:

$$I(\tau) \propto \langle \mathcal{E}_1^2(t-\tau)\rangle + \langle \mathcal{E}_2^2(t)\rangle + \langle \mathcal{E}_1(t-\tau)\mathcal{E}_2^*(t)\rangle \exp(-i\omega_l t) + \langle \mathcal{E}_1^*(t-\tau)\mathcal{E}_2(t)\rangle \exp(i\omega_l t) \tag{3.21}$$

where the angled brackets denote the time average performed by the detector and we have used a complex field representation such that

$$E_1(t) = \mathcal{E}_1(t)\exp(i\omega_l t)/2. \tag{3.22}$$

The first two terms of equation 3.21 denote the constant average intensity of the two beams. The second two correspond to the interference information in the form of first-order correlations between the two beams. Using the Fourier transform to move to the frequency domain, and introducing a shifted frequency, $\Omega = \omega - \omega_l$, the correlation function is given by

$$A_1^+(\Omega) = \mathcal{E}_1^*(\Omega)\mathcal{E}_2(\omega). \tag{3.23}$$

This simple case obviously needs to be extended to consider the inclusion of a dispersive medium within one of the arms. This is achieved mathematically by using a complex optical transfer function with a frequency dependent amplitude filter and a path-length dependent phase factor, $T(\Omega)exp[-ik(\Omega)]$. The Fourier transform of the measured correlation then becomes:

$$A_2^+(\Omega) = r_{12}(\Omega)\left|\mathcal{E}(\Omega)\right|^2 T(\Omega) \times \exp\left\{-id\left[k(\Omega) - \frac{\Omega+\omega_l}{c}\right]\right\} \tag{3.24}$$

where $r_{12}(\Omega)$ is a complex, frequency dependent function representing amplitude losses and any unbalanced phase shifts in the two arms and d is the

length of the sample (if the sample is only traversed once, as per a Mach-Zehnder interferometer).

The phase term of equation 3.24 describes the dispersive properties of the medium added into the empty interferometer. We can expand $k(\Omega)$ as a Taylor series and end up with a description of the higher order dispersions and their impact on the interferogram:

$$\begin{aligned}\mathcal{E}_2(\Omega) \approx & T(\Omega)\mathcal{E}_1(\Omega) \\ & \times \exp\left\{-id\left[k_l + k_l'\Omega + \frac{k_l''}{2}\Omega^2 + \frac{k_l'''}{6}\Omega^3 + \ldots\right] + i\frac{\Omega+\omega_l}{c}d\right\}. \quad (3.25)\end{aligned}$$

Each of the different terms of the expansion plays a specific role in the observed characteristics of the measured interferogram. However, for the rest of this work we shall be using a spectrally filtered input pulse with a bandwidth of 10 nm. By combining this with the fact that we only considering the shift of the interferogram rather than its frequency content (as per [104, 105]) we can truncate the expansion to first order in Ω [103]. It is known that an exponential factor linear in Ω transforms into a time shift. The inverse Fourier transform of the truncation of our Taylor expansion (eqn. 3.25) yields a complex field envelope that looks like:

$$\mathcal{E}_2(t) = \exp\left[\frac{-i\omega_l d(n_l - 1)}{c}\right]\mathcal{E}_1(t - \Delta t) \quad (3.26)$$

where the time delay, Δt, is given by

$$\Delta t = \frac{d}{c}\left[(n_l - 1) - \lambda_l\left(\frac{dn}{d\lambda}\right)_l\right] = \frac{d}{v_g}. \quad (3.27)$$

Interferogram Shape

From the above analysis it can be seen that the shape of the interferogram is closely related to the shape of the input pulses. It has been shown in the literature [108] that for Gaussian or sech-shaped pulses the interferograms also show

the same shape. For the work which we followed the analysis from in the previous section the measured interferograms from a balanced interferometer were Lorentzian in shape. This however was attributed to a limit in the bandwidth of the measurement source and not expected given the statistical nature of the white light [103].

3.5 Experimental Determination of Dispersion

In order to verify the modelling results, low coherence white-light interferometry measurements were taken in a Mach-Zehnder configuration (see figure 3-9). The arrangement consisted of two light sources co-incident on a 10 m length of solid-core photonic crystal fibre: a continuous-wave (CW) distributed feedback diode laser at 1510 nm, and a Q-switched microchip laser generating 700 ps pulses with a central wavelength of 1064 nm at a repetition rate of approximately 10 kHz. The fibre has a 5 μm core and when pumped by the microchip laser generates a broad-band optical supercontinuum extending from 400 nm to approximately 2300 nm [4, 109]. As we have seen with the refractive index of silicon, there is a sharp absorption band in the low-infrared region. To stop optical and thermal damage to the samples from absorption in this region a low-pass (long wavelength) filter was placed directly after the photonic-crystal fibre.

In the standard Mach-Zehnder arrangement the beam is split into two arms using a non-polarising beam splitter cube; one containing the sample and the other used as a reference beam. Bulk objective lenses (60×, NA = 0.65) were used to couple into and out of the waveguide arrays tested and an identical pair of lenses were put in the path of the reference arm so that any dispersion present in the glass would be cancelled out in the measurement. To minimise any error in variation between optical elements, and to ease alignment, no other optics were present inside the interferometer cavity. The beams are recombined using another non-polarising beam-splitter cube and there is a polarisation selection element (a rotatable polariser) before the light is focused onto a femtowatt photoreceiver via a length of single-mode fibre. Finally, wavelength selection is done by inserting bandpass filters (with a 10 nm full-width-half-maximum (FWHM)) into the beam. Bandpass filters with a central wavelength between 1200 nm and 2000 nm, in approximately 50 nm steps were used.

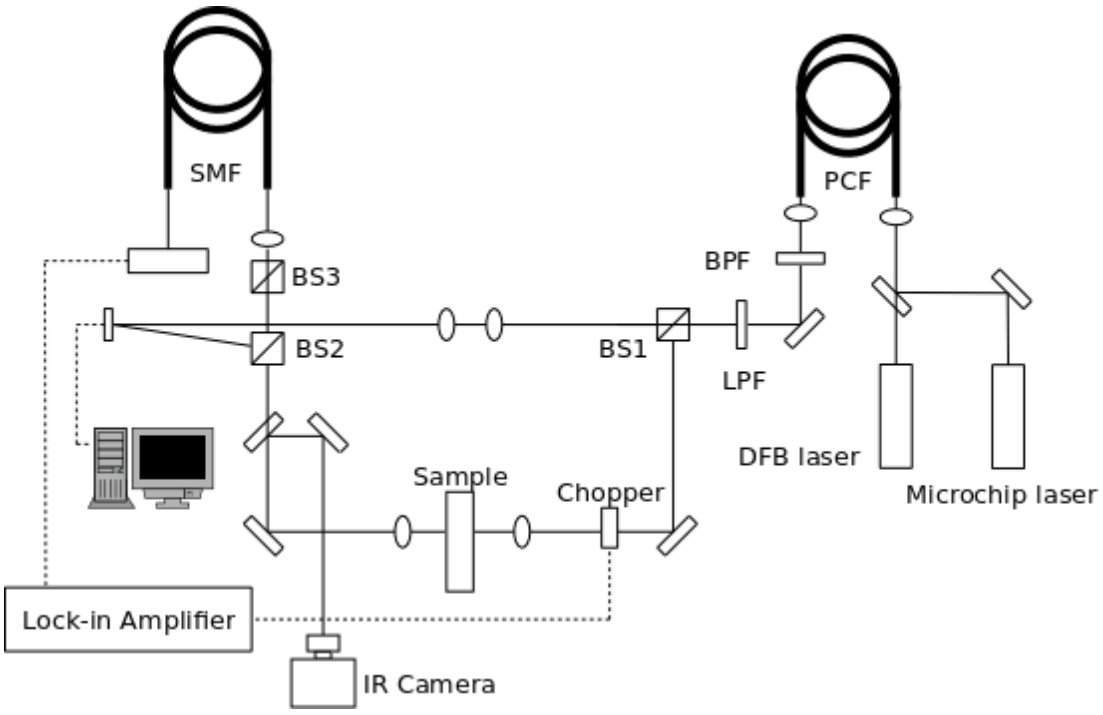

Figure 3-9: Schematic of the experimental set-up for low coherence white light interferometry. The dual arm Mach-Zehnder configuration can clearly be observed. To the right of the diagram are two laser sources as described in the text, BPF and LPF are the band-pass and long-pass filters respectively and BS1 through BS3 denote the three beam-splitter cubes, of which BS3 is polarised and the other two are not.

The measurement set up actually measures the group-delay, the temporal delay in travelling through a medium at a given mode's group velocity. In a balanced interferometer, the two arms would interfere constructively and a signal would be obtained. By changing the optical path-length in either of the arms, the phase between the light in each arm changes. This creates a series of fringes. This optical path length change happens in the sample arm due to the group delay induced by the sample for each specific wavelength. To match this delay, the physical length of the reference arm is changed using a computer-controlled motorised stage. The change of length of this arm, compared to when no sample was present, gives a measurement of the group delay inside the sample.

Coupling to and from the waveguides was made repeatable by the use of the DFB laser and an InGaAs array camera. This was either mounted in the

output beam from the sample to view the output intensity pattern, or on a Zeiss V6 microscope directly above the sample. The latter view provided a look at scattering loss and was used as an initial placement tool, after which the view was changed to the former description. The InGaAs camera used had a spectral range up to 1700 nm and thus measurements above this had to be aligned using the photoreceiver at the output of the interferometer.

3.6 Analysis

Two different regimes were considered during experiments, the first is arrays with large separation. To test this, an array of 3 channels, with cross-section 220 nm by 380 nm, were examined. They had a wall-to-wall separation of 600 nm. Each waveguide was capped with a 160 nm thick layer of HSQ mask left over from the etching process and stood on a 20 nm thick silica pedestal. The pedestal is the result of a slight over-etch to ensure that the silicon was completely etched through. In this regime, we are mostly interested in looking at coupling-induced dispersion for the three-mode system.

The second regime is arrays with small separation. To examine this configuration, an array of only 2 channels is considered. These also have a cross section of 220 nm by 380 nm but have a wall-to-wall separation of only 100 nm. The other features of the surrounding dielectric are as described above. Each of these regimes will be treated separately.

3.6.1 Waveguide Arrays with Large Separation

To analyse the data from the interferometer, the quasi-TE and quasi-TM modes had to be separated (figure 3-10a). This was done by using a rotatable polarising beam-splitter in the output beam of the waveguides (BS3 in figure 3-9). Once this had been done, the interference fringe packet was analysed to see if the component for each supermode was extractable.

A Fourier transform method previously used to characterise a fibre-mode converter [110] was tested. This method involves recording interference field profiles of an interferometer for different reference arm lengths and then using Fourier analysis to extract beat frequencies and filter the relative spatial components con-

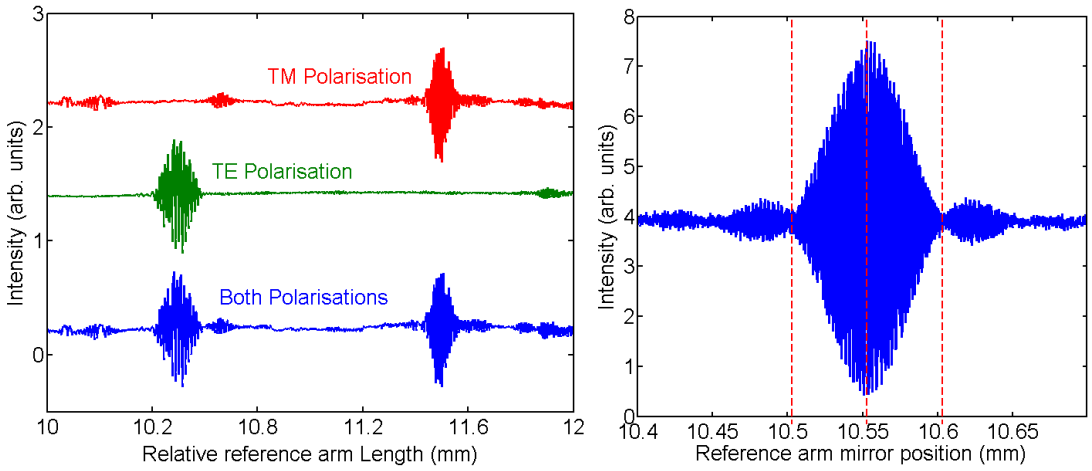

(a) (b)

Figure 3-10: (a) Plot of representative interference fringes, with no polarisation control and then showing the different polarisation components by rotating the polarising beam splitter cube BS3 (figure 3-9). As can clearly be seen, the two interference fringes correspond to a TE like and TM like modes. The TE only and TM only traces have been offset for clarity. (b) Higher resolution scan of the interference fringe. The vertical markers denote the centroid of the fringe and the extremal values that were used to mark the physical extent of the fringe packet.

tributing to each frequency. It was hoped that for each section of the interference fringe, the supermode might be extractable. Unfortunately, the assumption of this work is that the output field is well defined. In this sample this was not the case, and no further analysis could be performed.

There are three TE (and TM) supermodes supported by the geometry under test (figure 3-11). The transverse profile of the supermodes that an N channel array can support follows the following formula:

$$x_j = \sin\left(\frac{nj\pi}{N+1}\right) \tag{3.28}$$

where N is the number of channels in the array, j is the order of the supermode, and n is the waveguide number (nominally from left to right). Using this

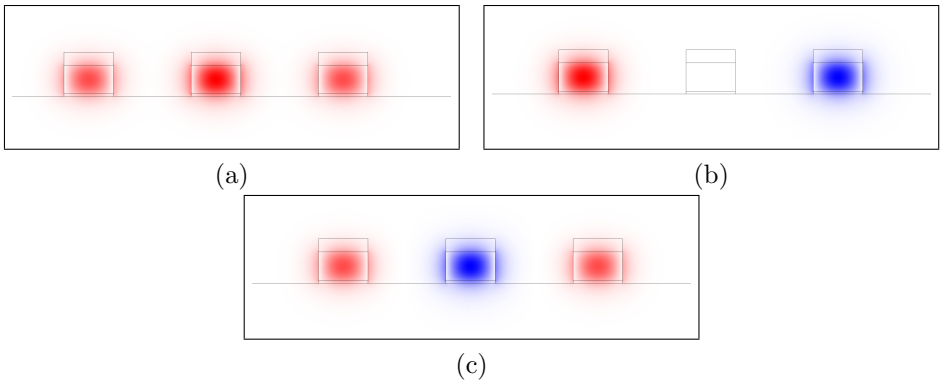

Figure 3-11: Figure showing the three different modes output from the numerical modelling of a three channel array. The modes can be characterised by their order j as given in equation 3.6.1: (a) defines a fundamental symmetric mode where $j = 1$, (b) defines an antisymmetric mode where $j = 2$ and (c) defines another symmetric supermode with a higher transverse wavenumber and $j = 3$.

formula, it can be seen that the electric field in fictional channels outside of our array, E_0 and E_{N+1} are both zero. A more formal discussion of this is found in a discussion by Benton [16].

Thus, we can define the different parts of the fringe with each supermode such that:

- the shortest reference arm length would correspond to the mode with the lowest group index. In the three channel case this is the fundamental mode (fig. 3-11 (a)) where $j = 1$.
- the maximal extent of the interference fringe corresponds to the mode with the highest group index. In the case of the three channel array, this is the symmetric mode with $j = 3$ (fig. 3-11 (c)).
- the centroid, or centre-of-mass, of the fringe corresponds to the decoupled mode (in this case the antisymmetric mode (fig. 3-11 (b)) where $j = 2$.

This fringe position was then converted into a group index via the relationship between the relative time delay in each arm of the interferometer. The change in mirror position ΔD yields a change in optical path length of $2\Delta D$ for the non-sample arm of the interferometer. This equates to a group delay of $2 * \Delta D/c$ where c is the speed of light. The group delay per unit length is then easily

calculable using the sample length, L. The inverse of the group delay per unit length is the group velocity. Thus the group velocity is given by:

$$v_g = \frac{cL}{2\Delta D}. \tag{3.29}$$

We can then use the relationship between group velocity and group index to yield:

$$n_g = \frac{2\Delta D}{L}. \tag{3.30}$$

However, this is not quite correct. What we have calculated is the relative group delay in response to replacing air with a sample of length L. This is therefore not a group velocity but a change in group velocity relative to the group velocity of the air. Therefore, the final equation that we should use is:

$$n_g = \frac{2\Delta D}{L} + 1. \tag{3.31}$$

These measurements were then compared to the numerical modelling for both the quasi-TE and quasi-TM modes (figure 3-12). At short wavelengths, the coupling induced dispersion is minimal and so the fringes observed have a minimum width. Let us consider the coherence length of our input pulses. The coherence length determines the distance over which the phase of the pulses can be determined. The coherence length, l_c, is defined by

$$l_c = \frac{\lambda^2}{2 * \Delta\lambda} \tag{3.32}$$

where λ is the centre wavelength of the radiation and $\Delta\lambda$ is the bandwidth of the pulse. For the filtered pulses of our experimental set up, where the bandwidth is 10 nm wide, a pulse centred at 1550 nm has a coherence length of 120 μm.

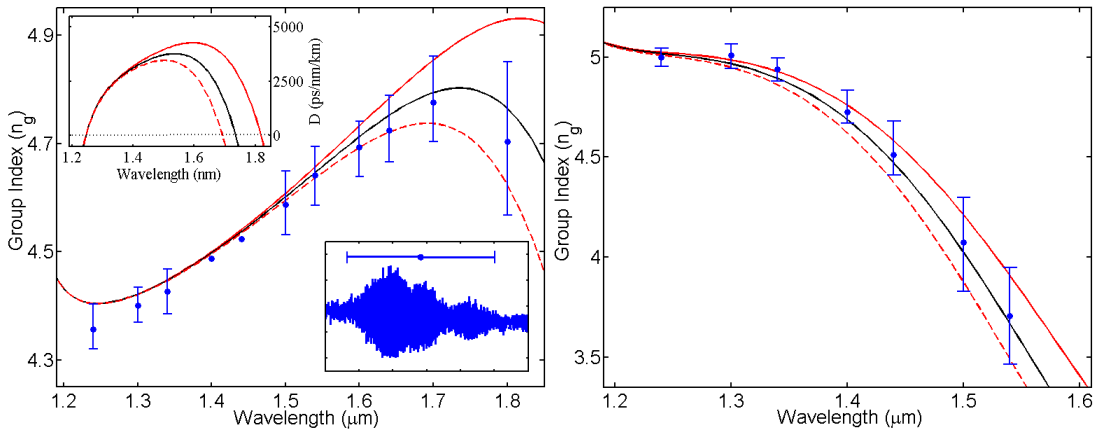

Figure 3-12: (a) TE mode group indices of each fringe analysed at each filter wavelength available (blue dots). The vertical bars mark the temporal extent of the fringe packet as defined in the text. The numerical modelling of the modes for $j = 1$ (red-dashed line), $j = 2$ (black line) and $j = 3$ (red-solid line) are also shown. Inset is shown the dispersion of each of these modes (with the same colour notation) and an example fringe taken at 1800 nm. (b) Group indices of the measurements of the TM mode.

This effectively defines the minimum width of our interference fringes due to the fact that the phase cannot be determined for differences longer than the path length difference [7]. As we have seen, the finite bandwidth of the filtered input pulses determines the length of the interferogram observed. However, the slope of the dispersion across this bandpass window will also be a factor in determining the interferogram width. As we are in the linear regime of propagation, there is no reason to believe that the temporal or spectral properties of the pulses should change. Given this, observing a fringe pattern smaller than that defined by the coherence length is not possible.

For wavelengths far above 1600 nm, it is observed that there is significant broadening of the interference fringes over this minimum limit. This is due directly to the coupling induced dispersion, described theoretically earlier in the chapter. The match to the numerical modelling of this array (fig. 3-12) is extremely good across the entire wavelength range. Two differences are apparent from the figures. Firstly the numerical data appears to be slightly below that expected from the modelling. Primarily this could be due to a discrepancy between

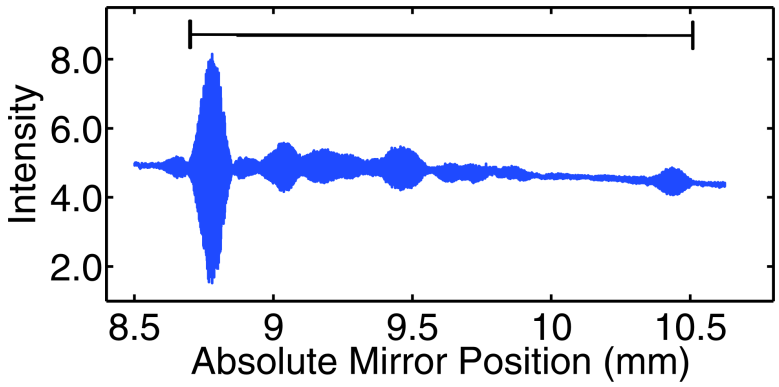

Figure 3-13: Representative interferogram measurement for the TE modes of a two channel waveguide array with small wall-to-wall separation. As can be seen, there are two extremal peaks with larger amplitude than any other features. In between these peaks is a series of other interference features, with a modulated amplitude.

the refractive index values as defined within the model space or simplifications that were made in calculating the group indices, such as the group index of air being exactly 1. The second thing is that the experimental data appears to have a turning point that is at shorter wavelengths than the numerical data. This is most likely due to a discrepancy between the modelled geometry and the numerical one. Slight changes in waveguide width, of only a few nanometres can change the position of the turning point considerably [87].

3.6.2 Waveguide Arrays with Small Separation

In order to more clearly observe the splitting of the interference fringe into separate supermode components, the coupling-induced dispersion needs to increase above that observed in arrays with large separation as discussed in the preceding section. Experimental measurements were made on waveguides of a two channel array, similar to those already used but with a 100 nm wall-to-wall separation. A two-channel array was considered here to make fringe analysis easier, as only two supermodes exist for each polarisation; a symmetric and anti-symmetric supermode.

The fringe analysis is however not trivial as can be seen from the representative interference fringe for the TE polarisation, taken using a band-pass filter with

a central wavelength of 1500 nm (figure 3-13). Using a similar argument to before, the extremal peaks can be identified with travel through the array in either of the two supermodes: the symmetric (antisymmetric) mode having the lower (higher) group index and being at the short (long) reference arm length end of the interference fringe. In almost all of the fringes the amplitude of these peaks are much higher than the interferogram within a coherence length of their centroid and are thus well formed. Interestingly the amplitude of the interference fringe from the symmetric mode is always higher than the antisymmetric mode (as can be seen in 3-13 and the inset of 3-12). This would most likely be due to the different mode composition at the input of the waveguide array. Given that the spot size of the illuminating beam is of the order of the size of the whole array then it is a good assumption that the overlap with the symmetric mode of the waveguide array is good and a larger proportion of power will be transferred into this mode.

The modulation between these extremal parts of the interferogram is more difficult to understand. Both of the TE and TM modes are only quasi-TE and quasi-TM and have a small but finite field in the z-direction. We therefore need to rethink our assumption that the waves propagate down the waveguide with no coupling between the TE and TM modes. Coupling could occur between each of these modes within the waveguide. The polarisation controller was moved within the set up to be next to the bandpass filter to try and remove this effect. The results were exactly the same. This could be due to the impossibility of completely filtering out one or other of the polarisation modes. One other explanation could be the coupling of modes through a scattering point. Modes of opposite symmetry but the same polarisation (TE) could couple in the presence of a significant scattering point or defect within or around the waveguide structure. However, no significant scattering points were observed during the alignment process, when viewing the waveguides from above. As yet, the author has no other explanation for the modulation.

If we consider only the extremal peaks of the interferogram, over the whole measurement region of interest (figure 3-14a) then we observe that the coupling induced dispersion is much larger than for the large separation regime, as expected. It can also be shown that for this geometry the coupling-induced group velocity dispersion is larger than the group velocity dispersion, caused by ma-

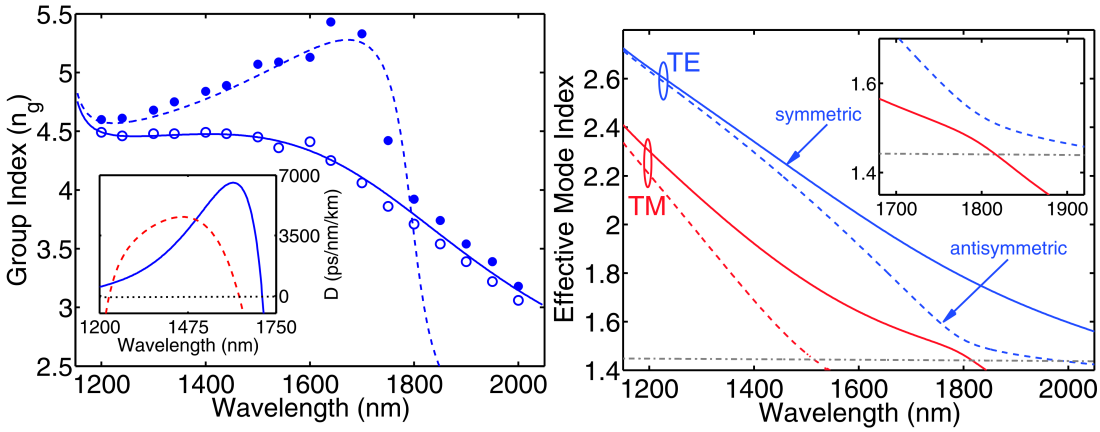

(a) (b)

Figure 3-14: (a) Graph of experimentally measured group index of a two-channel array of 220 nm by 380 nm waveguides with a 100 nm wall to wall separation. The filled (empty) blue circles correspond to the maximal (minimal) peak of the interferogram for each wavelength (see figure 3-13). The numerical modelling results for the symmetric and antisymmetric modes are also shown (solid and dashed lines respectively). Inset is a plot of the single waveguide dispersion (red) plotted against the coupling induced dispersion of the two-channel array. Beyond 1800 nm only a single fringe is observed for the TE polarisation. (b) Numerical modelling of the effective index of the TE and TM modes of the two-channel array. Inset is an expanded view of an anti-crossing feature observed.

terial and waveguide effects, for an individual waveguide (figure 3-14a inset) as theoretically predicted [89].

What is also observed in the analysis is that at approximately 1800 nm there is a shift to a single interference with symmetric symmetry. By looking at the observed, numerical field patterns for the symmetric modes before and after the transition, we can see that the supermode has changed. Instead of two modes that are well contained by the silicon (figure 3-15a and 3-15b) we can see that there exists only a single mode and that the majority of the electric field intensity, and also the power, is confined to the slot between the waveguides (figure 3-15c).

To observe this transition a little more closely, we consider the numerical calculation of effective index (figure 3-14b). The antisymmetric mode will be cut-off when its effective index drops below the refractive index of silica. At this point it is not guided by the silicon and disperses into the substrate. This can

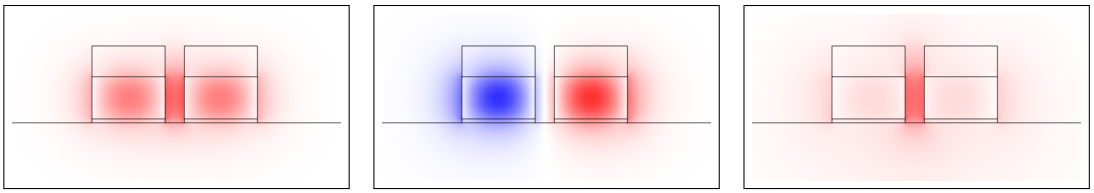

(a) (b) (c)

Figure 3-15: Electric field component parallel to the silicon-silica interface for the symmetric and anti-symmetric quasi-TE supermodes before the waveguide-mode to slot-mode transition at 1400 nm ((a) and (b)) and the symmetric quasi-TE mode, or slot mode, after the transition at 1950 nm (c).

clearly see to be the case at approximately 1800 nm, as observed experimentally, but an anti-crossing is also observed at this point. The highly dispersive anti-symmetric mode drastically changes effective index until it has the same effective index as the symmetric TM mode. As the modes have the same symmetry (figure 3-16a and 3-16d)), they would be degenerate at this point. This degeneracy is forbidden and as such the modes convert from one to the other.

This anti-crossing is a result of the vertical asymmetric mode confinement induced by the vertical asymmetry of the geometry under test. Under the waveguide is a block of silicon, whilst on top of the waveguides are individual caps of HSQ, which can be approximated to behave like silicon after irradiation. This mismatch means that as the confinement of the modes by the silicon gets weaker (at longer wavelengths) the individual lobes of the antisymmetric TE mode see a different local geometry . This causes them to be confined in a different spatial configuration (figure 3-16b). This configuration becomes more and more TM mode like (figure 3-16c) as the wavelength increases. This change forces a change to the effective index of the mode, and complementary changes to the effective index and field profile of the symmetric quasi-TM mode. After the anti-crossing, the resultant field of the TE mode is exactly the same as a less confined version of the TM mode from before the transition. At this point ,the effective mode index of the anti-symmetric TE mode drops below refractive index of silica and is no longer a confined mode of the silicon nanostructures. At this point we have only two modes of our system, both of which can be thought of as slot modes.

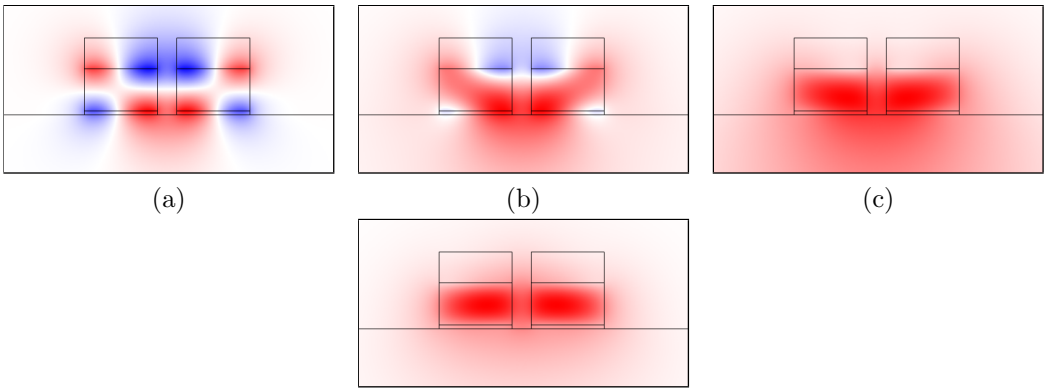

Figure 3-16: Numerically calculated mode profiles for the magnetic field component parallel to the silicon-silica interface, for the antisymmetric quasi-TE mode (at 1650 nm (a), 1790 nm (b) and 1950 nm (c)) and the symmetric quasi-TM mode (at 1650 nm (d)) near the anti-crossing.

3.7 Summary

In this chapter we have shown that dispersion is an important property of silicon waveguides. This dispersion is a controllable quantity through the interaction with other closely spaced waveguides. Numerical calculation and experimental results confirm that we have observed coupling induced dispersion in coupled waveguide arrays on the order of, or greater, than the group-velocity dispersion of a single waveguide of similar dimensions. In this chapter we have also observed, both numerically and experimentally, the transition from a waveguide-guidance regime to a slot-guidance regime. During analysis of this transition an anti-crossing has been observed numerically. The presence of this anti-crossing has been explained through the vertical asymmetry of the geometry under consideration.

Chapter 4

Silicon Photonic Wires in the Nonlinear Regime: Modulation Instability

4.1 Introduction

The following chapter extends the work on linear optics presented in Chapter 3. In this work we examine the non-linear phenomenon of modulation instability inside both isolated and coupled silicon photonic wires. Section 4.2 will discuss the background theory. This will be followed by a discussion of previously published academic literature in section 4.3. Once we have introduced the relevant background, section 4.4 will discuss my work on both numerically and experimentally studying modulation instability in silicon photonic wires. I shall put particular emphasis on describing the complicated experimental set-up. I shall compare numerical analysis from the academic literature to the results of these experiments. Finally, in section 4.5, I will discuss the paper published by researchers at Bath that followed on from this work.

4.2 Optical Nonlinearity

We have already defined, in the introductory chapter the concepts of nonlinear refractive index, the Kerr effect and self-phase modulation. However, in order to

understand more complex nonlinear behaviour, and in particular when we deal with pulses, we should consider nonlinearity in more detail and introduce the non-linear Schrödinger equation.

4.2.1 Third-Order Susceptibility

In Section 1.6 we discussed Kerr nonlinearity and the nonlinear relationship between the applied field and dielectric polarisation of a medium. To do this we expanded the polarisation in a Maclaurin series (equation 1.22). The result was a set of tensors, describing the linear, $\chi^{(1)}$, and nonlinear, $\chi^{(m>1)}$, relationship between the polarisation and electric field. To describe nonlinearity in silicon and silica, we can ignore the first nonlinear term, $\chi^{(2)}$, due to inversion symmetry and also ignore higher order terms due to their relative magnitude. We are left with considering only the third-order susceptibility, $\chi^{(3)}$. The term in our description of the polarisation (equation 1.22) that depends on the third-order susceptibility implies an interaction between three electric fields to produce a fourth field [111]. The $\chi^{(3)}$ interaction is thus a four-photon process. Given this, the generalised polarisation arising from this third order susceptibility is given by:

$$P^{(3)} = \epsilon_0 \chi^{(3)} \left(\omega; \omega_i, \omega_j, \omega_k\right) \vec{E}\left(\omega_i\right) \vec{E}\left(\omega_j\right) \vec{E}\left(\omega_k\right) \tag{4.1}$$

where the third-order susceptibility term defines:

$$\chi^{(3)} \left(\omega; \omega_i, \omega_j, \omega_k\right) = \chi^3 \left(\omega = \pm\omega_i \pm \omega_j \pm \omega_k\right) \tag{4.2}$$

for $i, j, k = 1$. Given this there are 108 different terms covering all the possible permutations of the three fields at each of the three frequencies. This does not mean that there are 108 different mechanisms describing nonlinear interactions. The third-order nonlinear polarization defined by (equation 4.1) is responsible for mechanisms such as four-wave mixing, Kerr-effect phenomena such as self-phase modulation, Raman scattering and two-photon absorption [112]. Each of these

mechanisms has its own component or components within the $\chi^{(3)}$ tensor that govern their behaviour.

The most general case is when all four fields are at different frequencies and we have four-wave mixing (FWM). There are then a myriad of degenerate cases:

- all three laser fields have the same pump frequency, ω_0, and the generated field has a frequency $\omega_{FWM} = 3\omega_0$. This is third-harmonic generation, controlled by the third-order susceptibility element $\chi^{THG} = \chi^{(3)}(3\omega_0; \omega_0, \omega_0, \omega_0)$.

- if a frequency difference of two of the fields is tuned to a resonance with a Raman-active mode of the medium then the four wave mixing, $\omega_{FWM} = \omega_{CARS} = \omega_1 - \omega_2 + \omega_3$, then we refer to this as coherent anti-Stokes Raman scattering (CARS).

There is also a component of the $\chi^{(3)}$ tensor that defines the effect of three frequency-degenerate fields on the polarisation at their own frequency. The corresponding tensor element, $\chi^3(\omega; \omega, \omega, -\omega)$, is responsible for this and is referred to as the Kerr-type nonlinear susceptibility. This component generates the nonlinear refractive index, n_2 discussed in Section 1.6 through [16, 111]:

$$n_2 = \frac{3}{4\epsilon_0 c n_0^2} \chi^{(3)}(\omega; \omega, \omega, -\omega). \tag{4.3}$$

For very short laser pulses and broadband field waveforms, SPM can be thought of as a four-wave mixing process ($\omega_{p1} + \omega_{p2} = \omega_3 + \omega_4$), where we have two pump photons at frequencies ω_{p1} and ω_{p2} generating new frequency components at ω_3 and ω_4. The pump photons can also be degenerate, whereby the new frequency components generated through FWM appear as Stokes and anti-Stokes sidebands in the output field spectrum. Under certain conditions, the pump modifies the refractive index and phase matching conditions of the modes involved in the FWM process, leading to a rapid growth of the Stokes and anti-Stokes signals [111].

This is what is known as modulation instability, whereby two photons from a pump field, with frequency ω_p generate sideband frequencies with frequencies $\omega_p \pm \Omega$.

4.2.2 Nonlinear Schrödinger Equation

Pulse propagation dynamics in waveguides can generally be described by the nonlinear Schrödinger equation (NLSE), which has been derived in many textbooks and publications [2, 16, 113, 114]. Although it is a nonlinear propagation equation concerned primarily with optics, its functional form is similar to that of the Schrödinger equation from quantum mechanics in that we have two differential components and a component related to the total energy, or in this case the nonlinearity.

In the absence of higher order dispersion effects the equation is given by:

$$i\frac{\partial A}{\partial z} = -\frac{i\alpha}{z}A + \frac{\beta_2}{2}\frac{\partial^2 A}{\partial T^2} - \gamma|A|^2 A \tag{4.4}$$

where A is the slowly varying pulse envelope. The first term on the right hand side of this equation describes loss; the second dispersive effects and the third nonlinearity. It can be seen that the NLSE can be seen to be a combination of the nonlinear phase-shift equation and the dispersive wave equation discussed.

Solutions to this equation can be found by using the inverse scattering method [2], but the more common methodology is the split-step Fourier method [2, 115, 116]. In this case, the NLSE is treated as two separate equations, a dispersive equation and a nonlinear equation. These are solved separately over a small time step compared to both the nonlinear and dispersive lengths of the waveguide.

4.2.3 Modulation Instability

Modulation instability (MI) manifests itself as a reinforcement of small deviations of the waveform by the interplay of nonlinear and dispersive effects. This is observed through the generation of spectral side-bands in the frequency domain, akin to degenerate four-wave-mixing that is phase matched by SPM through the nonlinear phase factor, γP. For a full explanation of the relationship between four-wave-mixing and modulation instability in the frequency domain, see reference [2]. Modulation instability can also be thought of in the time domain, where it manifests itself as the collapse of a CW or quasi-CW waveform into a

chain of pulses. For isolated SOI waveguides MI has been both predicted theoretically [117] and observed experimentally [118].

To analytically predict modulation instability we start by taking the steady state solution to the non-linear Schrödinger equation (NLSE), introduced in the preceding section, and adding a small perturbation. In the steady state, we can assume that the amplitude is independent of time at the input end of the waveguide and remains as such during propagation. In this case, the steady state solution is:

$$A(z,T) = \sqrt{P_0}e^{\gamma P_0 z} = \sqrt{P_0}e^{\phi_{NL}} \tag{4.5}$$

where ϕ_{NL} is the non-linear phase shift induced by self-phase modulation acquired during pulse propagation. The implication of this solution is that this power-dependent phase shift is the only modification to the pulse. Adding a small perturbation, $a(z,T)$ to the solution and substituting into equation 4.4 yields

$$\frac{\partial a}{\partial z} + i\beta_2 \frac{\partial^2 a}{\partial T^2} = \gamma P_0 \left(a + a^*\right) \tag{4.6}$$

where the presence of the conjugate of the perturbation denotes coupling between positive and negative components of frequency. The solution yields the following dispersion relation for the wavenumber, K, and frequency, Ω, such that

$$K = \pm\frac{1}{2}|\beta_2\Omega| \left(\Omega^2 + \mathrm{sgn}\left(\beta_2\right)\Omega_c^2\right)^{1/2} \tag{4.7}$$

where $\mathrm{sgn}\left(\beta_2\right)$ denotes whether dispersion is normal or anomalous, and Ω_c is given by the following

$$\Omega_c = \frac{4\gamma P_0}{|\beta_2|}. \tag{4.8}$$

Considering the above analysis, there are two important points concerning modulation instability. Firstly, the signature of MI is the appearance of spectral side-bands at frequencies $\omega_0 + \Omega$ and $\omega_0 - \Omega$. Secondly, the steady-state solution of the NLSE is immune to the effects of small perturbations only in the normal dispersion regime only ($sgn\,(\beta_2) = +1$). In the presence of anomalous dispersion the small perturbation grows exponentially and causes the splitting of a CW beam into a pulse train.

It is possible to define a growth rate, g, of the perturbation defined as the imaginary part of the expression K. It is possible to convert from amplitude gain to power gain by including a factor of 2 such that, $g(\Omega) = 2\Im(K) = 2\mathbf{Im}(K)$. This yields

$$g(\Omega) = |\beta_2 \Omega| \sqrt{\Omega_c^2 - \Omega^2} \tag{4.9}$$

This equation describes maximal gain at two frequencies, Ω_{SL}, and denotes the frequency at which the two spectral side lobes appear (fig. 4-1).

$$\Omega_{SL} = \pm \frac{\Omega_c}{\sqrt{2}} = \pm \left(\frac{2\gamma P_0}{|\beta_2|} \right)^{1/2} \tag{4.10}$$

In the above discussion, it has been noted that we have truncated this analysis to the presence of second-order dispersion only. In the presence of higher order dispersion, it is typical to see an extra pair of modulation instability peaks generated much further away from the pump [16, 119, 120].

4.3 Literature Review

As discussed above, modulation instability (MI) is a degenerate case of four wave mixing (FWM). Both MI and FWM have been studied extensively in other optical media, such as optical fibres, but until recently the application of this nonlinear phenomenon in silicon waveguides has been neglected. Some of the

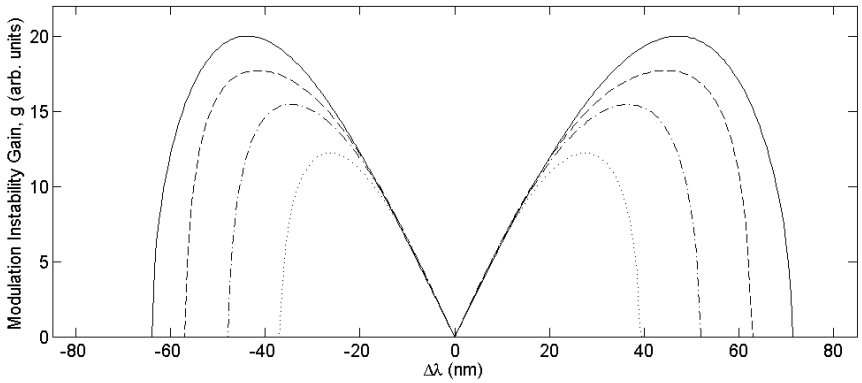

Figure 4-1: Plot showing the standard shape of modulation instability peaks as the power is increased from low (dashed) to high (solid) in the absence of higher-order dispersion.

recent academic literature that was instrumental in shaping this work is reviewed below.

In 2005, NIT Microsystems Integration Laboratories published the report of experimental observations of four wave mixing in silicon nano-wires on the silicon-on-insulator platform [121]. In this work, the authors were concerned with the effects of crosstalk on optical components in telecommunications networks. Their work considers a single silicon wire fabricated on an SOI wafer. The wire is 400 nm wide and 200 nm thick, with spot-size converters at either end [122]. In their work they use an EDFA to amplify pump light at a frequency of 1546.9 nm to a power of 7 dBm. This was coupled into the spot-size converters along with a weaker idler signal at 1547.7 nm. Their results show clear side-band generation in the output spectrum (fig. 4-2 (a)), that they determine is due to FWM. This hypothesis is further enhanced by the power dependence of the conversion efficiency that is approximately 2, a characteristic of FWM conversion [2]. Also of interest are the temporal measurements that show a decrease in intensity of the output signal over time (fig.4-2 (b)). The understanding of the authors is that this relates directly to free-carrier absorption generated by TPA.

The discussion presented in the paper deals more with the technological impact of using silicon waveguides in optical communications systems. On a more fundamental level they briefly attend to the influence of SPM and XPM on their results, although in no great detail. Another consideration not discussed at all is

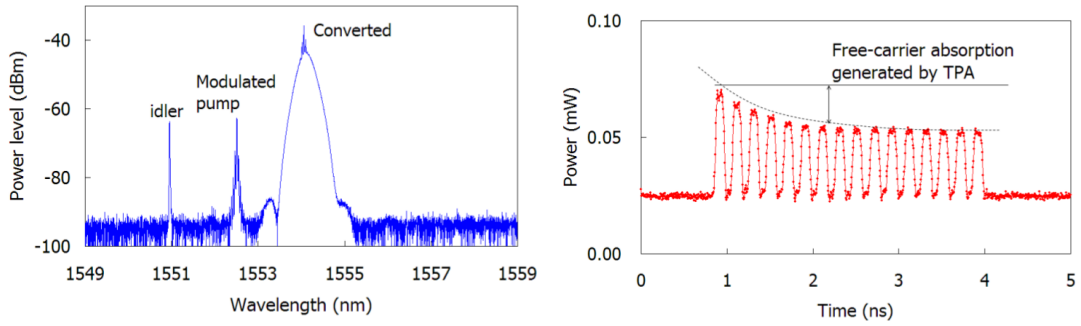

(a) (b)

Figure 4-2: (a) Figure showing output spectra from a pump and idler being input into a 5.8 cm long silicon waveguide. The generated wavelength is centred at 1554.12 nm. (b) The output waveform for 100 ps pulse trains. A clear decrease in amplitude can be seen. This was attributed to free-carrier absorption due to TPA. Reprinted from [121].

the effect of the spot-size converters on any nonlinearity, or the presence of the cladding layers. This may be unimportant in further analysis, due to the relative nonlinearities of both cladding materials concerned but the solution is non trivial.

Whilst the telecommunications industry are interested directly in silicon photonic wires, some research institutions have published research on FWM and MI that is more concerned with fundamental physical understanding. Two of the more published groups in non-linear optics in silicon are Columbia University and Cornell University. Both have published on modulation instability in single silicon photonic wires.

In 2006, researchers at Columbia University published a theoretical observation of MI in silicon waveguides of only a few millimetres in length, achieving three orders of magnitude more gain when compared to optical fibres [117]. The modulation instability that they demonstrate in the paper can be optically tuned unlike the phenomena in previous works. Their gain reaches a maximum when both waves experience anomalous GVD (denoted case B). They also consider the case where one of the input waves experiences normal GVD whilst the other experiences anomalous GVD (denoted case A).

The silicon wires that are used here have a height of 220 nm and a width of 360 nm, not dissimilar to the work by Fukuda [121]. These dimensions are chosen

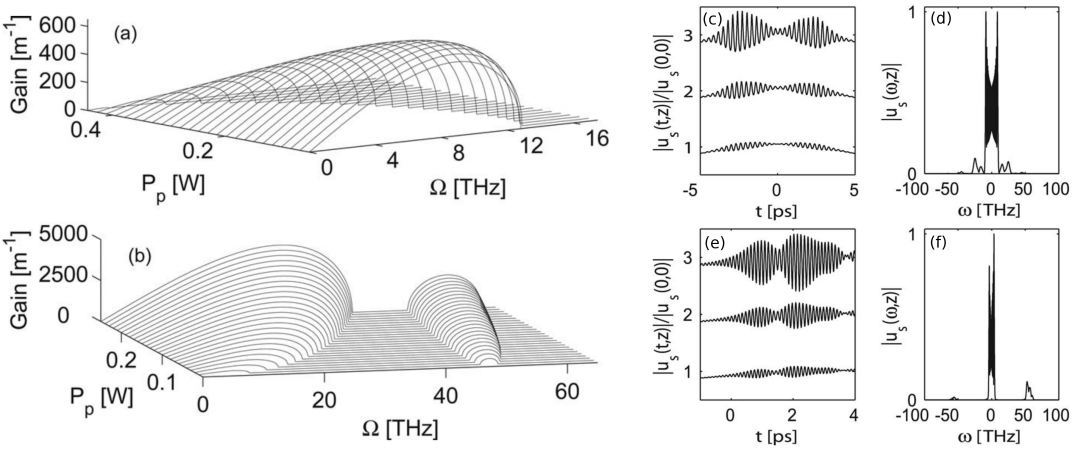

Figure 4-3: Calculated MI gain spectra for cases A (a) and B (b). The powers of the signal wave are 50 mW and 10 mW in case A and B respectively. Temporal and spectral output for an incident Gaussian pulse are shown for case A ((c) and (d)) and case B ((e) and (f)). The temporal signals, (c) and (e), are at positions 19.5, 20 and 20.5 mm from bottom to top with the peaks vertically offset by 1 for clarity. Reprinted from [117].

to give a zero dispersion wavelength of 1550 nm. The steady-state gain spectra in both case A and B, as a function of pump power and detuning frequency are shown in figure 4-3. It can clearly be seen that although the power is smaller in case B a larger MI gain is observed when both waves are in the anomalous GVD regime. This initial analysis included intrinsic and free carrier losses, and the associated change in refractive index due to the presence of the free carriers, but there appears to be no consideration of multi-photon absorption. They continued this analysis by numerically launching a 10 ps Gaussian pulse, with a peak power on the order of 100 mW, into the waveguides (fig. 4-3). Their results showed a significant temporal modulation, a manifestation of the onset of MI, for both case A and case B. However there were also differences in the two spectra. In case A, when one of the waves experiences normal GVD, the MI side-band growth only happens after the central part of the spectrum has broadened due to self- and cross- phase modulations. Contrary to this, in case B, the side-bands develop well away from the central part of the spectrum and develop from the noise, without the need for a seed laser. This has been observed experimentally elsewhere [123].

As mentioned above, experimental observation of FWM has also received at-

tention. Cornell University have published many works showing experimental observation of these effects [123–125]. In the first work [123], the focus is transferring highly developed active optical components from the optical fibre platform to the SOI platform. They extend the work discussed previously by Fukuda, by increasing bandwidth and conversion efficiency through proper phase-matching. They use waveguides of different shapes and sizes to control the GVD in the desired manner: 300 nm x 600 nm, 200 nm x 400 nm and 1.0 μm x 1.5 μm. GVD and gain were calculated numerically, and compared to experimental results. Experimentally, they use an optical parametric oscillator centred at 1550 nm as a source for both the pump and signal pulses. These are then filtered to 1 nm and 1.5 nm FWHM respectively, yielding temporal durations of 3.5 ps and 2.4 ps respectively. The pump pulse is passed through an EDFA, but no mention of the total gain is discussed. Finally, both pulses are combined using a wavelength division multiplexer and coupled to the silicon waveguide using both a tapered lensed fibre and an inverse silicon taper.

The outcome of their observations is that they observe smaller gain than predicted due to the combined effects of nonlinear absorption, free carrier absorption and pump depletion. They state that the results show that these processes are dominant at low pump powers. They also go on to say that the limit of their source bandwidth impairs their measurement of the true gain bandwidth and larger values are expected.

The second paper from this group goes into more depth about their results [124]. In this work, their 3 dB bandwidth is 150 nm, with peak conversion efficiency of -9.6 dB. Here they use similar experimental methods but expand on their results, citing that the phase-matching bandwidth is not only dependent on the GVD but also the fourth-order dispersion. Using this higher-order dispersion phase-matching they can extend their previous results to span the C-band of the telecommunications network with minimal signal degradation. In the first paper, discussed above, the focus appeared more on peak efficiency, but here they have obviously extended their understanding of FWM within silicon nano-wires to more actively understand the bandwidth of the gain spectra (fig. 4-4).

More recently, further bandwidth gains have been made by this group [125]. In this work they take care to optimise their system to push the first zero-GVD point into the C-band. In doing this they reduce the fourth-order dispersion by

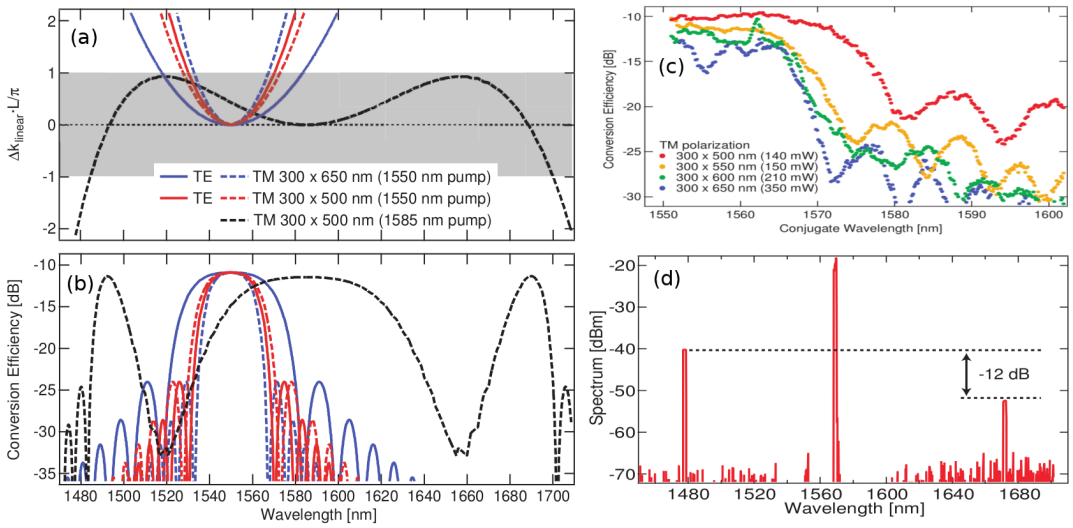

Figure 4-4: The phase-mismatch after 1 cm of propagation (a) and the subsequent conversion efficiency for 100 mW pump power for the three waveguides considered in [124]. All curves assume a pump of 1550 nm except the black curve which has a pump at 1585 nm. In the presence of fourth-order dispersion a second phase matching point appears detuned from the pump. (c) Experimentally measured conversion efficiency for the TM polarisation mode pumped at 1550 nm.The TM mode for the smallest waveguide has the lowest GVD and hence the largest conversion bandwidth. (d) Output spectra showing wavelength conversion over four telecommunications bands, from 1477 nm to 1672 nm with -12 dB efficiency. Reprinted from [124].

two orders of magnitude. Now the waveguides are 270 nm x 700 nm but sit on a 30 nm thick silicon slab. The result is that their gain spectra bandwidth is greater than 840 nm, the limit of the detection equipment. The change in bandwidth is not only due to the drastic reduction in fourth-order dispersion but also due to a reduction in free-carrier absorption. This is achieved by the presence of the silicon slab under the waveguide. Whilst the mode area of the composite geometry is not drastically increased by the presence of the slab, there is a larger silicon cross section and the authors argue that this reduces the presence of free carriers in the areas of high optical intensity.

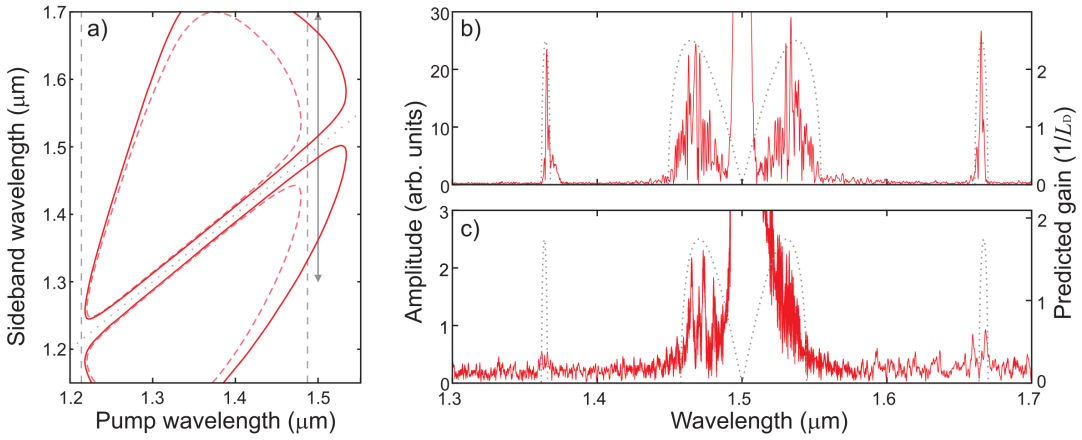

Figure 4-5: (a) Predicted wavelengths of MI side-bands versus pump wavelength. The grey arrow denotes a 1550 nm pump, with the dashed (solid) lines corresponding to the peak gain for the symmetric (antisymmetric) supermodes. As can be seen, MI does not occurs in the symmetric supermode using a 1550 nm pump due to it experiencing normal dispersion at this wavelength. (b) and (c) show output spectra at a distance of 1.93 mm through the array when pumped with a rectangular 10 ps pulse with power 10 P_0. (c) has free carrier effects included and as such the gain peaks that are far detuned from the pump do not appear. Reprinted from [89].

4.3.1 Waveguide arrays

In the preceding literature review we have concentrated solely on single silicon waveguides. However, recent theoretical work on arrays of silicon wires has been published by researchers at the University of Bath [89]. The main concepts in this work are the shifting of GVD induced by the presence of coupling. This work, and the experimental confirmation completed as part of this thesis, were discussed in the preceding chapter. The theoretical paper also discusses two two nonlinear processes, namely MI and soliton effects. The experimental work outlined in the rest of this chapter is based upon the analysis of MI presented in the aforementioned work.

The waveguides considered in the work by Benton *et al* [89] are 220 nm high and 330 nm wide with an edge-to-edge separation of 330 nm. For the out-of-phase mode, this yields strongly dispersive coupling in the proximity of a 1550 nm pump pulse. The MI side-band growth rate, and output pulses after a 10 ps rectangular

pulse has propagated through 1.93 mm of waveguide, can be seen in figure 4-5. The 10 ps pulses were chosen to enable propagation in the quasi-continuous-wave regime, whilst remaining experimentally achievable. As with the work by Foster *et al*, the presence of fourth order dispersion yields a prediction of frequency generation that is far detuned from the pump [124]. Unlike authors of other work, Benton *et al* believe that without a seed laser the presence of FCA will overwhelm any MI gain and hamper detection of spectral side-bands. The suggestion is that techniques to sweep free carriers away from the waveguide be employed to enable observation of the spectral side-bands without a seed. Subsequent discussions with the authors of this work suggested that the calculations had been done with an over conservative estimate of the absorption due to FCA and that MI gain could be observed without a seed laser.

4.4 Experimental Observation of MI in Silicon Photonic Wire Arrays

The experimental work outlined here tries to follow that of the theoretical work on MI in waveguide arrays [89]. To that end, the initial consideration is generation of a suitable pump pulse. My aim was to generate a Gaussian, or sech-squared type pulse of approximately the same FWHM as the rectangular pump as described in the literature. As with the numerical work, I am not going to use an idler pulse as a seed, but rather let the MI gain generate the appropriate signal from the background noise.

4.4.1 Waveguide Selection

In this work we start by considering a single waveguide of 220 nm x 380 nm. The zero dispersion wavelength of this waveguide is approximately 1600 nm, as shown in figure 4-6 (a). I measured the dispersive properties of this waveguide utilising the same method as used in Section 3 of this thesis. The results compare favourably with my numerical simulations using the Comsol Multiphysics software (shown by the blue dashed line in figure 4-6 (a)). Using the theoretical equations, knowledge of the dispersive properties is all that is required to calculate the modulation instability gain (fig. 4-6 (b)). The power was fixed and the

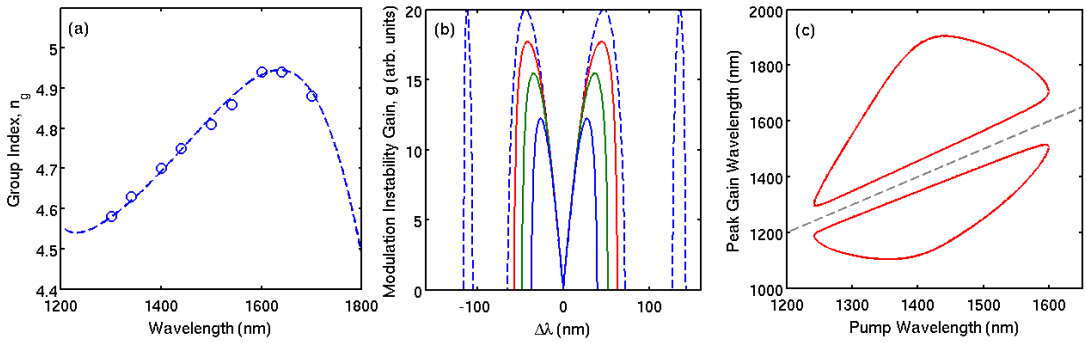

Figure 4-6: (a) Plot showing the experimental (blue circles) and numerically modelled (dashed line) group index for a 220 nm x 380 nm silicon waveguide. (b) Modulation instability gain in the wire defined in (a) pumped at a wavelength of 1231 nm (blue solid), 1234 nm (green solid), 1236 (red solid) and 1260 nm (blue dashed). The increase in the gain is directly related to the value of β_2 as the power is fixed at $P = 10P_0$. As the higher-order dispersion begins to take effect, the gain peak splits and is shifted from the central wavelength. The peak values of the gain spectra are plotted as a function of the input wavelength, showing the clear presence of two extremal peaks at far detuned wavelengths (c).

peak gain is only modified by the change in the dispersion characteristics. It can be seen that this waveguide has non-trivial higher-order dispersion, as discussed in many previous works, and the modelling shows the presence of the modulation instability side-bands far detuned from the pump. This can be seen better in the peak gain map (fig. 4-6 (c)). Here, I have plotted the peak values of the gain spectrum as a function of the pump wavelength.

The main goal of this experimental research is to consider modulation instability in waveguide arrays. The coupling-induced dispersion of the arrays will undoubtedly mean that a different geometry will be required in order to set the zero-dispersion wavelength of either the symmetric or anti-symmetric modes to the spectral region around 1600 nm. This coupling-induced dispersion also increases the complexity of the observed physics. To eliminate this complexity, I decided to consider only a single 380 nm single wide waveguide in the first instance. The geometry change yields not only a change in zero GVD wavelength but also a substantial GVD at the pump wavelength, approximately 2500 ps/nm/km. This simplification to the geometry allowed me to perfect the experimental configuration prior to evaluation of the array structures.

4.4.2 Pulse Generation

Generation of suitable pulses to stimulate MI growth, is a two stage process. The first stage uses a commercial ultra-fast laser system, a Coherent RegA9000 regenerative amplifier seeded by a Coherent Mira Oscillator, as a source for a parametric amplifier. The Mira oscillator is a titanium-sapphire laser that outputs a 76 MHz pulse train of 100 mW average power. The pulses within this pulse train are centred at 800 nm and have a duration of the order of 0.1 ps. The high repetition rate means individual pulses have relatively low energy and peak power. These pulses are injected into the Coherent RegA 9000 regenerative amplifier. This again uses titanium-sapphire as the gain medium but with a higher pump power creating population inversion. A combination of a Q-switch and pulse-picker dump this energy into the seed pulse and out of the cavity. The output pulse train now has an average power of approximately 1.1 W and a 250 kHz repetition rate.

The output pulses are input into an optical parametric amplifier (OPA). An optical parametric amplifier makes use of materials that lack inversion symmetry. In the non degenerate case, there is an interaction between three distinct frequencies of light: a pump wave, ω_p, a signal wave, ω_s and an idler wave, ω_i. Conservation of energy tells us that the relation $\omega_p = \omega_s + \omega_i$. In the plane-wave limit this leads to interactions such that the rate of change of the amplitude of each component can be described by the amplitude of the other two and the phase mismatch

$$\frac{\partial}{\partial z} A_s = \kappa A_p A_i * exp\left(-iz\Delta k\right) \tag{4.11}$$

where z is the propagation direction, κ is a coupling constant, A denotes the wave amplitude for a given component and Δk is the phase mismatch, given by $\Delta k = k_p - (k_i + k_s)$. The Coherent OPA splits the input pulse train from the RegA into a 75:25 split. The larger of the two amplitudes is then directed into the nonlinear crystal. In this OPA, Coherent use a barium-borate (BBO) crystal. The smaller amplitude wave is passed through a thin sapphire crystal to generate a broadband supercontinuum. The supercontinuum is then fed into the BBO crystal going through a first pass delay. A second pass delay controls the

co-incidence of the pump and supercontinuum on a second pass through the BBO crystal. Wavelength selection is done through angular rotation of the BBO crystal with respect to the pump and supercontinuum beams. Maximising amplification then takes careful control of the two pass delay lengths. The output pulses of the OPA were centred at 1537 nm, with a repetition rate of 250 kHz, an average power of 30 mW and a duration of 100 fs.

4.4.3 Bandwidth Selection

In order to spectrally filter the pulses from the OPA, I used a silica transmission grating from Ibsen Photonics. The grating has 996 lines/mm and the angular dispersion can be calculated by

$$\frac{\partial \theta_D}{\partial \lambda} = \frac{\sin(\theta_i) - \sin(\theta_D)}{\lambda \cos(\theta_D)}. \tag{4.12}$$

For a central wavelength of 1550 nm, incident on the grating in the Littrow configuration (at an angle of 49.6°), this yields a dispersion of 0.08 $^\circ/nm$. The transmission grating is placed in the output of the OPA and a 0.65 NA aspherical objective, 30 cm away from the grating, couples the collected light into the input of an EDFA. It would be possible to measure the temporal width of the pulses at this point, but the dispersive properties of the EDFAs may alter the temporal characteristics of the pulses prior to insertion into the silicon waveguides.

Using the above equations yields a spectral width of 0.5 nm. Making the assumption that the pulse is Gaussian, transform-limited and chirp-free, we can calculate the temporal duration to be 6.7 ps.

4.4.4 EDFA

Post spectral filtering using the transmission grating, I chose to use two erbium doped fibre amplifiers (EDFAs) to provide the necessary amplification of the pulses.

An EDFA is an all-fibre optical amplifier using a length of optical fibre with an erbium-doped core as the gain medium. Fibre Amplifiers are commonly used to overcome transmission losses in fibre-optic communication systems but also

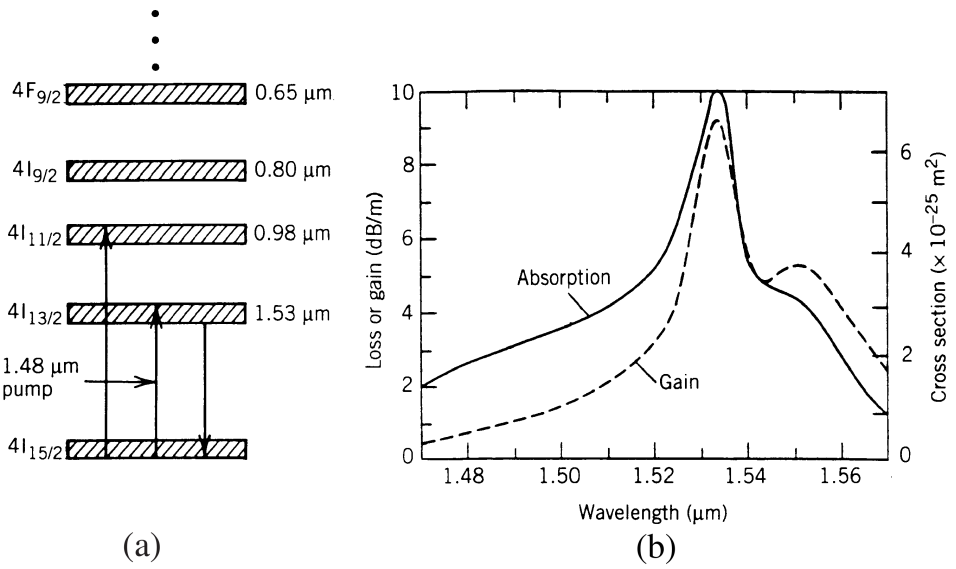

Figure 4-7: (a) Energy Levels of erbium ions in silica fibres. (b) Absorption and gain spectra of an erbium doped fibre [126]. Both reprinted from [127].

provide a gain mechanism for pulse amplification at higher powers. Erbium, in the form of Er^{3+} ions are a commonly used rare earth material for providing gain due to the emission wavelengths associated with its excited states. The energy levels of Erbium and the relative absorption and gain spectra are shown in figure 4-7. As can be seen from the energy levels, efficient pumping is possible using lasers near 980 nm and 1480 nm wavelengths. A non optical mechanism, such as a phonon, can then reduce the ion to the lower edge of its $4l_{13/2}$ state. From here, optical emission at 1.53 nm is achieved, within the C band of the telecommunications spectrum.

4.4.5 Experimental Configuration

As can be seen in figure 4-8, we use two EDFAs to achieve the required amplification. The first uses a highly doped Erbium fibre (Thorlabs Er110-4/125) as the gain medium. This fibre is spliced to a length of Nufern 4 μm core dispersion compensation fibre, to compensate the dispersive properties of the Erbium fibre.

Splicing was achieved using an arc-fusion splicer. Initially both fibres had to be stripped, and their end faces cleaved as close to a perpendicular as possible.

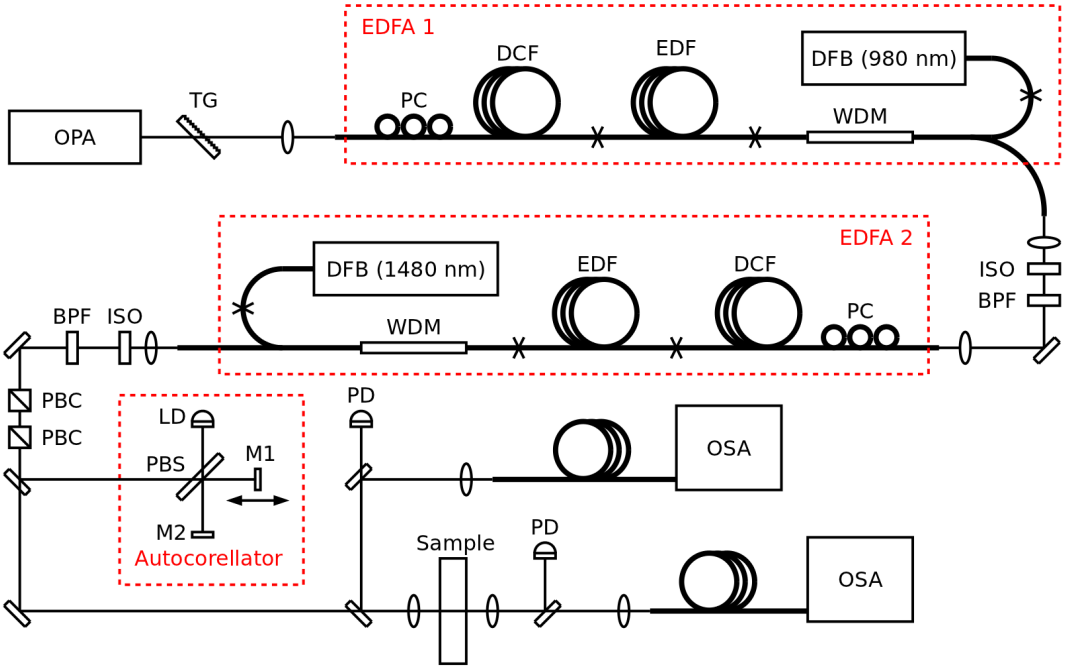

Figure 4-8: Schematic of the experimental configuration of the EDFAs and subsequent insertion and collection optics. The OPA pulse is spectrally filtered by a silica transmission grating (TG) before being inserted into the first of two EDFAs. Both EDFAs comprise a length of dispersion compensation fibre (DCF), erbium doped fibre (EDF), a wavelength multiplexer (WDM) and a distributed feedback laser (DFB). Isolators (ISO) and bandpass filters (BPF) reduce ASE and feedback between the EDFAs. Various pick-offs are in place to measure the temporal and spectral properties of the input pulse prior to entering the sample, via an autocorrelator and OSA respectively. The OSA is also used for the output spectra.

The end places are then placed within a few microns of each other. An electric arc, an electric breakdown that produces an ongoing plasma discharge, is used to super heat both ends of the fibre simultaneously. Both surfaces melt, whereby they are pushed together. As the fibres cool, they fuse together. This whole process is very quick and as such there is negligible diffusion of the dopants that make up the core region. Losses of the order of 0.01 dB were expected but not formally measured. Finally, a protective layer was put over the splice to protect the exposed fibre from damage.

With the two main fibres connected, a free space coupling system was em-

ployed to assess the length of each of the pieces. Finally lengths of 60 cm and 200 cm were chosen for the EDF and dispersion compensating fibre respectively. This was based on the characterisation of the output power, gain and amplified spontaneous emission (ASE). Once cut to the desired length, the Erbium fibre was spliced to the single tail side of an all-fibre wavelength division multiplexer (WDM). This device uses a fused biconical-taper to co-propagate the light from two separate fibres into a single output [128]. The WDM used was specific to 980 nm and 1550 nm with a 20 nm bandwidth on each fibre. In the orientation used, the single output was spliced to the Erbium-doped fibre and the 980 nm input was spliced to a 980 nm distributed-feedback diode laser.

The set-up was positioned in a backwards pumping regime as the power of the DFB diode laser put us in the saturation regime. In the backwards-pumping configuration there is lower ASE and thus better power conversion [129]. A fibre polariser, comprising of two quarter-wave plates sandwiching a half-wave plate was placed over the fibre. This uses stress-induced birefringence, generated from coiling the fibres around a spool, to create the three fractional wave plates. The spools are then axially rotated with respect to one another to achieve the desired polarisation state.

After the output from the fibre coupler, we used a 20x aspheric objective lens to couple to some free space optics. The first was an isolator to prevent the back reflecting pump from the second EDFA from entering the first; followed by a bandpass filter, to remove some ASE. Another 20x aspheric lens was used to couple into the second EDFA. An isolator was not required between the OPA and the first fibre amplifier as the backward propagating pump was not transmitted back along the light path by the transmission grating.

The second EDFA also used Nufern 4 μm core fibre for dispersion compensation but used some Thorlabs Er16-8/125 fibre as the gain medium. This fibre has a larger core and a lower concentration of erbium ions. This larger core area avoids non-linearity for the higher signal powers. A 4 m length of this fibre was used to maximise the power, whilst keeping the noise and nonlinearity to an acceptable level. This fibre was pumped with a 1480 nm DFB diode laser. The reason for pumping in this regime is to maximise conversion efficiency.

After the second EDFA (fig. 4-8) I used a similar isolator and bandpass configuration to minimise ASE into the device. I also used two rotatable beam-

splitter cubes (PBS) to control the polarisation and power entering the waveguide. At this point, the input pulses were temporally characterised prior to insertion into the waveguide. This is discussed in the section immediately following this. Insertion into and emission from the sample waveguide was controlled by a 60x aspheric lens (using a similar alignment procedure as discussed in Chapter 3), and the output was analysed on an optical spectrum analyser.

4.4.6 Autocorrelation

Temporal characterisation of the input pulses was achieved using interferometric autocorrelation. The basic premise of an autocorrelator is that a beam splitter splits a pulse into two copies. These are then overlapped on a nonlinear medium, where they interact if they are temporally superimposed. The second harmonic recording is proportional to

$$I_t = \int \left| \left(\vec{E}\,(t)\, e^{i(\omega t+\phi)} + \vec{E}\,(t-\tau)\, e^{i(\omega(t-\tau)+\phi)} \right)^2 \right|^2 dt \tag{4.13}$$

where $\vec{E}$ is the electric field from each arm [108, 130]. At zero delay the interferometric signal is a coherent superposition of the relevant fields, yielding

$$I_t(0) = 2^4 \int \vec{E}^4(t) dt. \tag{4.14}$$

Far from the coherent superposition, the interference fringes lose their coherence, and the value of the interferometric autocorrelation is equivalent to an intensity autocorrelation.

The upper and lower envelopes of the interferometric signal are given by

$$\int |\vec{E}(t) \pm \vec{E}(t-\tau)|^4 dt \tag{4.15}$$

where the negative denotes the lower envelope (fig. 4-9 (a)). The autocorrelation can easily tell you about the pulse characteristics. Not only is it possible

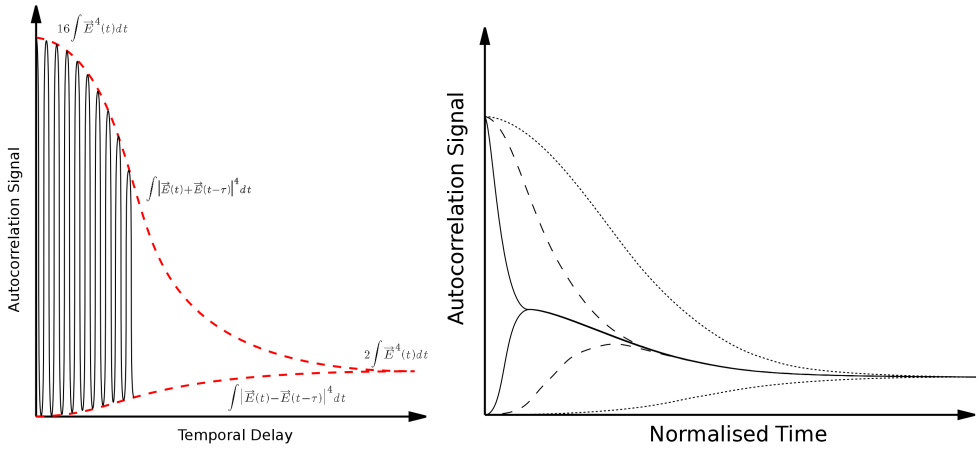

(a) (b)

Figure 4-9: (a) Cartoon of an interferometric autocorrelation. The interference fringes can be seen, with the envelope added for clarity (red dashed lines). Also shown are the equations for the two envelopes along with the equation defining the maxima of the upper envelope, and the background signal level. (b) Locus of the upper and lower envelopes of the interferometric and intensity autocorrelations given by pulses with linear chirp. The level of chirp increases from the dotted to solid lines. Reprinted from [108].

to translate from your delay time to real time, to calculate the pulse duration, but it is also possible to tell if the pulse has any chirp, observed by the presence of "wings" at either end of the interferogram. In a chirped pulse, the phase of the frequency components with is not constant across the pulse. A linear phase shift between different frequency components, translates the temporal position of that component in the pulse train. Pulses with the low-frequency components of the pulse at the front (back) are known as positively (negatively) chirped. The mathematical explanation of the interferometric shape of a linearly chirped pulse is explained in reference [108], but is shown graphically in figure 4-9 (b). As can be seen, with a chirped pulse the measured full width half maximum of a chirped interferogram does not reflect the temporal duration of the pulse accurately.

In my set up I use interferometric autocorrelation in a Michelson arrangement (fig. 4-8). The mirror, M2, defining one of the arms of the interferometer is mounted on the top of a translation stage. This is used to equalise the optical path length in both arms. The second mirror, M1, is mounted on an oscillating stage, made from an audio speaker. This is driven by a function generator to

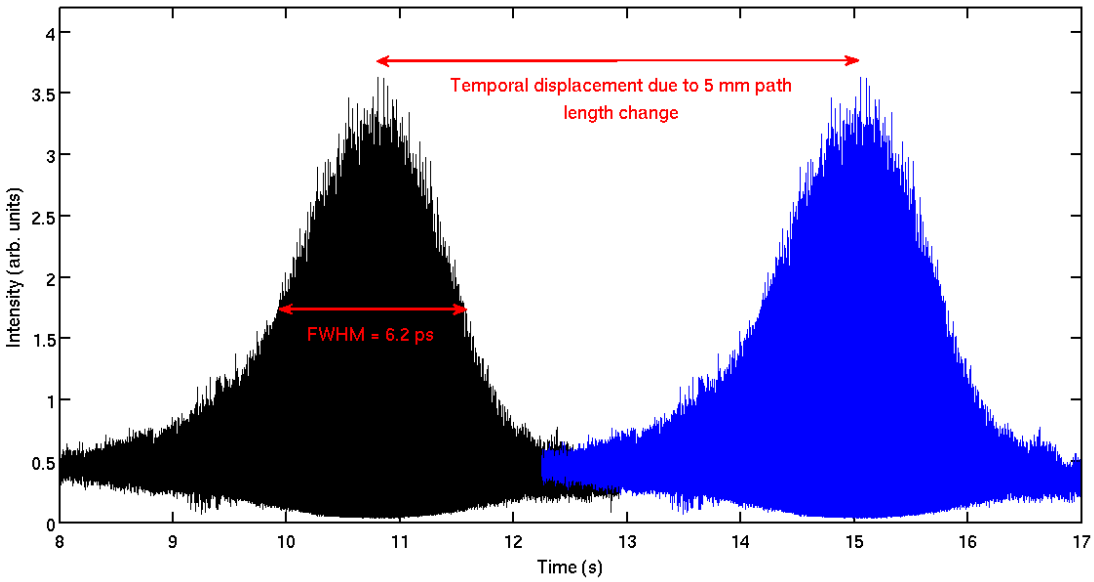

Figure 4-10: Plot of the autocorrelation trace of the input pulse into the silicon waveguide. The autocorrelation was taken using a laser diode and a Michelson interferometer geometry. The second peak represents the temporal shift of the pulse given a change in the path length of 5 mm.

create the temporal delay required, τ. I took two sets of measurements of the pulse. Each was the same except that the delay path in the static arm was changed by 5 mm, with the mirror moving half that distance. From this I created a conversion factor to real time. The distance between the two traces is 0.42 s. Equating this to a travel time for light gives a conversion factor of $\sim$ 2.55 x 10^{-11}. The pulse width, using this conversion equates to 6.2 ps (fig. 4-10). The autocorrelation also shows us that there are no wings, and the ratio of the peak intensity and incoherent intensity autocorrelation is almost the ideal value of 8:1.

Time-Bandwidth Product

As an important aside to the above section, pulse characterisation depends heavily on the relative phase of the frequencies that comprise the pulse. An un-chirped pulse happens when the phase of all of the frequencies is constant at the centre of the pulse. In this case the pulse can be represented by an envelope and single monochromatic carrier frequency.

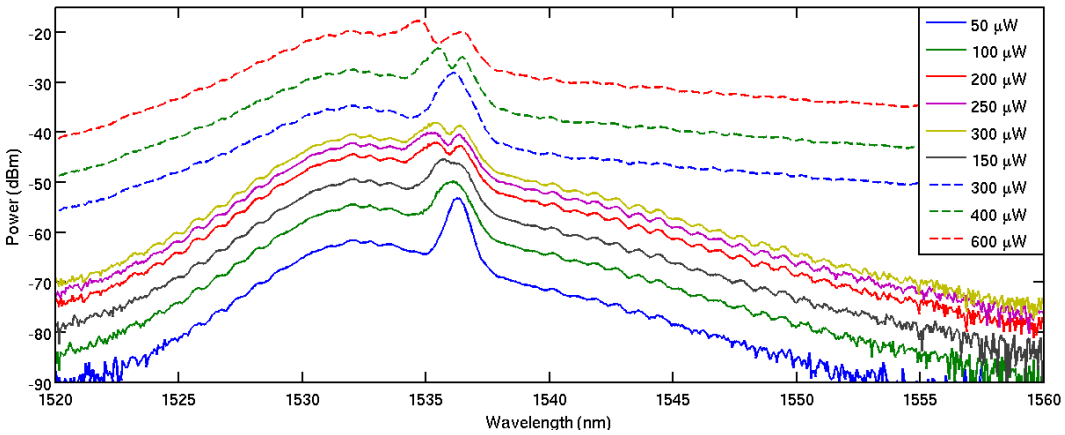

Figure 4-11: Spectra output from a single 380 nm x 220 nm waveguide, when pumped with pulses of average power as given by the legend.

A quantity, referred to as the time-bandwidth product can be calculated such that, for a Gaussian shaped pulse,

$$t_{FWHM}\nu_{FWHM} = \frac{2ln(1/2)}{\pi} \approx 0.44 \tag{4.16}$$

where ν_{FWHM} and t_{FWHM} are the full-width-half-maxima of the spectrum and temporal duration of the electric field. This product sets the minimum pulse duration that a Gaussian shaped spectrum can generate. Different pulse shapes have different time-bandwidth products, notably a sech-squared pulse has a time-bandwidth product of 0.315. Pulses that have the lowest possible time bandwidth product are referred to as time-bandwidth limited.

If a pulse is not time-bandwidth limited, and has a longer duration, it is most likely due to the presence of chirp, as discussed previously. The pulses we produced show no signs of chirp. The temporal measured duration of 6.2 ps and the measured wavelength bandwidth of 0.15 nm yield a time-bandwidth product of 0.5. If my assumption about the Gaussian pulse shape is correct, this puts the pulse near the time-bandwidth limit.

4.4.7 Results and Analysis

Results were collected using the method above, for different incident pump powers, controlled by the polarising beam splitter configuration prior to insertion into the waveguide (fig. 4-8). The powers input into the waveguide were 150 mW to 300 mW in steps of 50 mW. The power was further increased by removal of the second bandpass filter. Whilst the primary increase in power was away from the peak, matching the high attenuation region of the filter, there was also gain within the peak. In this configuration, the total input powers considered were 300 mW, 400 mW and 600 mW. This increased the total power across the entire spectrum, but also increased the peak power due to the non-zero attenuation in the centre of the bandgap. It can be seen, from the output spectra (fig. 4-11), that the majority of the pulse energy resides within the peak at 1537 nm. Previous analysis shows that the pulse is approximately Gaussian. The peak power, under these conditions, can be approximated as

$$P_{pk} \approx \frac{E_p}{\tau_p} = \frac{P_{avg}}{\tau_p r_{rep}} \tag{4.17}$$

where P_{pk} is the peak power, E_p is the pulse energy, P_{avg} is the average power, τ_p is the pulse duration and r_{rep} is the repetition rate of the laser. Given these parameters, the peak pulse energy is 18 W. This compares favourably with the values used in the academic literature where it is the order of $20P_0$. The value of P_0 is calculated from the nonlinear coefficient, γ, and the dispersion length, L_D, such that $P_0 = (L_D\gamma)^{-1}$. It is expected, from the results obtained by other researchers in our laboratories, that the insertion loss is of the order of 10 dB. Given this factor, the peak power inside the waveguide is only of the order of P_0.

The output spectra (fig. 4-11) shows that we observe asymmetrical spectral broadening around the pump wavelength. This is observable both with and without the extra filter. The apparent spectral contraction of the broadening at 300 μW after inserting this filter is due to the lower spectral power density in the peak but larger power present in the wings of the pulse. The pulse appears broader in this case. However, the trend of an asymmetric pulse broadening is still observed. It is unlikely that this pulse broadening is due to MI but looks

more like solitonic behaviour or other nonlinear phenomenon. It is possible that the nonlinear losses, namely TPA and FCA are higher than originally expected. The pulse characteristics are also lower than proposed in the literature and so we could be below the power threshold to observe MI. A seed pulse could be required to help overcome this.

4.5 Subsequent Work

Following the work described above, my colleagues at the University of Bath built upon this work to publish further experiments using a seeded system [131]. Here they use an idler at 1542 nm along with the pump signal at 1532 nm both generated from the optical parametric amplifier, OPA. In order to compensate for the delay in the pump signal induced by the EDFA, the idler signal is passed through a 10 m length of HC-PCF, engineered to provide negligible dispersion at the idler wavelength, and inherently low nonlinearity.

In this work, they use directional couplers of 380 nm width that are separated by 900, 800 and 400 nm distances. With the large separation waveguides, the splitting of the supermodes is negligible and hence MI develops similarly to the case where only a single wire exists as per my original experiments. The 400 nm separated directional coupler has a large shift in GVD due to the coupling-induced GVD, making the zero dispersion wavelength for the symmetric supermode fall between 1500 nm and 1600 nm. The experiments were performed similarly to those described in the previous sub-sections, but with more optimisation of the pulse generation. The input pulses were tuned to be 8.5 ps long, centred at 1530 nm (fig. 4-12 (a) Inset 1).

On top of observing clear wavelength conversion detuned away from the pump wavelength (fig. 4-12 (a) Inset 2), the authors extend this to look at the conversion efficiency as a function of the idler wavelength, and the MI gain as a function of pump power (fig 4-12 (b) and (c) respectively). The conversion efficiency, η, is defined here as the converted idler power divided by the signal power in the output; and the MI Gain, G, as the signal power with the pump switched on divided by that with the pump off; such that:

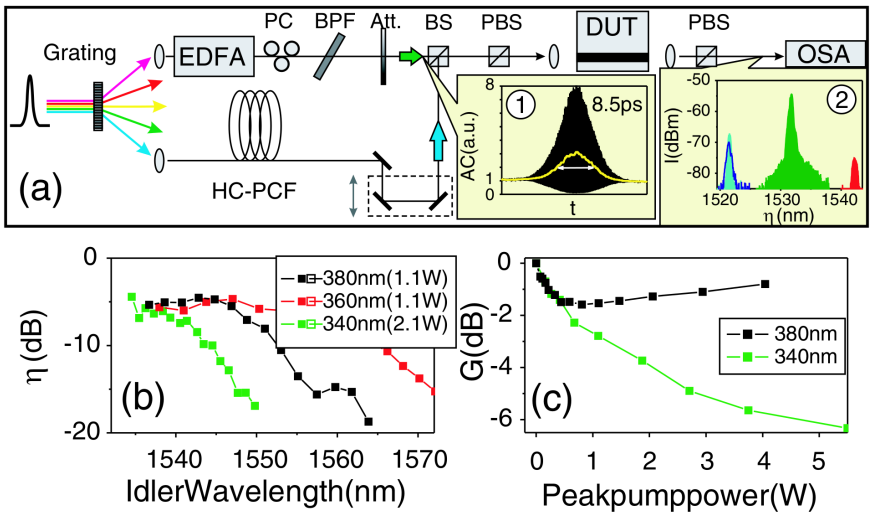

Figure 4-12: (a) Schematic of the experimental set up showing both the auto-correlation of the input pulse (Inset 1) and a typical output spectrum (Inset 2) showing pump (green), signal (blue) and idler (red) components. (b) Measured conversion efficiency spectra of three single-channel waveguides (widths: 380, 360, and 340 nm, respectively) with the pump at 1532 nm. The peak pump power inside the waveguide is shown in the label. (c) MI gain versus peak pump power inside the 380 nm wide (black, $\lambda_{signal} = 1520$ nm) and 340 nm wide (blue, $\lambda_{signal} = 1518$ nm) wires. The peak signal power inside the wires is 0.15 W. Reprinted from [131].

$$\eta = \frac{P^{out}_{idler}}{P^{in}_{signal}} \tag{4.18}$$

$$G = \frac{P^{out}_{signal}|_{\mathbf{pumpon}}}{P^{out}_{signal}|_{\mathbf{pumpoff}}} \tag{4.19}$$

For a single wire, as the waveguide width changes from 340 nm to 380 nm, the GVD at the pump wavelength goes from being normal to being anomalous. The wire width at 360 nm exhibits the broadest MI conversion band and, thus, the expected absolute value of GVD is smallest in this case. In order to determine if the converted spectrum experiences any MI gain, the dependence of the gain parameter, G, on the pump power was measured (fig 4-12 (c)). Their assertion from these results is that the dominant process at the signal wavelength in both wires is the cross-phase modulation induced spectral broadening accompanied by

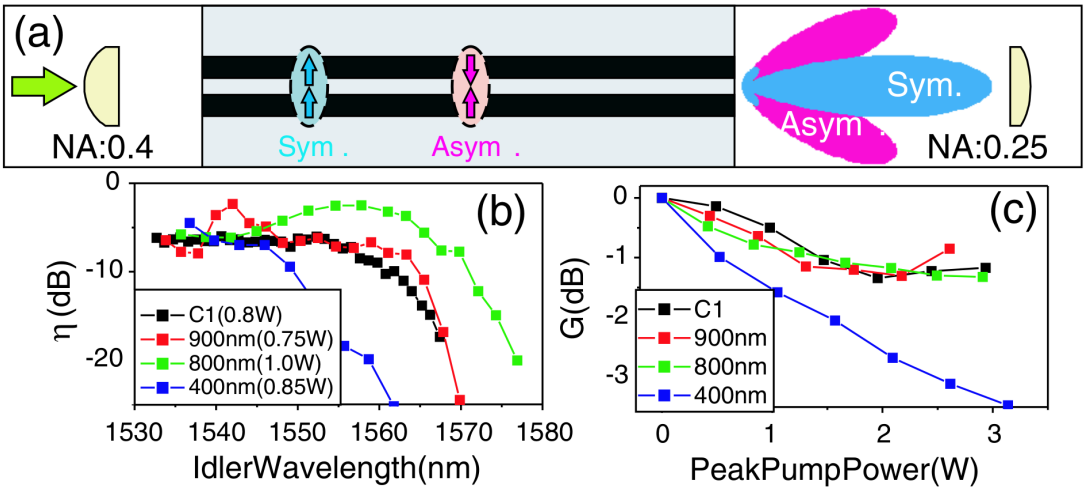

Figure 4-13: (a) Supermode excitation and collection in a directional SOI coupler. The radiation patterns of the symmetric and asymmetric supermodes are also shown. (b) Conversion efficiency versus idler wavelength in the couplers with separation distances 900, 800, and 400 nm. Estimated peak pump powers inside the waveguides are given in the label. (c) MI gain versus peak pump power of the arrays with $\lambda_{pump} = 1530$ nm and $\lambda_{signal} = 1518$ nm.

both TPA and FCA effects. Above moderate power, there is a divergence of the gain behaviour between the two waveguide widths. The rise for the 380 nm width coupler is associated with MI gain counterbalancing all the loss mechanisms. In the 340 nm wire, the rise in MI gain is not observed, noting that the spectral broadening is dominated by cross-phase modulation, not modulation instability gain.

As was discussed in the previous section, the nonlinear absorption could be too high to allow generation of spectral sidebands using the background noise as a seed. For the subsequent experiments completed here, the use of a seed laser provides ample intensity at the peak gain wavelength to observe the nonlinear wavelength conversion effects. If we look at the plot of gain as a function of peak pump power we see that all values are negative and we see a net absorption. These results shows that without a seed, it would not be possible to see the wavelength conversion processes at all; concordant with the results I presented earlier. For the 380 nm waveguide width it is possible to see that the MI gain is beginning to overcome some of the nonlinear losses above 1 W peak power in

the pump laser, however it is not strong enough to completely overcome them and induce positive net gain. Only at this point would an non-seeded experiment show any indication of modulation instability.

Excitation conditions have been carefully monitored (fig. 4-13 (a)) so as to exclude possible instabilities associated with nonlinear cross coupling between supermodes [132]. Conversion efficiency and MI gain for the couplers are shown in figure 4-13 (b) and (c) respectively. For the large separations, the dependencies are similar to the single waveguide cases and the presence of MI-generating parametric gain. For the 400 nm separation, we also observe spectral narrowing and continuous decrease of gain with pump power; unambiguous indication that MI is not present.

4.6 Summary

Work has been presented that shows modulation instability with in silicon waveguide arrays. My initial work on preparing the experimental set-up and obtaining the first set of results with a single wire have been described. In this work, 6.2 ps pulses of 18 W peak power were input into a silicon waveguide in order to observe modulation instability. Although non-linear effects were observed, there is no evidence of modulation instability in this configuration. The work has been continued by colleagues at the University of Bath, including a seed pulse generated from the parametric amplifier used in my experiments. They observe modulation instability and its pronounced dependence on the coupling-induced group-velocity dispersion.

Chapter 5

Silicon Photonic Wires in the Nonlinear Regime: Spatiotemporal Solitons

5.1 Introduction

Like the preceding chapter of this thesis this chapter focuses on nonlinear optics in arrays of silicon photonic wires. In particular here we discuss light bullets, or spatiotemporal solitons. The first section discusses some background theory on spatiotemporal solitons and spectral signatures that can be used to detect them, namely Čerenkov radiation. The following sections will discuss my work towards academic publications on spatiotemporal solitons [133,134]. Finally, I will discuss the extension to this work completed at the University of Bath [135,136] and my contribution to this work.

5.2 Background Theory

5.2.1 Temporal Solitons

In Chapter 1, we discussed how a balance between self-phase modulation and dispersive pulse broadening can result in a solitary wave, or soliton, that does not change during propagation. At the leading edge of the pulse, the refractive index increases with time due to the increase in optical intensity. This gives a

red-shift in the frequencies in this part of the pulse due to the retardation of the temporal oscillation relative to the rest of the pulse. At the trailing edge of the pulse there is a decrease in optical intensity with time. This causes a blue-shift of components of the pulse that exist within the tail.

In the presence of anomalous dispersion the bluer frequencies of light have a higher group velocity than the red frequencies. In the linear regime this would cause pulse broadening. However, for high optical fields, where nonlinear effects occur, the dispersion can be counteracted by nonlinear self-phase modulation.

Temporal solitons can be analysed using the nonlinear Schrödinger equation, as discussed in the preceding chapter. The NLS equation yields a well known soliton solution [2, 22, 114] of the form

$$E(\xi,\tau) = \sqrt{2q}\,\mathrm{sech}\left(\sqrt{2q}\tau\right) e^{iq\xi} \tag{5.1}$$

where τ is a dimensionless unit of time, ξ is a dimensionless unit of distance and q is the wavenumber. The usual derivation of this form can be found using the inverse scattering transform [2, 137].

5.2.2 Čerenkov Radiation

The soliton solutions to the NLS equation are highly stable to perturbations. This is because the soliton modifies the dispersion characteristics of the medium so that there are no dispersive waves with real frequencies having wavenumbers close to the soliton ones [138]. However, when the GVD of the fibre changes significantly over the spectral bandwidth of the pulse whereby we have appreciable higher-order dispersion, the wavenumbers of dispersive radiation and parts of the soliton spectrum are matched at a given frequency. The matching of wavenumbers in this case can yield resonant radiation known as *Čerenkov radiation* or *non-solitonic radiation* [2, 16, 138–144].

One clear characteristic required for this exchange is non-zero spectral amplitude within the soliton at this frequency [141]. The amplitude of the emitted radiation is primarily determined by the spectral amplitude of the soliton at the resonance frequency, ω_r. The spectral amplitude of an ideal soliton with central

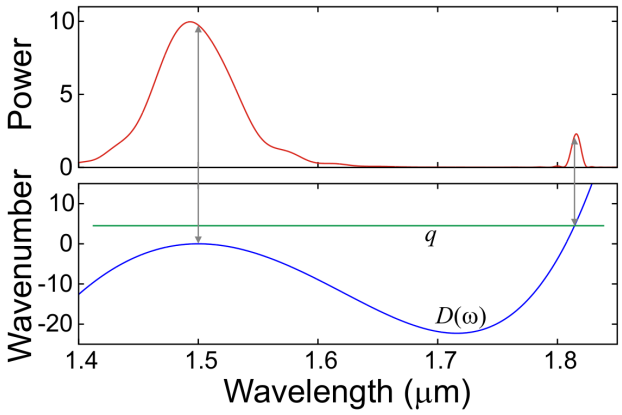

Figure 5-1: (top) The output of a 33.3 fs pulse at 1.5 μm after 0.6 mm propagation in a 220 nm x 380 nm silicon waveguide. The soliton (left hand peak) is formed and produces the Čerenkov radiation (right hand peak). The frequency of this peak can be found by matching the soliton wavenumber to the linear wavenumber (bottom). This plot shows the dispersion relations of both the soliton (marked q) and the dispersive waves (marked $D(\omega)$ in the frame of reference of the soliton. Reprinted from [16].

frequency ω_s is given by:

$$\frac{1}{e^{-(\omega_r-\omega_s)\pi\tau/2}+e^{(\omega_r-\omega_s)\pi\tau/2}}, \tag{5.2}$$

where τ is the soliton duration. It can be seen that as the soliton approaches the zero-GVD wavelength the resonance frequency will get closer to the soliton frequency and the intensity of the emitted radiation will increase exponentially [138] as the intensity of the soliton at that frequency increases.

There are two important points here, the wavelength of the resonance and how the intensity of the Čerenkov radiation can exceed the intensity of the soliton at that wavelength. Let us consider a soliton travelling in a system with appreciable higher-order dispersion (fig. 5-1). In this case, we are forming the soliton close to the second zero-GVD point of the waveguide, where the GVD slope, and hence the third-order dispersion, β_3, is negative. In this case we can see that the resonance occurs on the long wavelength edge of the soliton, in agreement with the literature [139–141].

To calculate the resonance condition, the ideal soliton solution is input in the equations of motion. The resulting outcome is

$$q = D(\omega) \tag{5.3}$$

where the resonance exists at frequency where the soliton dispersion relation, q, is equal to the dispersion relation of the dispersive waves, $D(\omega)$. For this analysis, the frame of reference of the system is the moving frame of reference of the soliton and as such q appears as a constant (all frequncies travel at the same speed) as shown by the straight green line in figure 5-1. The dispersion of the linear waves in this frame of reference yield the curve $D(\omega)$ labelled in figure 5-1. At the central frequency of the soliton, $D(\omega)$ has a point of inflection. In the absence of higher-order dispersion, the soliton wavenumber would be higher than that of the dispersive waves for all frequencies; due to the local modification of the refractive index by the soliton [138]. As such, the wavenumber of the dispersive waves in the soliton frame of reference, $D(\omega)$, becomes negative - even though they are not negative in the laboratory frame of reference. In the presence of higher order dispersion, this is not the case, and the above equation yields a resonance condition whereby the wavenumber of the soliton and the dispersive waves is the same (fig. 5-1). Between the central frequency of the soliton, and the resonant radiation freqeuncy there is a point of inflection in the dispersion relation of the dispersive waves. This point of inflection marks the transition from an anomalous dispersion regime (where the soliton is formed) to a normal dispersion regime (where the radiation is emitted).

So the soliton intensity at the frequency of the resonance acts as a source for the dispersive waves, with photons moving from one to the other. The driving force of this transfer is not discussed in the literature. The soliton, or perhaps more accurately pseudo-soliton due to the fact that it is constantly losing energy to the dispersive waves [144], looks to reform itself. In losing energy it will lose peak power and get temporally broader at the same time (reducing its band-width). This reformation, and the Kerr non-linearity and anomalous dispersion that drive it, means that more energy is present at the resonance wavelength; enabling further emission into the dispersive wave. Under these conditions, there

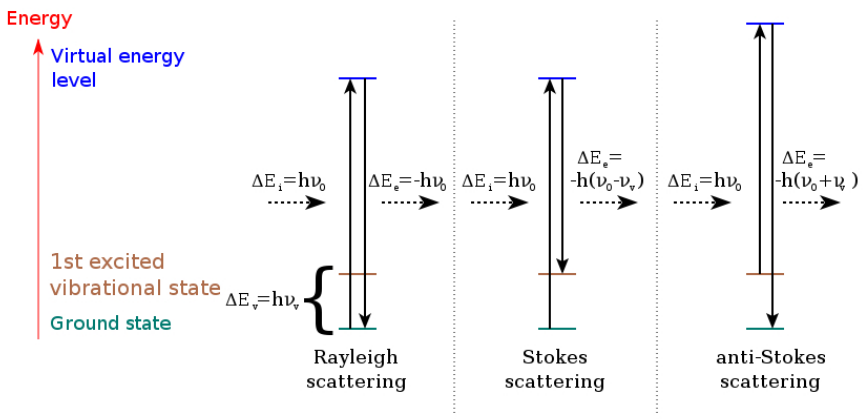

Figure 5-2: Cartoon depicting the Raman effect. The left hand diagram shows Rayleigh scattering, where the incident and scattered photons are the same. The other two diagrams show Raman scattering, with the scattered photon having both a lower (centre) and higher (right) energy than the incident photon.

will come a point whereby the rate of exchange of energy is negligible and the soliton is temporally longer and spectrally narrower to the point where the overlap to the resonance condition is negligible. At this point we can think that the energy transfer has effectively stopped [139, 141].

Spectral Recoil and Raman shift

The characteristics of Čerenkov radiation in the waveguides we are considering, depend on two further mechanisms worth discussing.

The first is the soliton self-frequency shift, due to Raman scattering. Raman scattering is an inelastic scattering process [145]. Usually when a photon is scattered, the energy of the incoming and outgoing photons are the same, an elastic scattering event. However, if the scattering process involves an excitation to a higher vibrational, rotational or electronic energy state then the the process is inelastic and the incoming and outgoing photons have different energies (fig:5-2). The incident photon can thus be red-shifted or blue shifted depending on whether it loses or gains energy from the medium through Stokes scattering or Anti-Stokes scattering.

For pulse widths on the order of picoseconds the spectral width of the pulse is large enough that the Raman gain can amplify the low frequency components,

with the high frequency components acting as a pump. This process continues along the fibre with the continuous transfer of energy to red components and a self-frequency shift of the soliton to redder wavelengths.

Therefore, as a soliton approaches a red-shifted zero-GVD point in the presence of negative third-order dispersion, the intensity of the red-shifted Čerenkov radiation is expected to increase [138, 141].

This growth of radiation should saturate due to spectral recoil. The conservation of momentum yields the concept that the spectral centre of mass is invariant to propagation [141]. Any radiation to longer wavelengths results in a spectral recoil of the soliton away from the radiation and back into the anomalous dispersion regime (in this case blue-shifting it) [139, 140]. This recoil can be seen in figure 5-1. If we are not seeing a red-shift due to the presence of the Raman nonlinearity, the change of energy to long wavelengths must be directly being emitted into the dispersive waves, rather than shifting the soliton.

In the absence of a Raman response, the soliton will continue to emit radiation and experiencing the subsequent spectral recoil until the soliton stabilises itself through dispersive wave losses. At this point the radiated energy and associated spectral recoil are negligible [141]. This point, also sets an lower limit on the distance from the zero-GVD that a soliton can be launched without experiencing these dispersive losses.

Relation to Particle Physics

Čerenkov radiation is emitted when a charged particle travels faster than the phase velocity of light. It is commonly seen as a blue glow surrounding water-cooled nuclear reactors. Charged particles from the reactor, usually electrons, enter the water whereby they are travelling faster than the speed light would normally travel in water. The charged particles polarise the atoms of the insulating material, which emit photons to return to their ground state. One can say that the Čerenkov effect takes place if the wavenumber of the wave created by the particle becomes smaller than the wavenumber of the dispersive wave for the same frequency. The wavenumber matching condition is satisfied and radiation is emitted under some angle to the direction of the particle motion [138]. The dispersive radiation described above can be shown to be exactly the same as the Čerenkov radiation of particle physics [16, 141, 146]. A waveguide can be consid-

ered here as a one-dimensional system and the angle is in the space-time plane. This angle determines the frequency of the dispersive wave relative to the soliton frequency [138].

5.2.3 Solitons in Waveguide arrays

Up to now, the consideration of solitons has been exclusively in the temporal domain. Within an array of silicon photonic waveguides, such solitons are known as solitonic supermodes, whereby the soliton has a spatial profile coinciding with one of the linear supermodes of the array (fig. 5-3a). Solitonic supermodes have previously been reported in the literature [89, 142, 147]. Given an excitation regime, whereby a number of supermodes were excited, at a given power, the relative dispersion relations of each supermode will determine which modes can support solitons at that given input power. This would depend on whether the soliton threshold, the peak power required to generate a soliton [2,16], was reached for that supermode:

$$P_0 = \frac{|\beta_2|}{T_0^2 \gamma} \tag{5.4}$$

where T_0 is the pulse duration, γ is the nonlinear parameter given by $\gamma = n_2\omega_0/S_{eff}c$ and β_2 is the dispersion parameter for that particular supermode. Obviously given this equation, the required power to form a soliton is inversely proportional to the product of the duration of the soliton and the nonlinear parameter. It can be seen that in general, a soliton can always be formed for nominally weark nonlinearity and/or low power as long as the above equation holds. In such cases they will be temporally broad (large T_0) and may be fragile in practice [148] and will exist as supermodal solitons.

This is not the only soliton formation that we can expect within the aforementioned arrays. Self-trapping of an optical beam in a continuous medium can form a spatial soliton [149]. The normal behaviour of diffraction is counteracted by self focusing; a convergence of the beam due to the nonlinear refractive index increase. This self focusing can be thought of as the spatial analogy to self-phase modulation in the time domain. This behaviour is also observed in

discrete spatial media, such as the silicon photonic wire arrays described here. In this case the suppression of inter-waveguide coupling yields a discrete spatial soliton [150, 151]. One advantage to considering discrete media over continuous ones is the reduction in the power requirements for spatial soliton formation [16].

Arrays of silicon photonic wires are a prime candidate for studying spatiotemporal solitons due to their relatively high nonlinearity, which helps to reduce the required pump power, combined with the tunability of both the dispersion length and the coupling length, our discrete diffraction length. The balancing of these lengths is crucial for observation of spatiotemporal solitons [89].

Increasing the power above that required for soliton formation, to a given threshold, breaks the symmetry of the solitonic supermodes so that the stable solution no longer reflects the spatial symmetry of the linear system [147,152]. This yields a low-power range whereby supermodal solitons are expected to dominate, and a high-power range whereby it is expected that spatiotemporal solitons will dominate the propagation physics.

Čerenkov radiation as a signature of solitons in waveguide arrays

We have seen above, that Čerenkov radiation can be emitted from a soliton given higher-order dispersion. This is also true for spatiotemporal solitons and supermodal solitons. In general, a N-wire system will exhibit N separate resonant frequencies. The presence of these frequencies is controlled by the symmetry of the array. Using the same analysis as above, the effect of substituting a perturbed ideal soliton solution into the NLS equation we obtain a similar output

$$q\vec{E}_n = D(\omega)\vec{E}_n + C(\omega)(\vec{E}_{n-1} + \vec{E}_{n+1}. \tag{5.5}$$

Here $\vec{E}_n$ is the amplitude of the electric field in wire n, $D(\omega)$ relates to dispersion and $C(\omega)$ the coupling coefficient of the system that describes the discrete diffraction present. When solved, this eigenvalue problem yields the eigenvectors describing the modes of the system (fig. 5-3a). Combining the eigenvector equations with the resonance condition yields the equation defining the N wavelength radiation peaks of the system [16]:

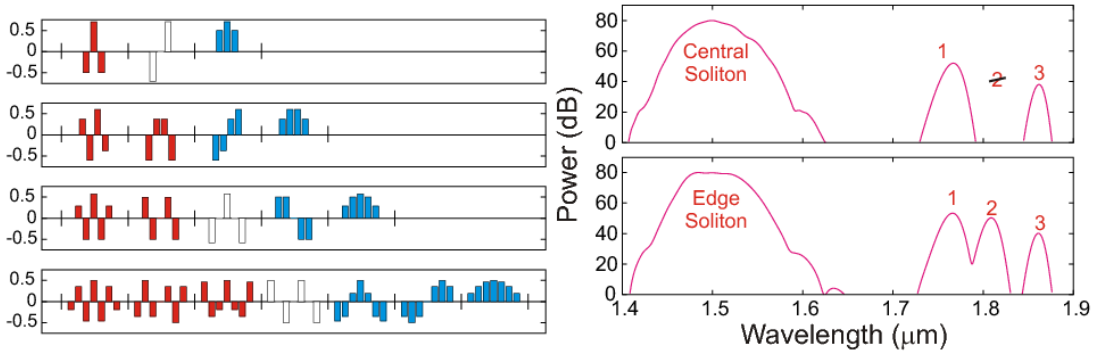

(a) (b)

Figure 5-3: (a) Normalised eigenvectors shown for (top to bottom) 3, 4, 5 and 7 channels. Each eigenvector corresponds to an amplitude projection in each waveguide across the array. (b) Power spectra summed over all three waveguides after 2.4 mm propagation distance for a 3-channel array of 220 nm x 380 nm waveguides. Both the symmetric and asymmetric excitation conditions are shown. Clearly the presence of the radiation peak in the antisymmetric mode is suppressed for the centrally excited spatiotemporal soliton. Reprinted from [16].

$$q = D(\omega) + 2C(\omega)cos\left(\frac{j\pi}{N+1}\right). \tag{5.6}$$

Both supermodal and spatiotemporal solitons will emit Čerenkov radiation. In the case of supermodal solitons, the radiation will be emitted into the specific supermode that the soliton is propagating in (as no other supermodes have a non-zero projection onto that mode). A soliton that is propagating as a spatiotemporal soliton will emit radiation into multiple different dispersive waves as it will have non-zero projection on more than one supermode. These radiation into these modes will happen at different resonant frequencies depending on the dispersion relations of the specific supermodes.

Soliton Excitation

Excitation of individual solitons is non-trivial. In the case whereby we are in the spatiotemporal soliton power regime then there are two distinct types of soliton: edge solitons and central solitons.

Consider the simplest case of a three-channel array. If a spatiotemporal soliton forms in the central waveguide, it must be made up of a superposition of the two symmetric supermodes (fig. 5-3a). Therefore, it can only project radiation into these modes (fig. 5-3b). If the soliton forms in either of the edge waveguides, then the spatial profile can only be made from a superposition of all of the supermodes. In this case, the resonance condition can be Čerenkov satisfied by all of the supermodes and thus we can observe three radiation peaks in the output spectrum (fig. 5-3b).

Perfectly symmetric or antisymmetric excitation conditions could lead to one of these scenarios. Another possibility is to extend one of the waveguides at the input end, coupling light into this will mean that as the array starts you have a very defined supermode contirbution. This does however pose a problem in that nonlinear interactions will happen during this propagation in the extended single channel. One way around this would be to weaken the nonlinear interaction by changing the intensity in the coupled mode. This could be done by tapering an extended input waveguide (so that it started much bigger than the waveguides comprising the array) [153], or by cladding it in a higher index dielectric so that the mode was less confined to the silicon [94, 122].

When we consider supermodal solitons we have a more complex excitation requirement. Whilst the energy of a spatiotemporal soliton is confined primarily to a single photonic wire within the array, supermodal solitons have a more spatailly dipsersed energy profile. In the same way that I discussed using tapered input waveguides to couple light selecitvely into individual waveguides for exciting spatiotemporal solitons, a similar method could be employed for supermodal solitons. However, coupling in adjacent input tapers would need to be considered. Also, generation of a phase change across the waveguides (in the case of higher-order spatial wavevectors) would need to be addressed. Potential avenues for exploration would be the use of phase mask [154] or inducing the phase change using waveguides of different path lengths, by creating curved input waveguides for example.

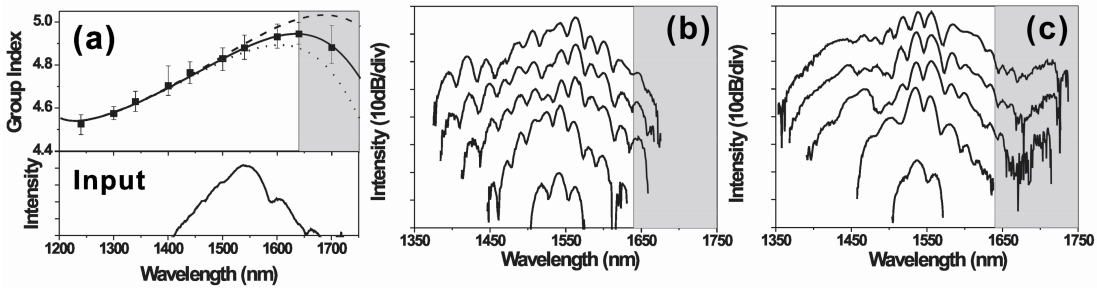

Figure 5-4: (a) Measured group indices of a 3-channel array of SOI waveguides (dots). The numerically calculated values for each supermode are represented by the dotted, dashed and solid curves. The grey area indicates where the second region of normal dispersion. Directly below this measurement is the input spectra for the nonlinear measurements. Transmission spectra of OPA pulses through a 3-channel waveguide array with central (b) and edge (c) excitation conditions. A 10 dB offset has been applied between adjacent measurements for clarity.

5.3 Spatiotemporal Soliton Experiments

In the preliminary sections of this chapter, we discuss that control of both the dispersion, coupling and nonlinear lengths was important for generating the right conditions to observe spatiotemporal solitons. Our experiments use a three-channel array containing waveguides of 220 nm x 380 nm in cross section that have a wall-to-wall separation of 600 nm. Three channels were chosen as this is the simplest geometry that can display both a central and edge bullet, a geometry that gives us an ability to control the generation of the radiation from the antisymmetric mode. These experiments were conducted alongside Dr. Wei Ding of the University of Bath. The work on measurement of the dispersion is my own, but the non-linear measurements were started by myself and built upon by Wei Ding. The specific results were taken by Wei Ding but the experimental set-up was developed together.

Using the methods discussed in Chapter 3, I measured the dispersion using a white light interferometer (fig. 5-4). I also performed numerical FEM simulations for comparison. Using this data the dispersion length of a 150 fs pulse as approximately 0.6 mm and the coupling length as approximately 0.6 mm. The nonlinear length, given a peak power of 10 W, is 0.5 mm.

Experimental probing of these conditions was done by using an input pulse

directly from an optical parametric amplifier (OPA). This amplifier is a Coherent 9850, as described in the previous section, and is pumped by an ultra-fast laser system from Coherent. The output pulses from the OPA are measured as 150 fs, using a two-photon absorption based autocorrelator, centred at 1540 nm. The pump pulses were input into the waveguide array using a 60× aspheric objective lens (numerical aperture of 0.65). This yielded a calculated spot size of 1.45 μm. Whilst this spot-size is not small enough to illuminate a single waveguide, it is small enough to be manoeuvred across the face of the array to control the symmetry of the excitation. This was achieved by moving the waveguide array in the focal plane using a micro-positioning stage. Collection optics were another set of aspheric coupling lenses to collimate the output from the waveguide array and then couple into a single-mode optical fibre. This optical fibre was connected to an optical spectrum analyser.

Output spectra were recorded for average input powers of 0.08 μW, 6.2 μW, 37 μW, 74 μW and 123 μW. The power was controlled by rotatable polarising beam-splitter-cubes in the input optical beam, as has been described in the previous chapters of this thesis. The powers recorded equate to peak input powers inside the waveguides of up to 16.4 W, given an approximate -23 dB coupling insertion loss.

Under these conditions we observe clear generation of new wavelengths at 1720 nm when the excitation is assymetric and the majority of the input is concentrated into the edge waveguide. If this were the case, then the radiation could be attributed to the antisymmetric mode; which is only present in this coupling regime. If the pump beam is aligned with the geometrical centre of symmetry it has a zero projection onto this mode.

Let us consider the dispersion relations of all the excited modes, in the frame of reference of the soliton, at the pump frequency of 1540 nm (fig. 5-5). It can clearly be seen that the soliton dispersion relation (black line) intersects with dispersion relation of a dispersive wave in the antisymmetric mode (solid blue line). This occurs 176 nm from the pump, at a wavelength of 1716 nm. This is consistent with the data from the experiment shown in figure 5-4.

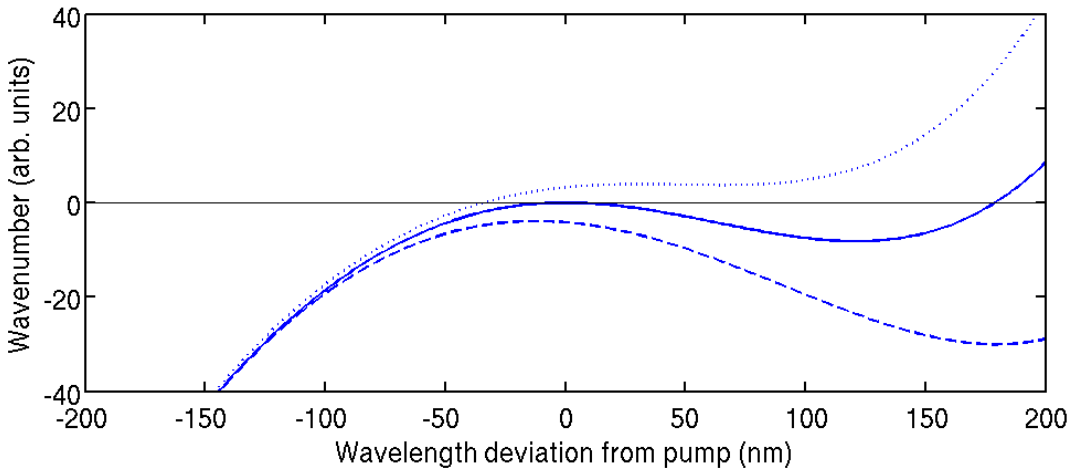

Figure 5-5: Graph showing both solitonic (black line) and linear wavenumbers (blue lines) for a three channel array. The soliton is shown with a nominal zero q value for clarity, at a pump wavelength of 1540 nm. A single resonance condition can be observed, 176 nm away from the pump wavelength (at a wavelength of 1716 nm). This radiation is in the antisymmetric supermode of the array.

5.4 Subsequent Work

Subsequent to the work presented above, my colleagues at the university of Bath furthered the numerical study of spatiotemporal solitons in silicon photonic wires [135, 136]. These works involved refining the experimental measurements further using narrower pulses, with a duration of 120 fs, and generating a more comprehensive set of results (fig. 5-6). Experimentally the main contribution came from Dr. Wei Ding. However, the biggest difference was the complex numerical modelling undertaken to understand the experimental results. This was completed by Dr. A. Gorbach and O. K. Staines.

5.4.1 Modelling Spatiotemporal Solitons

Numerically solving linear Maxwell's equations shows that adjacent wires are coupled through their evanescent tails. Nonlinear propagation can be approximated through a set of coupled nonlinear Schrödinger equations:

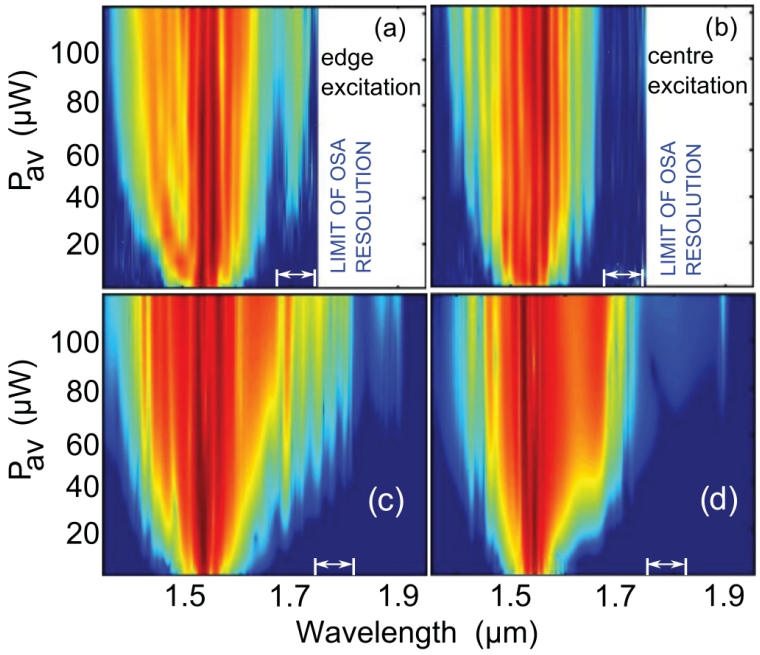

Figure 5-6: Experimentally measured transmission spectra of 120 fs pulses for the edge (left) and centre (right) excitations as a function of increasing power. The edge of the image denotes the edge of the detection bandwidth provided by the optical spectrum analyser. A spectral component can clearly be seen at the long wavelength side of the pulse for an edge excitation that is not present when the waveguide array is excited symmetrically. This is highlighted by the white arrow. Below the experimental measurements are the corresponding numerical calculations (c,d) with the spectral region of the excitation dependent spectra observed experimentally highlighted by a white arrow. Reprinted from [135].

$$\partial_z E_n = i\hat{D}\left(i\partial_t\right) E_n + i\hat{C}\left(i\partial_t\right)\left(E_{n-1} + E_{n+1}\right) + i\gamma\left(1 + i\epsilon_{tpa}\right)|E_n|^2 E_n - \left(\epsilon + \sigma_{fcc} Q_n\right) E_n \tag{5.7}$$

where n is the wire number and E_n is the amplitude of the electric field in wire n, γ is the nonlinear coefficient, ϵ_{tpa} is the two-photon absorption coefficient, ϵ is the linear loss. Q_n is the free carrier density and σ_{fcc} is the free carrier scattering coefficient. $\hat{D}(i\partial_t)$ and $\hat{C}(i\partial_t)$ are the polynomial operators for dispersion and coupling respectively [135].

In the absence of the nonlinearity, the resulting dispersive wave equation is usually solved in the frequency domain. The nonlinear terms, a form of nonlin-

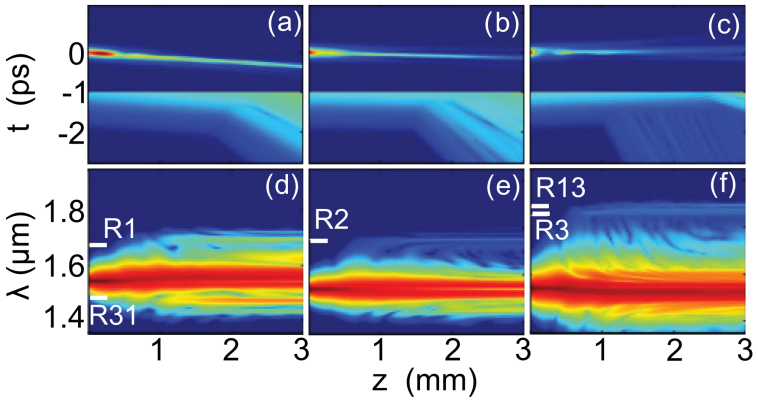

Figure 5-7: (a-c) Temporal and (d-f) spectral evolution of the S_1 (a,d), S_2 (b,e) and S_3 (c,f) supermodes along the array under edge excitation with average power of 70 muW. The soliton and linear radiation are plotted on a different intensity scale to enable both to be seen simultaneously. In the spectral plots, R_1, R_2 and R_3

ear phase equation, are more readily solved in the time domain. Therefore the solution is to employ a split-step Fourier technique [2, 16].

In this work A. Gorbach *et al* numerically model the NLS equation using two types of initial condition. Firstly, where the input pulse is coupled into an edge wire, exciting a superposition of all three supermodes; and secondly when the pulse is coupled into the central wire so that a superposition of the symmetric supermodes only is excited. The modelling suggests that during the propagation through the array, the S_3 supermode (which is symmetric but with the edge waveguides out of phase with the centre one) has the highest threshold. During propagation it becomes distorted (fig. 5-7). The other modes are more stable over the 3 mm length of the waveguides. All three supermodes emit resonant radiation at a certain stage of their evolution. This radiation propagates at different group velocities and therefore separates from the soliton in the time domain. In the spectral domain (fig. 5-7), it forms peaks that break the symmetric spectral broadening of self-phase modulation. If only the central wire is pumped, the S_2 mode is not excited, while the evolution of the other modes is broadly similar to the edge excitation shown. Both inter-mode and intra-mode radiation can be observed. Inter-mode radiation is allowed between the S_1 and S_3 supermodes due to symmetry.

In order to compare the numerical and modelling results, the numerical output in one of the edge wires is monitored. Unlike the central wire, this carries a component of all the excited supermodes. The resulting spectrum vs. power can be seen in figure 5-6. There is very good qualitative agreement with the experimental measurements. The radiation in the spectral region around 1720 nm is directly associated with the intra-mode resonance of the quasi-soliton in the S_2 supermode. There is a slight shift towards shorter wavelengths due to the approximation of the dispersion model of bulk silicon used in the numerical modelling.

Distinguishing Spatiotemporal and Supermodal solitons

As discussed by A. Gorbach [135] it is expected that supermodal solitons will dominate nonlinear propagation characteristics below the point whereby symmetry breaking occurs. However, in experimental context this means that using Čerenkov radiation will not be sufficient to discern between the two regimes. Both solitonic supermodes and spatiotemporal solitons will both generate Čerenkov radiation at the same resonances. Consider pulse injection that is completely symmetric through the waveguides (injected into the centre waveguide). This will have non-zero projection onto the antisymmetric supermode. Regardless of power, once either two supermodal solitons or a spatiotemporal soliton have been formed, both will emit Čerenkov radiation into dispersive waves travelling into the other two modes. The same analysis is true for edge excitations, where all the dispersive radiation will exist in all three modes.

It has been reported [16] that spatiotemporal solitons contain much more energy, and require higher peak power to form compared to their supermodal counterparts. In his thesis, such a ratio was of the order of 3.5, for a given pumping regime. This suggests that it is potential possible to form higher-order supermodal solitons before spatiotemporal solitons can form. Cross correlation measurements of the input and output pulses in this regime may help discern whether we are inside this higher-order soliton regime. These same temporal measurements could discern the relative delays of each component of the signal, potentially enabling some further analysis in the temporal domain.

The other, and more striking option is to look at the spatial signature of the propagation. The amplitude of the Čerenkov radiation produced is much

smaller than the amplitude of the soliton, and as such a large proportion of the intensity of the output light would be in the spatial profile of the soliton. In the supermodal soliton regime,this would be in the superposition of the excited supermodes, whereas in the spatiotemporal soliton regime, the output light would be located in a single waveguide only when it was created (due to the superposition of the supermodes). However, after some distance of propagation, the modes would not be in phase and the amplitude of the observed intensity pattern would be a superposition of all of the supermodes dependent on their relative phase shifts. Characterisation of this type could be done by collecting a magnified image of the output faces of the waveguides. Given the small geometry bulk optics may not be suitable and perhaps some form of scanning near-field measurement, for example rastering a tapered fibre tip across the end face of the array, may provide more resolution.

Therefore, Čerenkov radiation is a good signature for the presence of solitons, but cannot be used as the sole characteristic to determine which soliton regime you are in. Other measurement techniques will also be needed.

5.5 Summary

In summary, I have shown preliminary experimental measurements that show pronounced generation of new wavelengths when a 3-channel array is pumped by 150 fs pulses centred at 1550 nm. These wavelengths are only generated during asymmetric input coupling and are shown to be at the same frequency of resonant radiation, or Čerenkov radiation, in the asymmetric waveguide mode. Further work completed at the University of Bath corroborates these results by comparing more detailed experimental results with numerical calculations of nonlinear propagation. Whilst this work shows that the peaks are undoubtedly Čerenkov radiation emitted from propagating solitons, no distinction is made between supermodal and spatiotemporal solitonic behaviour.

Chapter 6

Conclusions and Future Work

In this thesis I have explored linear and nonlinear optics across two different forms of optical waveguides. Linear and nonlinear experimentation has been undertaken, the results of which have been confirmed by numerical modelling by both myself and other members of the University of Bath.

In chapter 2, I reported on modelling done that shows that dual-core hollow-core photonic crystal fibre can support a decoupling of the core modes of adjacent cores. This work extends published literature concerning all-solid fibre to consider fibres of an air-silica matrix. With this new geometry, a decoupling point has been found numerically. This point shows an increase in the coupling length of over two orders of magnitude, similar in value to the academic literature. This is the first work to attempt to understand decoupling in a fibre comprising a silica-air matrix as its cladding. Future work, to experimentally observe the decoupling has been suggested to further explore this phenomenon.

In chapter 3, I discussed linear optics in silicon photonic waveguides. The dispersive properties of arrays of waveguides were investigated experimentally and numerically. The experimental results showed observation of coupling-induced dispersion of similar order to the group-velocity dispersion of a single waveguide. This confirmed predictions made by Christopher Benton of the University of Bath in previously published work. In this chapter I also numerically and experimentally observed the transition from a waveguide-guidance regime to a slot-guidance regime, and discussed the accompanying modal anti-crossing that was present during this transition.

In chapter 4, I presented preliminary work pertaining to modulation instabil-

ity within silicon waveguide arrays. The experimental set-up and initial results, whereby only a single photonic wire is concerned, have been described. In this work, 6.2 ps pulses of 18 W peak power were input into a silicon waveguide in order to observe modulation instability. Although non-linear effects were observed, there is not significant evidence of modulation instability in this configuration. The chapter concludes with a description of the continuation of this work by colleagues at the University of Bath, primarily by Dr. Wei Ding. In this work, we observe modulation instability and its pronounced dependence on the coupling-induced group-velocity dispersion, using a seeded, non-degenerate configuration.

Again, in chapter 5, I present my preliminary experimental measurements that show pronounced non-linear wavelength generation when a 3-channel array is pumped by 150 fs pulses centred at 1550 nm. These wavelengths are only generated during asymmetric input coupling and are shown to be at the same frequency of resonant radiation, or Čerenkov radiation, in the asymmetric waveguide mode. Subsequent progression of these initial results by Dr. Wei Ding and Dr. Andrey Gorbach have also presented. The initial results were corroborated by comparing more detailed experimental results with numerical calculations of nonlinear propagation. This work shows that the peaks are undoubtedly Čerenkov radiation emitted from propagating solitons, but it remains difficult to distinguish whether the observed phenomena originate from supermodal- or spatiotemporal-solitonic behaviour.

Appendix A

Previously Published Work

A.1 Journal Publications

M. G. Welch, C. E. de Nobriga, R. A. Correa, W. J. Wadsworth and J. C. Knight, "Accurate Measurement of the Dispersion of Hollow-Core Fibers Using a Scalable Technique", Optics Express, **17**, 9006-9012, (2009).

C. E. de Nobriga, G. D. Hobbs, W. J. Wadsworth, D. Skryabin, J. C. Knight, A. Samarelli, M. Sorel and R. M. De La Rue, "Supermode Dispersion and Waveguide-to-Slot Mode Transition in Arrays of Silicon-on-Insulator Waveguides", Optics Letters, **35**, 23, 3925–3927 (2010)

A. V. Gorbach, W. Ding, O. K. Staines, C. E. de Nobriga, G. D. Hobbs, W. J. Wadsworth, J. C. Knight, D.V. Skryabin, A. Samarelli, M. Sorel and R. M. De La Rue, "Spatio-temporal nonlinear optics in arrays of subwavelength waveguides", Physical Review A **82**, 4, 041802 (2010)

W. Ding, O. K. Staines, G. D. Hobbs, A. V. Gorbach, C. E. de Nobriga, W. J. Wadsworth, J. C. Knight, D. V. Skryabin, M. J. Strain, M. Sorel, R. M. De La Rue, "Modulational instability in a silicon-on-insulator directional coupler: role of the coupling-induced group velocity dispersion ", Optics Letters, OSA, **37**, 4, 668–670 (2012)

A.2 Conference Publications

J. C. Knight, M. G. Welch, C. E. de Nobriga and R. Amezcua Correa, "Controlled Dispersion in Photonic Crystal Fibers", Conference on Lasers and Electro-Optics (CLEO), OSA, Paper CMW1, (2009)

C. E. de Nobriga, W. J. Wadsworth, A. V. Gorbach, D. V. Skryabin, J. C. Knight, A. Samarelli, M. Sorel and R. M. De La Rue, " Supermode Dispersion of Strongly Coupled Silicon-on-Insulator Waveguides", Conference on Lasers and Electro-Optics (CLEO), OSA, Paper CThB4 (2010)

C. E. de Nobriga, G. D. Hobbs, W. Ding, A. V. Gorbach, W. J. Wadsworth, J. C. Knight, D. V. Skryabin, A. Samarelli, M. Sorel and R. M. De La Rue, "Supermode Dispersion and Mode Transitions in Silicon-on-Insulator Waveguide Arrays", Nonlinear Photonics (NP), OSA, Paper NME1 (2010)

W. Ding, C. E. de Nobriga, G. D. Hobbs, W. J. Wadsworth, J. C. Knight, A. V. Gorbach, O. K. Staines, D. V. Skryabin, A. Samarelli, M. Sorel, and R. M. De La Rue, "Spectral Signatures of Spatio-Temporal Solitons in Arrays of Silicon-on-Insulator Photonic Wires", Nonlinear Photonics (NP), OSA, Paper NWA4 (2010)

Wei Ding, Charles de Nobriga, Gareth Hobbs, William Wadsworth, Jonathan Knight, Andrey Gorbach, Owain Staines, Dmitry Skryabin, Antonio Samarelli, Mark Sorel and Richard De La Rue, "Spectral signatures of spatio-temporal solitons in arrays of silicon-on-insulator photonic wires", Photon 10, IOP, Paper (2010)

A. V. Gorbach, W. Ding, O. K. Staines, C. E. de Nobriga, G. D. Hobbs, W. J. Wadsworth, J. C. Knight, D. V. Skryabin, A. Samarelli, M. Sorel and R. M. De La Rue, "Solitonic supermodes and resonant radiation in subwavelength silicon-on-insulator", European Optical Society Annual Meeting (EOSAM), Paper 3347 (2010)

W. Ding, A. V. Gorbach, O. K. Staines, C. E. de Nobriga, G. D. Hobbs, W.

J. Wadsworth, J. C. Knight, D. V. Skryabin, A. Samarelli, M. Sorel, R. M. De La Rue, “Spatio-Temporal Nonlinear Optics in Arrays of Subwavelength Waveguides ”, Conference on Lasers and Electro-Optics (CLEO), OSA, (2011)

References

[1] A.W. Snyder and J.D. Love. *Optical Waveguide Theory*. Chapman and Hall, 1983.

[2] G. P. Agrawal. *Nonlinear Fiber Optics*. Elsevier/Academic Press, London, 4^{th} edition, 2007.

[3] M. Born and E. Wolf. *Principles of Optics*. Pergamon Press Ltd., Oxford, 2^{nd} edition, 1964.

[4] J. M. Stone. *Photonic Crystal Fibres and Their Applications in the Nonlinear Regime*. Phd thesis, University of Bath, Department of Physics, University of Bath, Claverton Down, Bath BA2 7AY, April 2009.

[5] Elizabeth Geller, editor. *Dictionary of Physics*. McGraw-Hill, 3rd edition, 2002.

[6] Bob Mellish. Transverse mode [online]. Available from: `http://en.wikipedia.org/wiki/Transverse_mode`. [Accessed 26-February-2012].

[7] R. Paschotta. *Encyclopedia of Laser Physics and Technology*. Wiley-VCH, Berlin, 1st edition, 2008.

[8] K.K. Lee, D.R. Lim, H.-C. Luan, A. Agarwal, J. Foresi, and L. C. Kimerling. Effect of size and roughness on light transmission in a si/sio$_2$ waveguide: Experiments and model. *Applied Physics Letters*, 77(11):1617–1619, 2000.

[9] K.K. Lee, D. R. Lim, L. C. Kimerling, J. Shin, and F. Cerrina. Fabrication of ultralow-loss si/sio$_2$ waveguides by roughness reduction. *Optics Letters*, 26(23):1888–1890, 2001.

[10] F. Ladouceur, J.D. Love, and T.J. Senden. Effect of side wall roughness in buried channel waveguides. *Optoelectronics, IEE Proceedings*, 141(4):242–248, 1994.

[11] F. F. Payne and J. P. R. Lacey. A theoretical analysis of scattering loss from planar optical waveguides. *Optical and Quantum Electronics*, 26:977–986, 1994.

[12] H. K. Tsang, C. S. Wong, T. K .Liang, I. E. Day, S. W. Roberts, A. Harpin, J. Drake, and M. Ashghari. Optical dispersion, two-photon absorption and self-phase modulation in silicon waveguides at 1.5 μm wavelength. *App. Phys. Lett.*, 80(3):416–418, 2002.

[13] B. Jalali. Silicon photonics: Nonlinear optics in the mid-infrared. *Nature*, 4(8):506–508, 2010.

[14] Q.Lin, J. Zhang, G. Piredda, R. W. Boyd, P. M. Fauchet, and G. P. Agrawal. Dispersion of silicon nonlinearities in the near infrared region. *Applied Physics Letters*, 91(2):021111, 2007.

[15] A. D. Bristow, N. Rotenberg, and H. M. van Driel. Two-photon absorption and kerr coefficients of silicon for 850–2200 nm. *Applied Physics Letters*, 90(19), 2007.

[16] C. J. Benton. *Solitons and Nonlinear Optics in Silicon-on-Insulator Photonic Wires*. Phd thesis, University of Bath, 2009.

[17] E. F. Schubert. *Light Emitting Diodes*. Cambridge University Press, 2nd edition, 2006.

[18] K. Rajagopal. *Textbook of Engineering Physics, Part 1*. PHI, New Dheli, 2008.

[19] P. Roberts, F. Couny, H. Sabert, B. Mangan, T. Birks, J. Knight, and P. Russell. Loss in solid-core photonic crystal fibers due to interface roughness scattering. *Opt. Express*, 13(20):7779–7793, 2005.

[20] Rodrigo Amezcua-Correa, N. G. Broderick, M. N. Petrovich, F. Poletti, and D. J. Richardson. Optimizing the usable bandwidth and loss through

core design in realistic hollow-core photonic bandgap fibers. *Opt. Express*, 14(17):7974–7985, 2006.

[21] N. Bloembergen. *Fundamentals of Photonics*, chapter Nonlinear Optics. John Wiley and Sons, 2nd edition, 2007.

[22] R. W. Boyd. *Nonlinear Optics*. Academic Press, 2nd edition, 2003.

[23] T. Kato, Y. Suetsugu, and M. Nishimura. Estimation of nonlinear refractive index in various silica-based glasses for optical fibers. *Opt. Lett.*, 20:2279–2281, Nov 1995.

[24] M. G. Welch. *Compressing and propagating solitons in hollow core photonic crystal fibre*. Phd thesis, University of Bath, Department of Phyiscs, University of Bath, Claverton Down, Bath BA2 7AY, 2010.

[25] T. E. Murphy. Ssprop : Split-step fourier propagation software, 2007.

[26] W. J. Tomlinson, R. H. Stolen, and C. V. Shank. Compression of optical pulses chirped by self-phase modulation in fibers. *J. Opt. Soc. Am. B*, 1(2):139–149, Apr 1984.

[27] M. Nisoli, S. De Silvestri, and O. Svelto. Generation of high energy 10 fs pulses by a new pulse compression technique. *Applied Physics Letters*, 68(20):2793–2795, 1996.

[28] S. A. Schelkunoff. Conversion of maxwell's equations into generalized telegrpahist's equations. *Bell Systems Technical Journal*, 33:661–719, 1955.

[29] H. A. Haus. Electron beam waves in microwave tubes. In *Proccedings of the Symposium on Electronic Waveguides, Polytechnic Institute of Brooklyn*, 1958.

[30] A. W. Snyder. Coupled-mode theory for optical fibers. *Journal of the Optical Society of America*, 62(11):1267–1277, 1972.

[31] D. Marcuse. Coupled mode theory of round optical fibers. *Bell Systems Technical Journal*, 52:1267–1277, 1973.

[32] A. Yariv. Coupled-mode theory for guided-wave optics. *IEEE Journal of Quantum Electronics*, QE 9(9):919–933, 1973.

[33] W.-P. Huang. Coupled-mode theory for optical waveguides: an overview. *J. Opt. Soc. Am. A*, 11(3):963–983, 1994.

[34] A.N. Kireev and T. Graf. Vector coupled-mode theory of dielectric waveguides. *Quantum Electronics, IEEE Journal of*, 39(7):866 – 873, july 2003. Coupled Mode Theory.

[35] T.A. Birks, D.M. Aitkin, G. Wyhlangowski, P.S. Russell, and P.J. Roberts. 2d photonic band gap strucutres in fibre form. In C.M. Soukoulis, editor, *Photonic Band Gap Materials*, volume 315 of *NATO ADVANCED SCIENCE INSTITUTES SERIES, SERIES E, APPLIED SCIENCES*, pages 437–444, 1996. NATO Advanced Study Institute on Photonic Band Gap Materials, ELOUNDA, GREECE, JUN 18-30, 1995.

[36] J. S. Foresi, P. R. Villeneuve, J. Ferrara, E. R. Thoen, G. Steinmeyer, S. Fan, J. D. Joannopoulos, L. C. Kimerling, H. I. Smith, and E. P. Ippen. Photonic-bandgap microcavities in optical waveguides. *Nature*, 390:143–145, 1997.

[37] Ying Xu, Hong-Bo Sun, Jia-Yu Ye, Shigeki Matsuo, and Hiroaki Misawa. Fabrication and direct transmission measurement of high-aspect-ratio two-dimensional silicon-based photonic crystal chips. *J. Opt. Soc. Am. B*, 18(8):1084–1091, 2001.

[38] G.J. Pearce. *Plane-Wave Methods for Modelling Photonic Crystal Fibre*. Phd thesis, University of Bath, 2006.

[39] Philip Russell. Photonic Crystal Fibers. *Science*, 299(5605):358–362, 2003.

[40] J. D. Joannopoulos, S. G. Johnson, J. N. Winn, and R. D. Meade. *Photonic Crystals : Molding the flow of light*. Princeton University Press, Princeton, N.J., 2nd edition, 2008.

[41] J. C. Knight, T. A. Birks, P. St. J. Russell, and D. M. Atkin. All-silica single-mode optical fiber with photonic crystal cladding. *Opt. Lett.*, 21(19):1547, 1996.

[42] F. Benabid. Hollow-core photonic bandgap fibre: new light guidance for new science and technology. *Phil. Tran. of the Roy. Soc. A*, 364(1849):3439–3462, 2006.

[43] R. Amezcua-Correa, N. G. Broderick, M. N. Petrovich, F. Poletti, and D. J. Richardson. Design of 7 and 19 cells core air-guiding photonic crystal fibers for low-loss, wide bandwidth and dispersion controlled operation. *Opt. Express*, 15(26):17577–17586, 2007.

[44] R. Amezcua-Correa, F. Gèrôme, S. G. Leon-Saval, N. G. R. Broderick, T. A. Birks, and J. C. Knight. Control of surface modes in low loss hollow-core photonic bandgap fibers. *Opt. Express*, 16(2):1142–1149, 2008.

[45] A.D. Fitt, K. Furusawa, T.M. Monro, C.P. Please, and Richardson D.J. The mathematical modelling of capillary drawing for holey fibre manufacture. *Journal of Engineering Mathematics*, 43:201–227, 2002.

[46] K. Okamoto. *Fundamentals of Optical Waveguides*. Elsevier Inc., 2nd edition, 2010.

[47] H. c. Huang. *Coupled mode theory as applied to microwave and optical transmission*. VNC Science Press, 1984.

[48] Carlo G. Someda. Antiresonant decoupling of parallel dielectric waveguides. *Opt. Lett.*, 16(16):1240–1242, Aug 1991.

[49] S Boscolo, M Midrio, and CG Someda. Directional couplers and decouplers in photonic crystal waveguides: Simulations and theory. In M Marciniak, editor, *ICTON 2001: 3RD INTERNATIONAL CONFERENCE ON TRANSPARENT OPTICAL NETWORKS, CONFERENCE PROCEEDINGS*, pages 80–83. IEEE, 2001. 3rd International Conference on Transparent Optical Networks (ICTON 2001), KRAKOW, POLAND, JUN 18-21, 2001.

[50] S. Boscolo, M. Midrio, and C.G. Someda. Coupling and decoupling of electromagnetic waves in parallel 2d photonic crystal waveguides. *Quantum Electronics, IEEE Journal of*, 38(1):47 –53, jan 2002.

[51] Zhi Wang, Guiyun Kai, Yange Liu, Jianfei Liu, Chunshu Zhang, Tingting Sun, Chao Wang, Weigang Zhang, Shuzhong Yuan, and Xiaoyi Dong. Coupling and decoupling of dual-core photonic bandgap fibers. *Opt. Lett.*, 30(19):2542–2544, Oct 2005.

[52] Z. Wang, T. Taru, T. A. Birks, J. C. Knight, Y. Liu, and J. Du. Coupling in dual-core photonic bandgap fibers: theory and experiment. *Opt. Express*, 15(8):4795–4803, Apr 2007.

[53] G.J. Pearce. *Fixed-Frequency Plane-Wave Solver for PCF*. University of Bath, February 2007.

[54] N. W. Ashcroft and N. D. Mermin. *Solid State Physics*. Thompson Press, 1976.

[55] R.P. Feynman. *The Feynman Lectures on Physics*, volume 2. Addison-Wesley, second edition, 2005.

[56] Daryl L. Logan. *A First Course in the Finite Element Method*. Cengage Learning, fifth edition, 2012.

[57] Giuseppe Pelosi. *Quick Finite Elements for Electromagnetic Waves*. Artech House, second edition, 2009.

[58] S.C. Brenner and L.R. Scott. *The Mathematical Theory of Finite Element Methods*. Springer, New York, 2008.

[59] Comsol. *Comsol Multiphysics User Guide*, November 2008.

[60] Jianming Jin. *The Finite Element Method in Electromagentics*. Wiley-IEEE Press, 2nd edition, May 2002.

[61] J. Berenger. A perfectly mathced layer for the absorption of electromagnetic waves. *Journal of Computational Physics*, 114(2):185–200, 1994.

[62] W. C. Chew and W. H. Weedon. A 3d perfectly matched medium from modified maxwell's equations with stretched coordinates. *Microwave Optical Tech. Letters*, 7(13):599–604, 1994.

[63] F. L. Teixeira and W. C. Chew. General closed-form pml constitutive tensors to match arbitrary bianisotropic and dispersive linear media. *IEEE Microwave and Guided Wave Letters*, 8(6):223–225, 1998.

[64] C. E. de Nobriga, W. J. Wadsworth, J. C. Knight, A. V. Gorbach, D. V. Skryabin, A. Samarelli, M. Sorel, and R. M. De La Rue. Supermode dispersion of strongly coupled silicon-on-insulator waveguides. In *CLEO*. OSA, 2010.

[65] C. E. de Nobriga, G. D. Hobbs, W. Ding, A. V. Gorbach, W. J. Wadsworth, J. C. Knight, D. V. Skryabin, A. Samarelli, M. Sorel, and R. M. De La Rue. Supermode dispersion and mode transitions in silicon-on-insulator waveguide arrays. In *NP*. OSA, 2010.

[66] C.E. de Nobriga, G. D. Hobbs, W. J. Wadsworth, J. C. Knight, D. V. Skryabin, A. Samarelli, M. Sorel, and R. M. De La Rue. Supermode dispersion and waveguide-to-slot mode transition ain arrays of silicon-on-insulator waveugides. *Opt. Lett.*, 35(23):3925–3927, 2010.

[67] E. D. Palik, editor. *"Silicon (Si)" in Handbook of Optical Constants*. Academic Press, 1985.

[68] S. Adachi. Model dielectric constants of si and ge. *Phys. Rev. B*, 38(18):12966–12976, 1988.

[69] I. H. Malitson. Interspecimen comparison of the refractive index of fused silica. *J. Opt. Soc. Am.*, 55(10):1205–1208, Oct 1965.

[70] M. Herzberger. Colour correction in optical systems and a new dispersion formula. *Optica Acta: International Journal of Optics*, 6(3):197–215, 1959.

[71] M. Herzberger and C. D. Salzberg. Refractive indices of infrared optical materials and color correction of infrared lenses. *J. Opt. Soc. Am.*, 52(4):420–424, 1962.

[72] H. Bach and N. Neuroth, editors. *The Properties of Optical Glass*, chapter Optical Properties. Springer-Verlag, Berlin, 1995.

[73] Schott. *Optical Glass Catalog*. Mainz, 1966.

[74] S. Adachi. *Properties of Group -IV, III-V and II-VI Semiconductors*. Wiley, 2005.

[75] P. Lautenschlager, M. Garriga, L. Vina, and M. Cardona. Temperature dependence of the dielectric function and interband critical points in silicon. *Phys. Rev. B*, 36(9):4821–4830, Sep 1987.

[76] Marvin L. Cohen and T. K. Bergstresser. Band structures and pseudopotential form factors for fourteen semiconductors of the diamond and zinc-blende structures. *Phys. Rev.*, 141(2):789–796, Jan 1966.

[77] M. Zaki. Bulk bandstructure in matlab: Pseudopotential method, Feb 2010.

[78] C. M. Herzinger, B. Johs, W. A. McGahan, J. A. Woollam, and W. Paulson. Ellipsometric determination of optical constants for silicon and thermally grown silicon dioxide via a multi-sample, multi-wavelength, multi-angle investigation. *Journal of Applied Physics*, 83(6):3323–3336, 1998.

[79] D. E. Aspnes and J. B. Theeten. Spectroscopic analysis of the interface between si and its thermally grown oxide. *Journal of The Electrochemical Society*, 127(6):1359–1365, 1980.

[80] D. F. Edwards and E. Ochoa. Infrared refractive index of silicon. *Appl. Opt.*, 19(24):4130–4131, 1980.

[81] M. A. Green and M. J. Keevers. Optical properties of intrinsic silicon at 300 k. *Progress in Photovoltaics: Research and Applications*, 3(3):189–192, 1995.

[82] Ernest V. Loewenstein, Donald R. Smith, and Robert L. Morgan. Optical constants of far infrared materials. 2: Crystalline solids. *Appl. Opt.*, 12(2):398–406, 1973.

[83] W. Primak. Refractive index of silicon. *Appl. Opt.*, 10(4):759–763, 1971.

[84] C. D. Salzberg and J. J. Villa. Infrared refractive indexes of silicon germanium and modified selenium glass. *J. Opt. Soc. Am.*, 47(3):244–246, 1957.

[85] C. M. Herzinger, P. G. Snyder, B. Johs, and J. A. Woollam. Inp optical constants between 0.75 and 5.0 ev determined by variable-angle spectroscopic ellipsometry. *Journal of Applied Physics*, 77(4):1715–1724, 1995.

[86] A. Mendez and T. F. Morse. *Specialty Optical Fibres Handbook*. Academic Press, December 2006.

[87] A. C. Turner, C. Manolatou, B. S. Schmidt, M. Lipson, M. A. Foster, J. E. Sharping, and A. L. Gaeta. Tailored anomalous group-velocity dispersion in silicon channel waveguides. *Opt. Express*, 14(10):4357–4362, 2006.

[88] J. I. Dadap, N. C. Panoiu, X. Chen, I.-W. Hsieh, X. Liu, C.-Y. Chou, E. Dulkeith, S. J. McNab, F. Xia, W. M. J. Green, L. Sekaric, Y. A. Vlasov, and Jr. R. M. Osgood. Nonlinear-optical phase modification in dispersion-engineered Si photonic wires. *Optics Express*, 16:1280–1299, 2008.

[89] C. J. Benton and D. V. Skryabin. Coupling induced anomalous group velocity dispersion in nonlinear arrays of silicon photonic wires. *Opt. Express*, 17(7):5879–5884, 2009.

[90] C. Kittel and P. McEuen. *Introduction to solid state physics*. John Wiley & Sons Inc., 1986.

[91] D. Mandelik, H. S. Eisenberg, Y. Silberberg, R. Morandotti, and J. S. Aitchison. Band-gap structure of waveguide arrays and excitation of floquet-bloch solitons. *Phys. Rev. Lett.*, 90(5):053902, Feb 2003.

[92] Vilson R. Almeida, Qianfan Xu, Carlos A. Barrios, and Michal Lipson. Guiding and confining light in void nanostructure. *Opt. Lett.*, 29(11):1209–1211, 2004.

[93] S.A. Maier. Gain-assisted propagation of electromagnetic energy in subwavelength surface plasmon polariton gap waveguides. *Optics Communications*, 258(2):295–299, 2006.

[94] C. Koos, P. Vorreau, T. Vallaitis, P. Dumon, W. Bogaerts, R. Baets, B. Esembeson, I. Biaggio, T. Michinobu, F. Diederich, W. Freude, and J. Leuthold. All-optical high-speed signal processing with silicon-organic hybrid slot waveguides. *Nat Photon*, 3:216–219, April 2009.

[95] A. Samarelli, M. Gnan, , R. M. De La Rue, and M. Sorel. Low propagation loss photonic wire and ring resonator devices in silicon-on insulator using hydrogen silsesquioxane electron-beam resist. In *ECIO*, 2008.

[96] A. Samarelli, D. S. Macintyre, M. J. Strain, R. M. De La Rue, M. Sorel, and S. Thoms. Optical characterization of a hydrogen silsesquioxane lithography process. *Journal of Vacuum Science & Technology B*, 26(6):2290–2294, NOV 2008. Fabrication.

[97] M. Gnan, D. S. Macintyre, M. Sorel, R. M. De La Rue, and S. Thoms. Enhanced stitching for the fabrication of photonic structures by electron beam lithography. *J. Vac. Sci. Technol. B*, 25(6):2034–2037, 2007.

[98] M. Gnan, S. Thorns, D.S. Macintyre, R.M. De La Rue, and M. Sorel. Fabrication of low-loss photonic wires in silicon-on-insulator using hydrogen silsesquioxane electron-beam resist. *Electronics Letters*, 44(2):115 –116, 17 2008.

[99] M. Gnan, G. Bellanca, and R.M. De La Rue. Post-process removal of spurious fabry-perot oscillations caused by cleaved waveguide-ends. *Lightwave Technology, Journal of*, 27(5):500 –510, march1, 2009.

[100] K. Izumi, M. Doken, and H. Ariyoshi. Cmos devices fabricated on buried sio2 layers formed by oxygen implantation into silicon. *Electronics Letters*, 14(18):593–594, 1978.

[101] M. Bruel, B. Aspar, and A. J. AubertonHerve. Smart-cute: A new silicon on insulator material technology based on hydrogen implantation and wafer bonding. *Japanese Journal of Applied Physics 1*, 36(3B):1636–1641, 1997.

[102] S. Franssila. *Introduction to microfabrication*. Wiley, 2004.

[103] Scott Diddams and Jean-Claude Diels. Dispersion measurements with white-light interferometry. *J. Opt. Soc. Am. B*, 13(6):1120–1129, Jun 1996.

[104] Wayne H. Knox, Nathaniel M. Pearson, Kathryn D. Li, and Charles A. Hirlimann. Interferometric measurements of femtosecond group delay in optical components. *Opt. Lett.*, 13(7):574–576, Jul 1988.

[105] Z. Bor, K. Osvay, B. Rácz, and G. Szabó. Group refractive index measurement by michelson interferometer. *Optics Communications*, 78(2):109 – 112, 1990.

[106] Kazunori Naganuma, Kazuo Mogi, and Hajime Yamada. Group-delay measurement using the fourier transform of an interferometric cross correlation generated by white light. *Opt. Lett.*, 15(7):393–395, Apr 1990.

[107] K. Naganuma and H. Yasaka. Group delay and alpha;-parameter measurement of 1.3 mu;m semiconductor traveling-wave optical amplifier using the interferometric method. *Quantum Electronics, IEEE Journal of*, 27(6):1280–1287, 1991.

[108] J. C. Diels, J. J. Fontaine, I. C. McMichael, and F. Simoni. Control and measurement of ultrashort pulse shapes (in amplitude and phase) with femtosecond accuracy. *Appl. Opt.*, 24(9):1270–1282, 1985.

[109] J. M. Stone and J. C. Knight. Visibly "white" light generation in uniform photonic crystal fiber using a microchip laser. *Opt. Express*, 16(4):2670–2675, 2008.

[110] Purnananda Nandi, Zilun Chen, Agata Witkowska, William J. Wadsworth, Timothy A. Birks, and Jonathan C. Knight. Characterization of a photonic crystal fiber mode converter using low coherence interferometry. *Opt. Lett.*, 34(7):1123–1125, 2009.

[111] M. Sheik-Bahae and M. P. Hasselbeck. *Handbook of Optics Volume IV: Optical Properties of Materials, Nonlinear Optics, Quantum and Molecular Optics*, chapter Chapter 17: Third-order Optical Nonlinearities. McGraw Hill, second edition, 2001.

[112] A. Zheltikov, A. L?Huillier, and F. Krausz. *Springer Handbook of Lasers and Optics*, chapter Nonlinear Optics. 1st edition edition, 2007.

[113] Y. Kodama and A. Hasegawa. Nonlinear pulse propagation in a monomode dielectric guide. *IEEE J. Quantum Electronics*, 23(5):510–524, May 1987.

[114] Y. S. Kivshar and G. P. Agrawal. *Optical Solitons : from fibers to photonic crystals*. Academic Press, 2003.

[115] Robert A. Fisher and William K. Bischel. Numerical studies of the interplay between self-phase modulation and dispersion for intense plane-wave laser pulses. *Journal of Applied Physics*, 46(11):4921–4934, 1975.

[116] Robert A. Fisher and W. Bischel. The role of linear dispersion in plane-wave self-phase modulation. *Applied Physics Letters*, 23(12):661–663, 1973.

[117] N. C. Panoiu, X. Chen, and Jr. R. M. Osgood. Modulation instability in silicon photonic nanowires. *Opt. Lett.*, 31(24):3609–3611, Dec 2006.

[118] S. Clemmen, K. P. Huy, R. Baets, D. Taillaert, W. Bogaerts, P. Emplit, and S. Massar. Modulation instability in silicon nanophotonic waveguides. XXXX.

[119] M. Yu, C. J. McKinstrie, and G. P. Agrawal. Modulation instabilities in dispersion-flattened fibers. *Phys. Rev. E*, 52(1):1072–1080, 1995.

[120] F. Biancalana, D. V. Skryabin, and P. St. J. Russell. Four-wave mixing instabilities in photonic-crystal and tapered fibers. *Phys. Rev. E*, 68(4), 2003.

[121] H. Fukuda nad K. Yamada, T. Shoji, M. Takahashi, T. Tsuchizawa, T. Watanabe, J. Takahashi, and S. Itabashi. Four-wave mixing in silicon wire waveguides. *Optics Express*, 13(12):4629–4637, 2005.

[122] T. Shoji, T. Tsuchizawa, T. Watanabe, J. Takahashi, and S. Itabashi. Low loss mode size converter from 0.3 μm square si wire waveguides to single-mode fibers. *Electronics Letters*, 138:1669, 2002.

[123] M. A. Foster, A. C. Turner, J. E. Sharping, B. S. Schmidt, M. Lipson, and A. L. Gaeta. Broad-band optical parametric gain on a silicon photonic chip. *Nature*, 441:960–963, 2006.

[124] M. A. Foster, A. C. Turner, R. Salem, M. Lipson, and A. L. Gaeta. Broad-band continuous-wave parametric wavelength conversion in silicon nanowires. *Optics Express*, 15(20):12949–12958, 2007.

[125] A. C. Turner-Foster, M. A. Foster, R. Salem, A. L. Gaeta, and M. Lipson. Frequency conversion over two-thirds of an octave in silicon nanowaveguides. *Optics Epxress*, 18(3):1904–1908, 2010.

[126] C. R. Giles and E. Desurvire. Propagation of signal and noise in concatenated erbium-doped fiber optical amplifiers. *J. Lightwave Technol.*, 9(2):147–154, 1991.

[127] Govind P. Agrawal. *Applications of Nonlinear Fiber Optics*. Elseview/Academic Press, London, 1st edition, 2001.

[128] B. S. Kawasaki, K. O. Hill, and R. G. Lamont. Biconical-taper single-mode fiber coupler. *Optics Letters*, 6(7):327–328, 1981.

[129] R. I. Laming, J. E. Townsend, D. N. Payne, F. Meli, G. Grasso, and E. J. Tarbox. High-power erbium-doped-fiber amplifiers operating in the saturated regime. *Photonics Tehcnology Letters*, 3(3):253–255, 1991.

[130] J. C. Diels and W. Rudolph. *Ultrashort Laser Pulse Phenomena: Fundamentals, Techniques and Applications on a Femtosecond Time Scale*. Academic Press, 2006.

[131] W. Ding, O. K. Staines, G. D. Hobbs, A. V. Gorbach, C. de Nobriga, W. J. Wadsworth, J. C. Knight, D. V. Skryabin, M. J. Strain, M. Sorel, and R. M. De La Rue. Modulation instability in a silicon-on-insulator directional coupler: role of the coupling-induced group velocity dispersion. *Optics Letters*, 37(4):668–670, 2012.

[132] S. Trillo, S. Wabnitz, G. I. Stegeman, and E. M. Wright. Parametric amplification and modulational instabilities in dispersive nonlinear directional couplers with relaxing nonlinearity. *J. Opt. Soc. Am. B*, 6(5):889–900, 1989.

[133] W. Ding, C. E. de Nobriga, G. D. Hobbs, W. J. Wadsworth, J. C. Knight, A. V. Gorbach, O. K. Staines, D. V. Skryabin, A. Samarelli, M. Sorel, and R. M. De La Rue. Spectral signatures of spatio-temporal solitons in arrays of silicon-on-insulator photonic wires. OSA, 2010.

[134] W. Ding, C. E. de Nobriga, G. D. Hobbs, W. J. Wadsworth, J. C. Knight, A. V. Gorbach, O. K. Staines, D. V. Skryabin, A. Samarelli, M. Sorel, and R. M. De La Rue. Spectral signatures of spatio-temporal solitons in arrays of silicon-on-insulator photonic wires. IOP, 2010.

[135] A. V. Gorbach, W. Ding, O. K. Staines, C. E. de Nobriga, G. D. Hobbs, W. J. Wadsworth, J. C. Knight, D. V. Skryabin, A. Samarelli, M. Sorel, and R. M. De La Rue. Spatiotemporal nonlinear optics in arrays of subwavelength waveguides. *PHYSICAL REVIEW A*, 82(4), OCT 26 2010.

[136] W. Ding, A. V. Gorbach, O. K. Staines, C. E. de Nobriga, G. D. Hobbs, W. J. Wadsworth, J. C. Knight, D. V. Skryabin, A. Samarelli, M. Sorel, and R. M. De La Rue. Spatio-temporal nonlinear optics in arrays of subwavelength waveguides. In *2011 CONFERENCE ON LASERS AND ELECTRO-OPTICS (CLEO)*, 345 E 47TH ST, NEW YORK, NY 10017 USA, 2011. IEEE. Conference on Lasers and Electro-Optics (CLEO), Baltimore, MD, MAY 01-06, 2011.

[137] V.E. Zakharov and A.B. Shabat. Exact theory of 2-dimensional self-focusing and one-dimensional self-modulations of waves in nonlinear media. *Sov. Phys. JEPT*, 34(18):62–63, 1972.

[138] D. V. Skryabin, F. Luan, J. C. Knight, and P. St. J. Russell. Soliton self-frequency shift cancellation in photonic crystal fibers. *Science*, 301(5640):1705–1708, 2003.

[139] P. K. A. Wai, C. R. Menyuk, H. H. Chen, and Y. C. Lee. Soliton at the zero-group-dispersion wavelength of a single-model fiber. *Opt. Lett.*, 12(8):628–630, Aug 1987.

[140] G.R. Boyer and X.F. Carlotti. Nonlinear propagation in a single-mode optical fiber in case of small group velocity dispersion. *Optics Communications*, 60, 1986.

[141] Nail Akhmediev and Magnus Karlsson. Cherenkov radiation emitted by solitons in optical fibers. *Phys. Rev. A*, 51(3):2602–2607, Mar 1995.

[142] C. J. Benton, A. V. Gorbach, and D. V. Skryabin. Spatiotemporal quasisolitons and resonant radiation in arrays of silicon-on-insulator photonic wires. *Physical Review A (Atomic, Molecular, and Optical Physics)*, 78(3):033818, 2008.

[143] P. K. A. Wai, C. R. Menyuk, Y. C. Lee, and H. H. Chen. Nonlinear pulse propagation in the neighborhood of the zero-dispersion wavelength of monomode optical fibers. *Opt. Lett.*, 11(7):464–466, 1986.

[144] P. K. A. Wai, H. H. Chen, and Y. C. Lee. Radiations by "solitons" at the zero group-dispersion wavelength of single-mode optical fibres. *Phys. Rev. A*, 41(1), January 1990.

[145] F. M. Mitschke and L. F. Mollenauer. Discovery of the soliton self-frequency shift. *Opt. Lett.*, 11(10):659–661, 1986.

[146] PK Tien, R Ulrich, and RJ Martin. Optical second harmonic generation in form of coherent cerenkov radiation from a thin-film waveguide. *Applied Physics Letters*, 17(10):447, 1970.

[147] A.V. Buryak and N.N. Akhmediev. Stationary pulse propagation in n-core nonlinear fiber arrays. *Quantum Electronics, IEEE Journal of*, 31(4):682 –688, apr 1995.

[148] Tim A. Birks. personal communication, 2012.

[149] R. Y. Chiao, E. Garmire, and C. H. Townes. Self-trapping of optical beams. *Phys. Rev. Lett.*, 13:479–482, Oct 1964.

[150] D. N. Christodoulides and R. I. Joseph. Discrete self-focusing in nonlinear arrays of coupled waveguides. *Opt. Lett.*, 13(9):794–796, Sep 1988.

[151] H. S. Eisenberg, Y. Silberberg, R. Morandotti, A. R. Boyd, and J. S. Aitchison. Discrete spatial optical solitons in waveguide arrays. *Phys. Rev. Lett.*, 81:3383–3386, Oct 1998.

[152] Dmitry V. Skryabin and Andrey V. Gorbach. *Colloquium* : Looking at a soliton through the prism of optical supercontinuum. *Rev. Mod. Phys.*, 82(2):1287–1299, Apr 2010.

[153] Peter Bienstman, Solomon Assefa, Steven G. Johnson, John D. Joannopoulos, Gale S. Petrich, and Leslie A. Kolodziejski. Taper structures for coupling into photonic crystal slab waveguides. *J. Opt. Soc. Am. B*, 20(9):1817–1821, Sep 2003.

[154] Waleed Mohammed, Mahesh Pitchumani, Alok Mehta, and Eric G. Johnson. Selective excitation of the lp11 mode in step index fiber using a phase mask. *Optical Engineering*, 45(7), 2006.